Experimental Method of Analyzing Stress Intensity Factors and Singularity Order in Rocket Motor Geometry

by

Chang Che-Way

Dissertation submitted to the Faculty of the
Virginia Polytechnic Institute and State University
in partial fulfillment of the requirements for the degree of
Doctor of Philosophy
in
Engineering Mechanics

APPROVED:

C. W. Smith, Chairman

D. Post

J. Morton

R. H. Plaut

R. Czarnek

Sep. 5 1990

Blacksburg, Virginia

Experimental Method of Analyzing Stress Intensity Factors and Singularity Order in Rocket Motor Geometry

by

Chang Che-Way

C. W. Smith, Chairman

Engineering Mechanics

(ABSTRACT)

A series of frozen stress experiments were conducted on surface flaws of varying aspect ratios in pressurized cylinder with star-shaped cutout in order to study the stress intensity factor distribution along the flaw border and to estimate the loss of the inverse square root singularity when the crack border intersects the inner star surface at right angles. By applying a refined optical method, the photoelastic data are converted into classical stress intensity factors resulting from the three dimensional stress state existing at the inner surface and compared with a numerical analysis to indicate the nearly uniform distribution of the stress intensity factor along the crack border. Based upon this result a two dimensional weight function approach is demonstrated to yield accurate values of the maximum stress intensity factor for the motor grain test geometry.

Acknowledgements

The author wishes hereby to express his sincere gratitude and deep appreciation to Professor C. W. Smith of the Engineering Science and Mechanics of Virginia Polytechnic Institute and State University for his help, guidance and financial support during the course of this research. Gratitude is also extended to the other members of my advisory committee, Dr. D. Post, Dr. J. Morton, Dr. R. H. Plaut, and Dr. R. Czarnek, for their impartation of knowledge both in and out of the classroom. The author would also like to thank his lab. partners, Mohammed Rezvani, Lei Wang, and C.C. Chang for their help in the laboratory.

This research was sponsored by The Air Force Astronautics Laboratory. The guidance of Dr. C. T. Liu is appreciated.

Finally, the author wishes to thank his family and parents, and express a special indebtedness to his wife and his son, Li-Yu and Kevin, for their encouragement and support during my graduate work.

This dissertation is dedicated to my parents and my wife.

Table of Contents

List of Illustrations

List of Tables

1.0 Introduction

Solid propellant motors are composite structures of two very dissimilar materials. The geometry of one part of the structure, the case or shell, is relatively simple and can be considered basically as a thin-walled pressure vessel. On the other hand, the geometry of the grain [1] is extremely complicated. The typical geometries of solid propellant rockets are illustrated in Fig.(1.1). The grain is the shaped mass of propellant inside the rocket motor. The propellant material and geometrical configuration of the grain determine the motor performance characteristics.

Surface flaws are the most common defects found in the elastic bodies. Both analytically and experimentally, there are many papers which have reported studies of surface flaws [2-4]. In the last two decades, there also have been several papers which investigated pressurized cylinders with star-shaped cutouts with or without a crack in it. In 1965, Durelli [5] was the pioneer who studied the stress analysis of rocket motors and used frozen stress photoelasticity to study the resulting stress fields. In 1972, Francis and associates [6] also measured the critical stress intensity factor for a crack emanating from the tip of a star finger in a two-dimensional epoxy model of a rocket motor under internal pressure. But all of the above cases considered only the two-

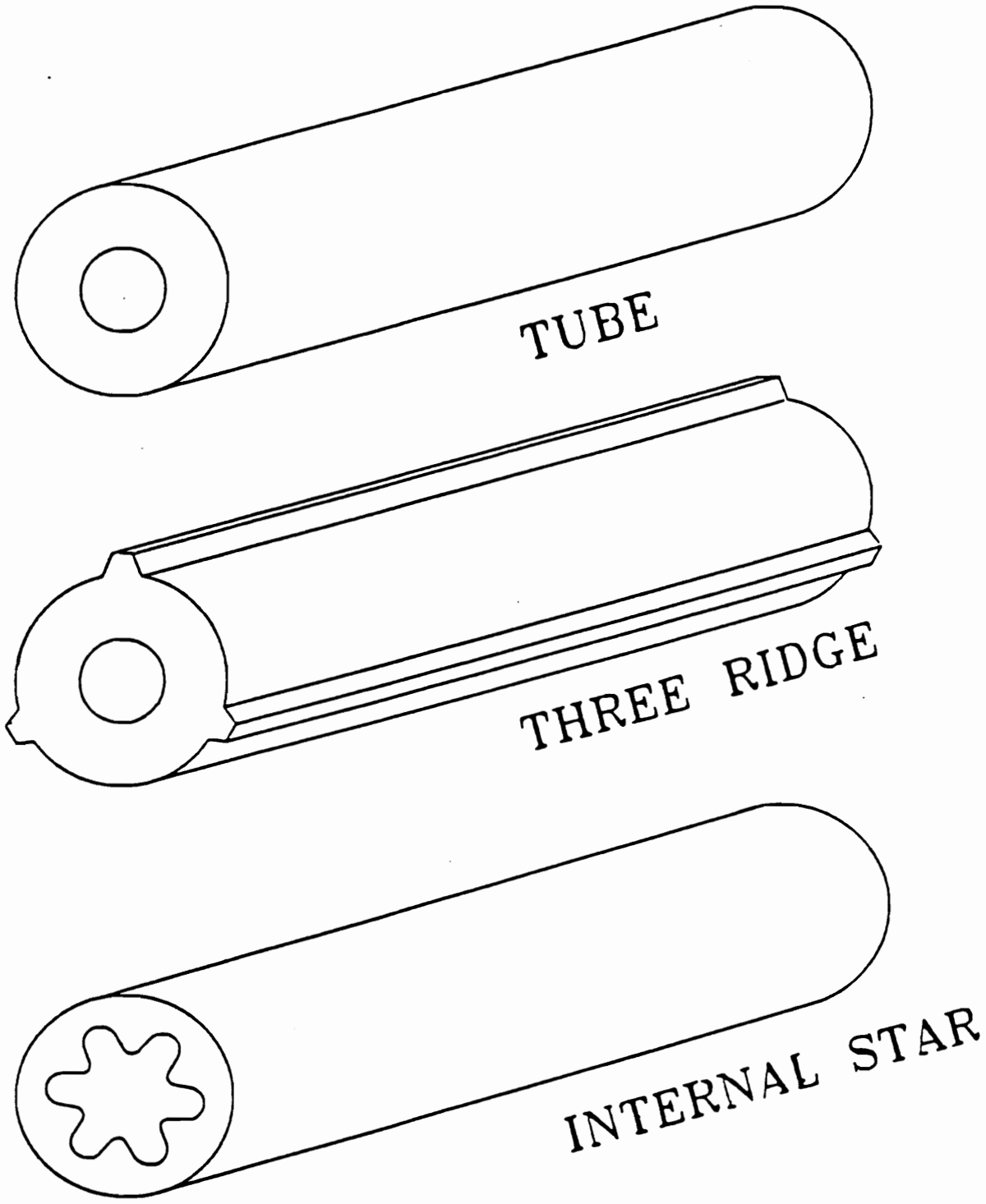

Figure 1.1. The typical geometries of rocket motors [1].

dimensional analytical solution. The author has not located any published papers which related to measurement of stress intensity factor distributions along the crack border of surface flaws in motor grain geometries. In the present state of development of experimental stress analysis techniques, photoelasticity is one of the best methods to determine the stress intensity factor of the rocket motor grain models with the inner semi-elliptical crack.

The cracks might arise in one of the following ways: (1) during the process of manufacture (2) thermal effect of the shrinkage (3) in storage (4) local differences of pressure inside the grain (5) thermal gradient or (6) process of curing and core pulling. When the rocket motor grains burn, the gas pressure in the crack reaches such a high level that the system may begin to burn in an unstable condition.

The objectives of this study are to find the stress intensity factors along the semi-elliptical crack front and estimate the fracture parameter λ_s where the crack intersects the inner surface.

It has been established both analytically [7] and experimentally [8] that , when cracks intersect a free surface at right angles, the inverse square root singularity is lost and that this effect is most significant in nearly incompressible homogeneous materials. Meanwhile, the complex geometry of the specimen also affects the stress intensity factor distributions along the crack border of surface flaws. Both of these conditions are faced when we study the surface flaws in rocket motors which emanate from the tip of the star fingers.

When the measurements such as those described above are made, it is necessary to develop algorithms [9] for converting optical measurements to fracture parameters for the central part of the crack and to utilize a modification based on experimental data to account for the three dimensional stress state existing at the inner star-surface crack front intersection region. The Linear Elastic Fracture Mechanics (LEFM) algo-

rithms are used in the interior of the body where the lowest eigenvalue $\lambda_o = 1/2$. Near the free surface where λ_o changes, a "variable eigenvalue" algorithm is used.

2.0 Literature Review and Problem Definition

2.1 The Work of Durelli

In 1961, Durelli [10] used several methods for the stress analysis of rocket propellant grain models with different boundary conditions, subjected to different loading conditions. The paper was limited to a discussion of strain and stress either in the actual rocket motor or in photoelastic models simulating the rocket motor. The main objective of these analyses was not to determine the magnitude of the stresses actually present in a propellant, but to help the designer of propellant configurations to decide which one of several alternative solutions is the best from the stress distribution point of view. The star configurations shown in Fig.(2.1) correspond to different transverse cross sections of the grain and may correspond to successive stages of burning of the original design.

Durelli assumed that the grain and case materials were elastic and behaved linearly. Both were assumed to be isotropic and homogeneous. Durelli also assumed that anisotropy and heterogeneity would not influence the strain distribution and that their effect would be of random nature. According to these assumptions, Durelli developed

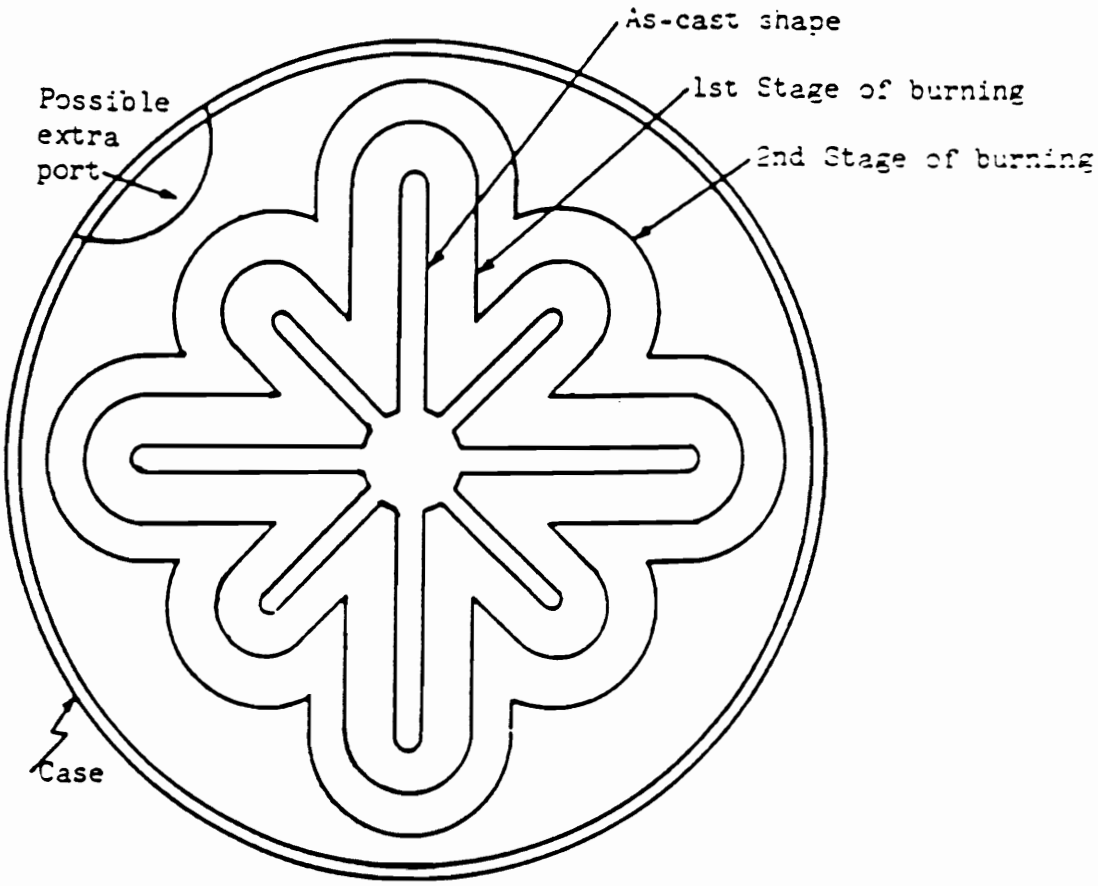

Figure 2.1. Transverse cross section of a solid propellant rocket motor at several stages of burning used by Durelli [10].

some relatively easy techniques for the analysis and redesign of grain models. In most of the tests conducted, the frozen stress method was used. However, no cracks were included in his work.

2.2 The Work of Becker and Brisbane

These authors [11] found the solutions to the problems of star-perforated grains subjected to pressurization and thermal loadings by using stress concentration factors which were obtained photoelastically.

In the stress analysis of solid propellant rocket grain models, the effects of internal star-perforations were investigated by means of an approximate solution which assumed a state of plane strain or a state of generalized plane strain. The two grain shapes used are shown in Fig.(2.2)

The authors used a finite element computer program to obtain numerical solutions for star-perforated grains with the same shapes as photoelastic models. Then, they compared the numerical solution with experimental results. The stresses and strains were obtained from the finite element program and used to calculate values of the stress concentration factor H. Similarly, Becker and Brisbane did not include the crack in the star-perforated grains.

2.3 The Work of Francis and Lindsey

In 1972, Francis and Lindsey [6] were the first investigators to deal with the pressurized crack in two-dimensional rocket motor geometries. They measured the critical stress intensity factor for a crack emanating from the tip of a star finger in a two-

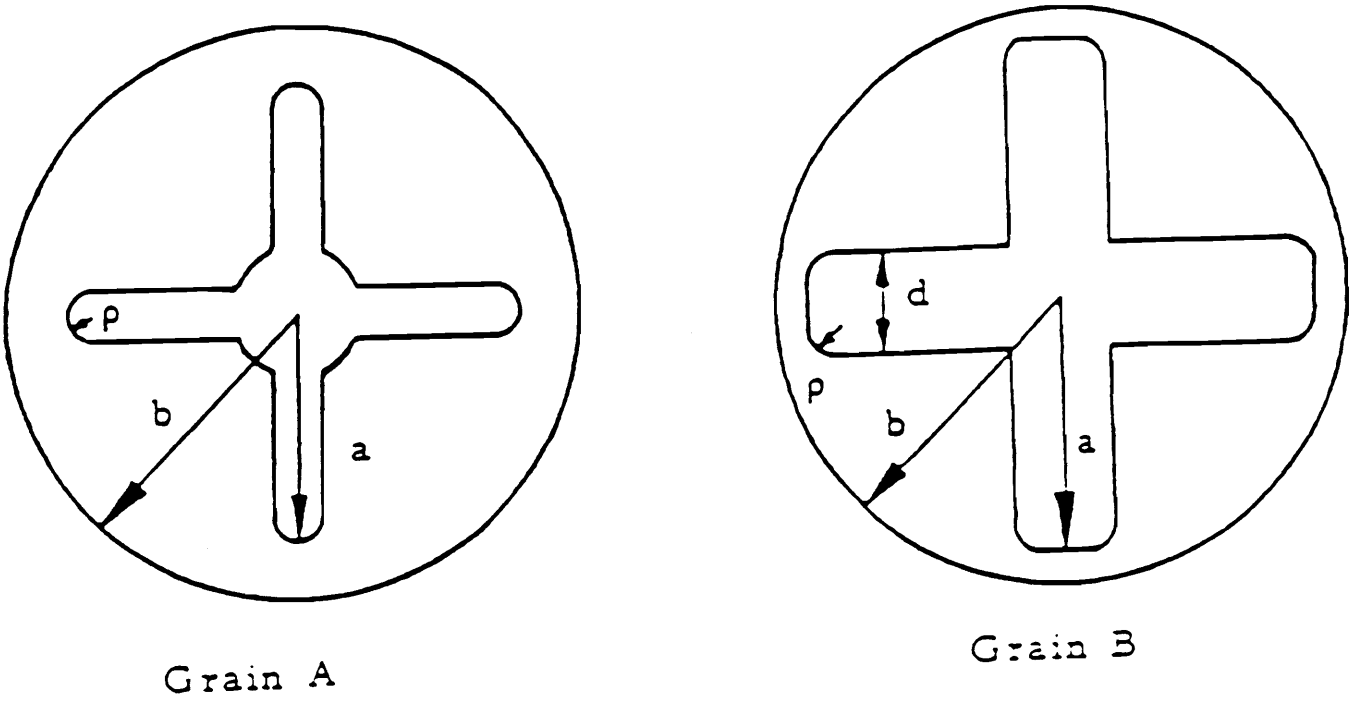

Figure 2.2. The grain shapes used by Becker and Brisbane [11].

dimensional photoelastic model of a rocket motor . They developed a method for evaluating two-dimensional crack behavior in a rocket motor model for pressure loadings where the pressure is applied directly to the crack surfaces.

They used a finite element program which was based on strain energy methods to calculate stress intensity factors for complex cracked rocket motor models. The geometries used were encased circular disks containing three different center perforations common to rocket grains as shown in Fig.(2.3). Then, comparisons between analytical solutions using elastic fracture mechanics and experimental observations of a brittle epoxy for the three different test geometries were made. The numerical results for stress intensity factors are given in the Fig(2.4).

2.4 The Work of Bazant

In 1974, Bazant [12,13] used a numerical method to approach the problem of the stress singularity at the free surface. Bazant used a separation of variables approach in the spherical coordinate system Fig (2.5) to show the displacements for a semi-infinite body as follows:

$$U(\theta, \phi, r) = r^{\lambda} f(\theta, \phi) \tag{2.1}$$

Equation (2.1) was substituted into the spherical form of Navier displacement equations. Then, he used the variational formulation to find the exponent, λ_u, and to calculate a value of stress singularity ($|\lambda_\sigma| = 1 - \lambda_u$) for a stationary crack. The value of λ_σ was .329 for a Poisson's ratio of .5, which differed at the traction free surface from the classical value of 1/2.

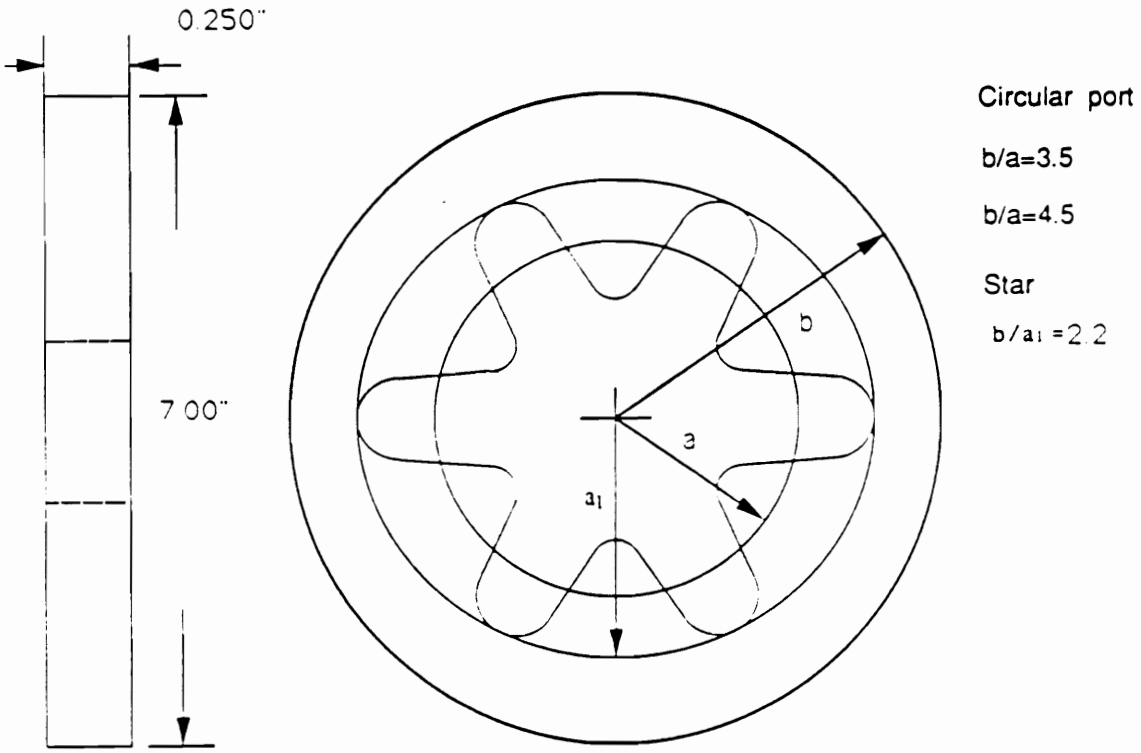

Figure 2.3. The geometries used by Francis et al. [6].

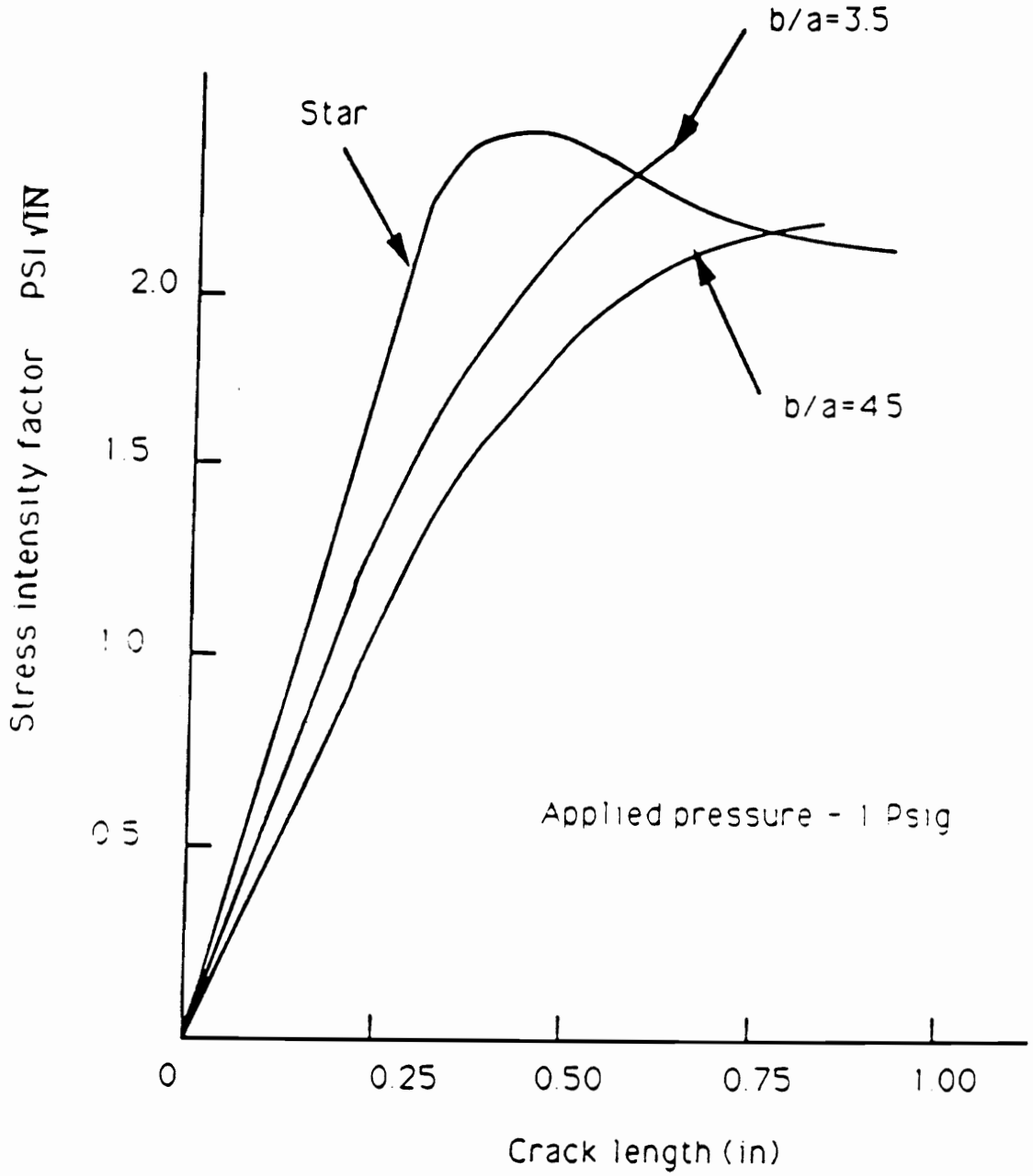

Figure 2.4. Stress intensity factors vs. crack length [6].

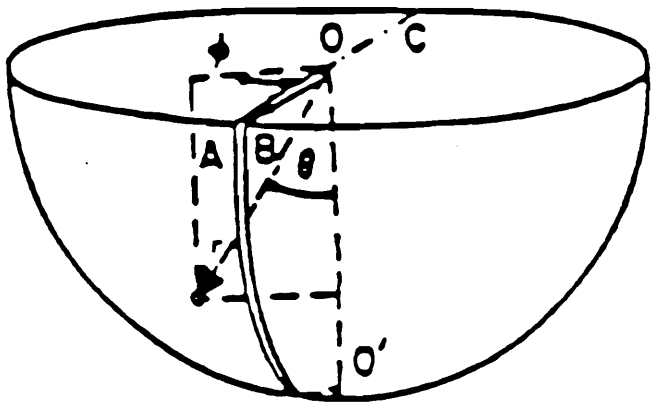

Figure 2.5. The geometry used by Bazant [12].

2.5 The Work of Benthem

J. P. Benthem [14]-[17] investigated the three dimensional state of stress and displacement about a quarter infinite crack in a half-space using eigenfunction expansions for stresses and displacements. Benthem used a spherical coordinate system (r, θ, ϕ) as shown in Fig.(2.6). The half-space extended along $\phi<\pi/2$ and the crack was located along $\theta = 0$, as a quarter infinite crack. His original report was published in 1975.

Benthem expressed stress and displacement fields from variables separable eigenfunction expansions. He first used the Neuber-Papkovitch-Boussinesq stress functions to solve the Navier-Cauchy displacement field equations and chose an axisymmetric geometry. Then, Benthem formulated the stresses in the form:

$$\sigma_{ij} = \sum_{K=1}^{\infty} r^{\lambda_\sigma{}^K} f_{ij}{}^K(\lambda_\sigma, \theta, \phi) \tag{2.2}$$

Benthem's investigation showed that stresses will be dominant in the region near the crack tip, just like a vertex region. He used the seven independent equations of Neuber-Papkovitch-Boussinesq solutions to match the traction free boundary condition at the crack tip. Then, he truncated the expansion and solved for the stress eigenvalues numerically. Benthem found that the stress eigenvalues, λ_σ, were a function of Poisson's ratio ν. Fig.(2.7) shows a plot of λ_σ versus Poisson's ratio. From the figure, Benthem's lowest eigenvalue for a value of Poisson's ratio of 0.5 was $\lambda_\sigma = -0.33$. It also indicated that the value of λ decreased when Poisson's ratio increased.

Benthem's analysis shows that the region near the intersection of a crack front with a traction free surface is in a three dimensional state of stress. In his work, one notes that the inverse square root singularity is lost at the free surface. That means the

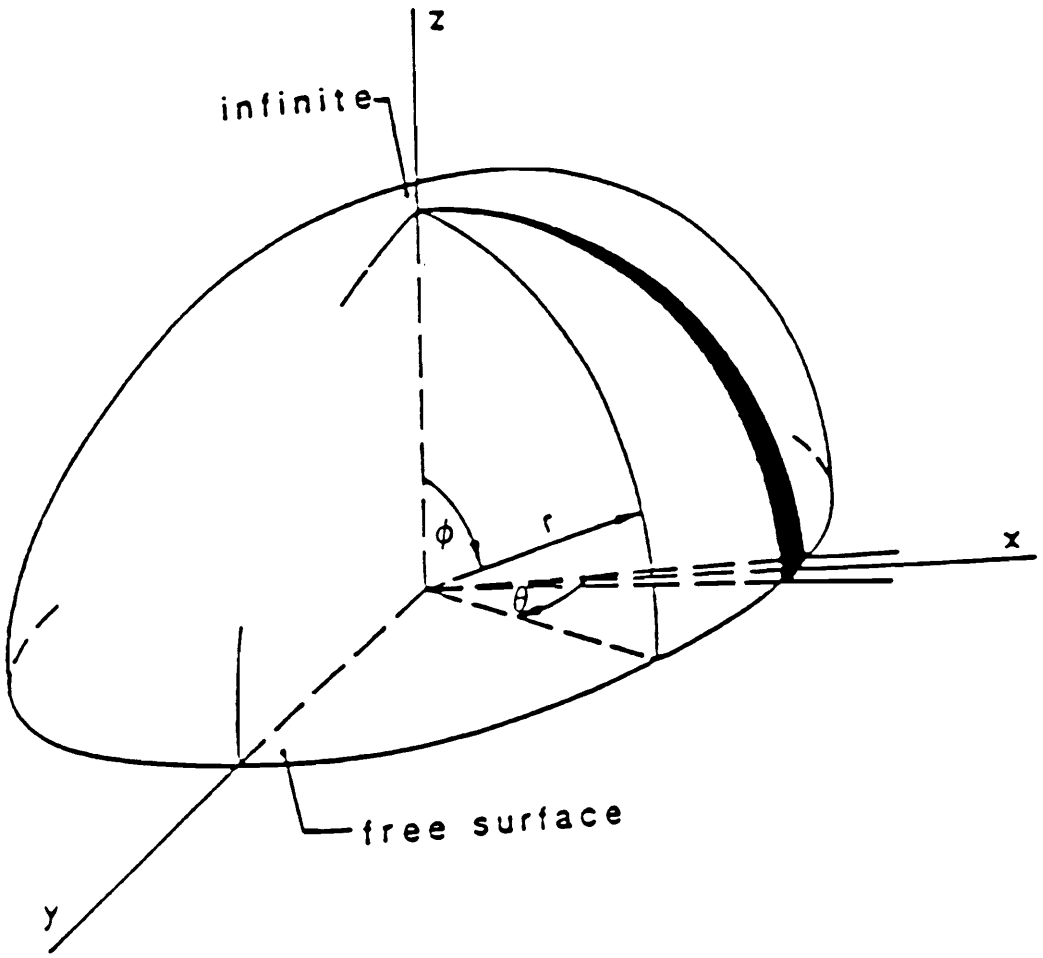

Figure 2.6. The geometry used by Benthem [14].

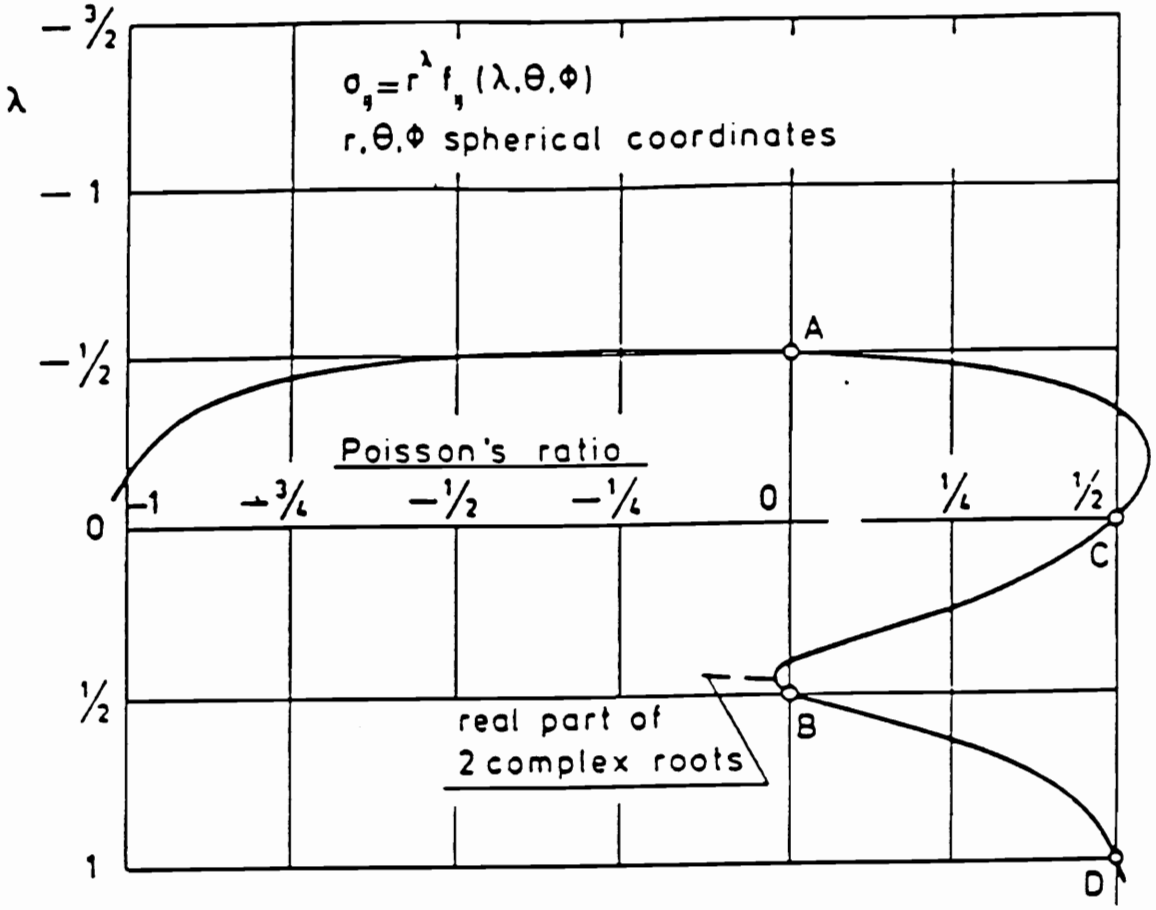

Figure 2.7. Benthem's first stress eigenvalue [14].

two-dimensional concept of stress intensity factor, K_I, is meaningless at the free surface. Meanwhile, Benthem did some experimental work on rubber with a through the thickness Vee notch loaded in mode I. Benthem's results were later confirmed by a finite difference approach, and by Bazant [13] using a finite element method.

2.6 The Work of Kawai and Fujitani

Kawai and Fujitani [18,19] formulated a stress function by using Boussinesq functions and Legendre polynomials. They solved the problem using separation of variables with spherical coordinates.

The collocation method was used on the traction-free surface to measure the stress singularity λ_1. Kawai and Fujitani found that the lowest order eigenvalue was a function of Poisson's ratio, similar to Benthem's result.

2.7 The Work of Swedlow and Associates

In 1978, Swedlow [21] used a numerical method to solve the general problem of singularity at the free surface. He applied the finite element method to find three-dimensional singularities. He followed the approach of Williams [22] to determine the classical singularity for planar elasticity. Swedlow formulated a finite element model with a group of finite element sectors surrounding the singularity.

Subsequently, Swedlow and Burton [23] combined the previously described Finite Element Method(FEM) with the Boundary Integral Equation(BIE) method to measure the singularity order. Fig.(2.8) and Fig.(2.9) show the geometries used by Swedlow and his associates. The boundary conditions on the surface were exactly satisfied by all the

field equations. Although the geometry used in the finite element solution was that of a thick plate, the development of the model was essentially the same as Bazant's.

Table 1 compares results of several investigators. The results of Swedlow and associates are in agreement with these of Benthem, Kawai, and Bazant, especially at low Poisson's ratios.

2.8 The Work of Takakuda

In 1985, Takakuda [24] investigated stress singularities near the crack front edges. First, the crack problems are formulated in the form of the integral equations. William's [22] approach is used for the Griffith crack [25] under plane strain conditions to verify his approach. Takakuda calculated the singularity at a surface crack whose crack front edge intersects the body surface with arbitrary angle. The geometry of the surface crack is shown in Fig.(2.10). He considered a surface crack in a semi-infinite elastic body $x_2>0$,occupying a region on a plane $x_3 = 0$ and subjected to the internal pressure p. The crack front edge intersects the body surface $x_2 = 0$ with angle α. For various values of Poisson's ratio and intersection angle, he obtained the displacement singularities as shown in the Table 2. Comparison of the results with Benthem's solution for $\alpha = \frac{\pi}{2}$ show very good agreement.

2.9 The Work of Cruse

Cruse [26] based his approach on Benthem's [14] result in which the stress singularity order is given by

$$\sigma \sim r^{\lambda} \tag{2.3}$$

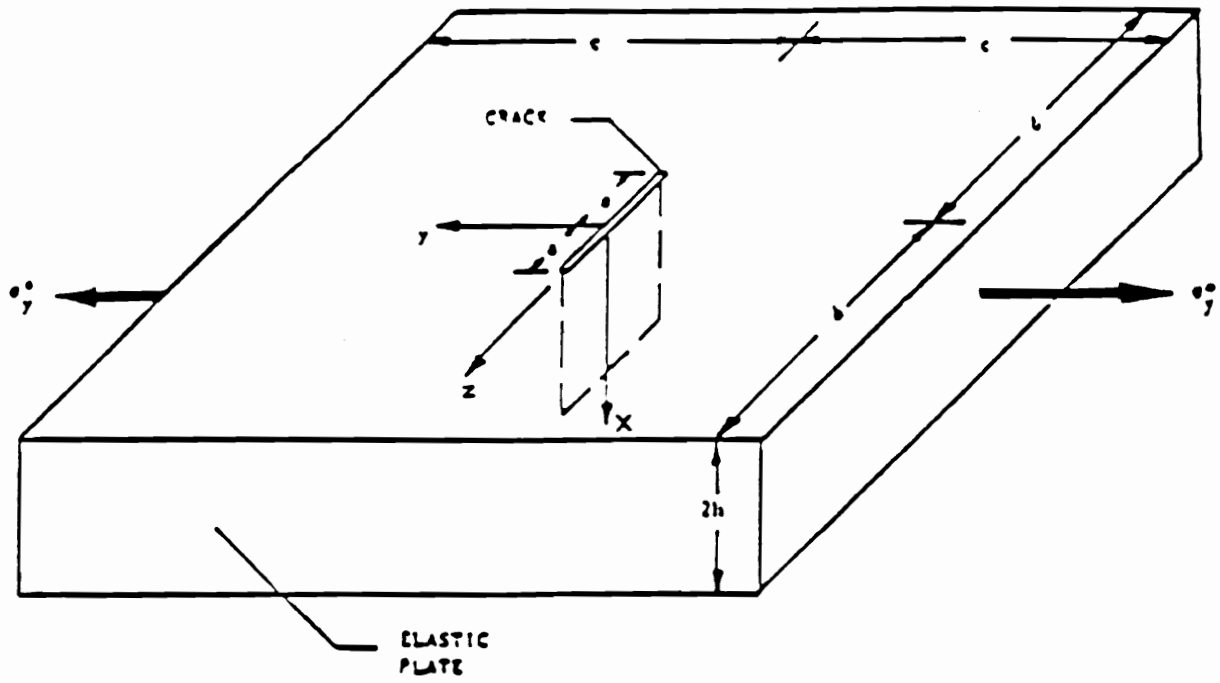

Figure 2.8. The geometry used by Swedlow for finite element formulation [23]

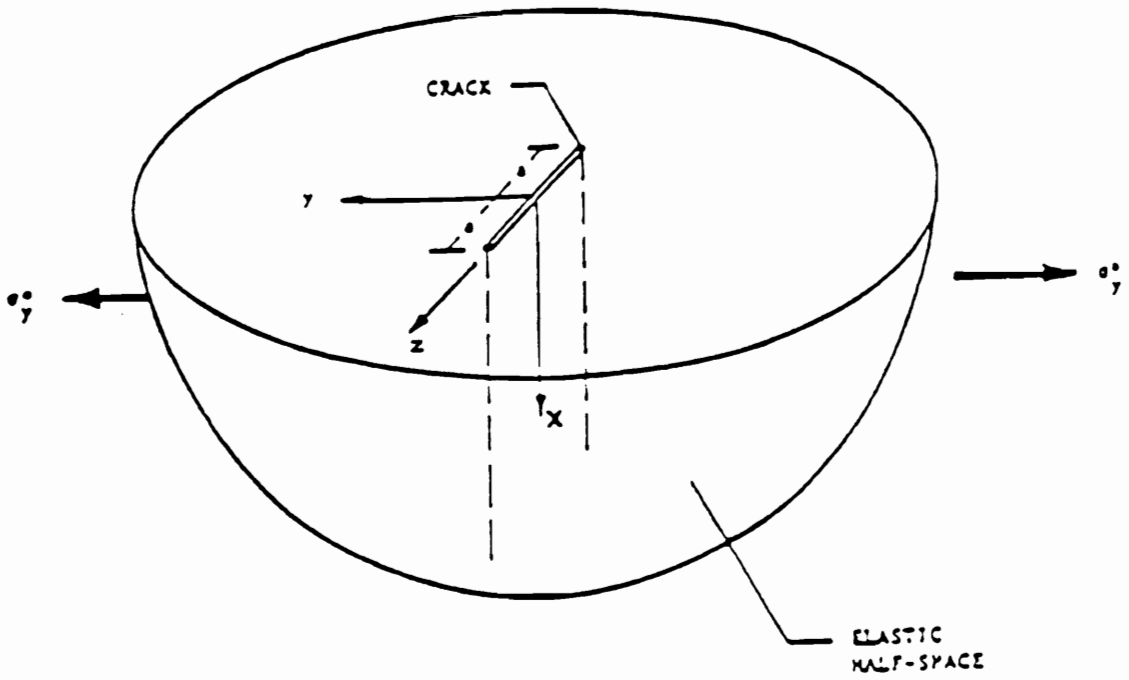

Figure 2.9. The geometry used by Swedlow for boundary integral formulation [23]

Table 1. Summary of several researchers' results [23]

Singularity Exponent at the Crack Vertex

Source	v = 0.0	v = 0.15	v = 0.30	v = 0.40
Analytical by Benthem	0.500	0.484	0.452	0.413
Analytical by Kawai *et al*	0.500	0.480	0.430	0.370
Finite Difference by Benthem	0.500	0.484	0.452	0.414
FEM by Bazant & Estenssoro	0.500	0.484	0.452	0.413
FEM by Swedlow Treatment	0.499	0.485	0.445	0.370

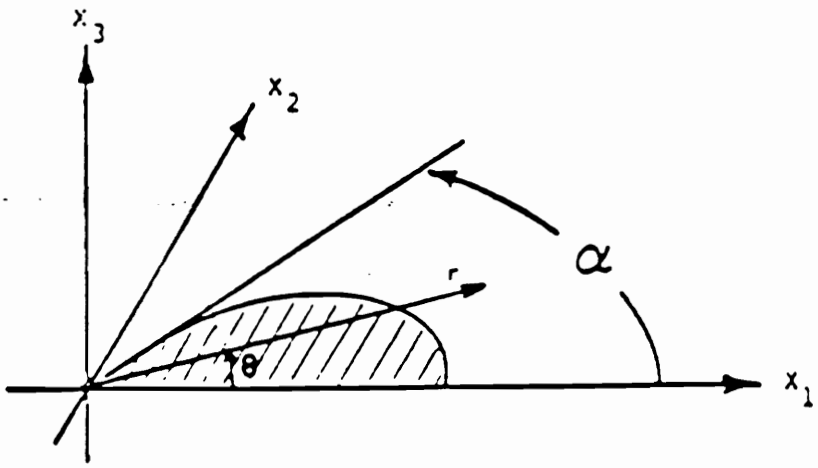

Figure 2.10. The geometry used by Takakuda [24]

Table 2. Takakuda's result [24]

$\frac{a}{\pi}$	v = 0.0	v = 0.1	v = 0.2	v = 0.3	v = 0.4	v = 0.5
0.125	0.8675	0.8861	0.9087	0.9354	0.9661	——
0.250	0.6944	0.7148	0.7464	0.7942	0.8687	——
0.375	0.5805	0.5946	0.6186	0.6578	0.7273	0.9493
0.500	0.4998	0.5096	0.5245	0.5477	0.5867	0.6684
0.625	0.4345	0.4403	0.4464	0.4540	0.4656	0.4864
0.750	0.3925	0.3888	0.3826	0.3740	0.3636	0.3527
0.875	0.3831	0.3706	0.3518	0.3283	0.3031	0.2789

$\lambda = \lambda(v)$, v = Poisson's ratio, and r is the polar distance from the free surface intersection point as used by Benthem. Cruse's analytical results Fig.(2.11) were obtained from the application of the BIE method for three-dimensional elastic behavior. The approach taken is to separate the solution into that part due to the crack and that part due to the free surface. The results show that the plane strain singularity ($\lambda = 1/2$) applies throughout the surface layer near the free surface intersection point.

Meanwhile, he also studied the fatigue crack growth for surface cracks in tension and bending. The material of the tension specimen is AMS 4928 titanium. The shape of the crack front showed turn-back near the free surface which is illustrated in Fig.(2.12a). The surface residual stress was found and that probably was responsible for this effect in a titanium plate[27]. Since this particular crack experienced crack-front turn-back near the free surface, the stress singularity order may be restored to one half. Fig.(2.12b) shows the crack growth profiles in four point bending for a nickel-base superalloy specimen. In four point bending, there is no crack front turn-back which indicates the lack of significant surface residual stresses. The two ends of the crack intersect the free surface at a right angle. The stress singularity at that point is different from one half.

2.10 The Work of Dally, Scimmarella, and Shareef

In 1990, Dally et al. [28] utilized the Westergaard [29] approach in conjunction with the Goursat-Kolosov stress function [30] to develop series solutions for stresses and displacements around the crack tip.

Dally et al. used a holographic interferometric technique to measure the in-plane displacements on the free surface near the crack tip. They modified the stress and

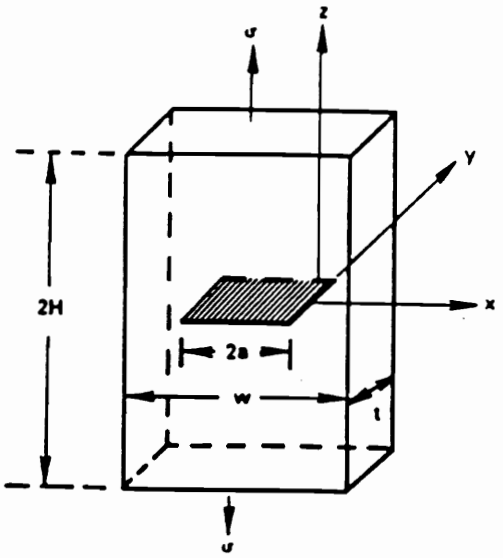

H/a = 1.75; 2a/w = 0.5

t/w = .75; ν = 1/3

(a)

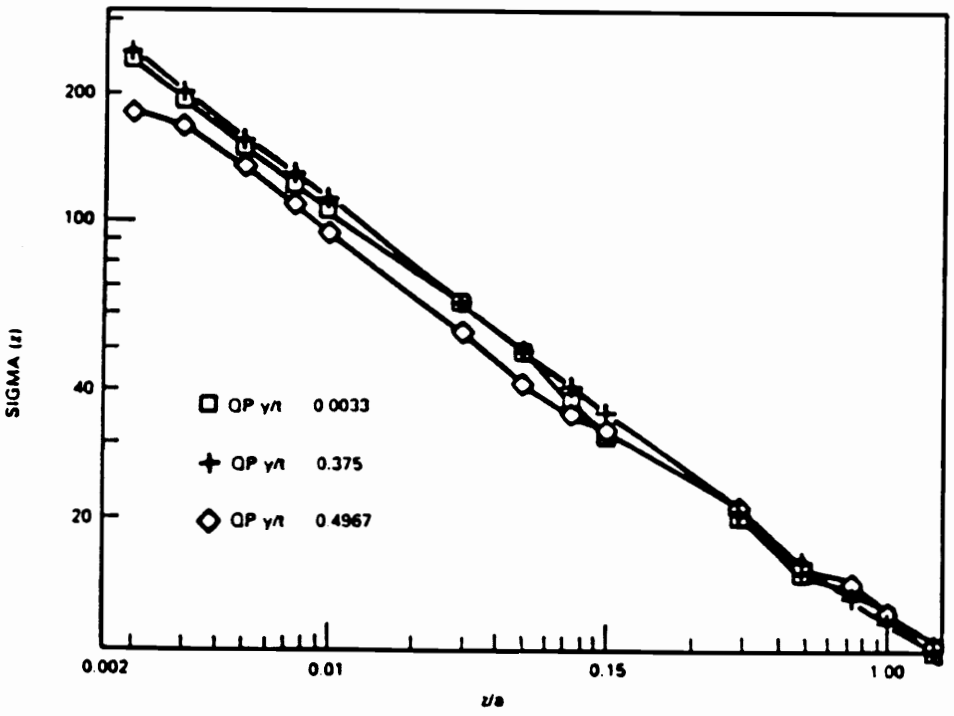

(b)

Figure 2.11. (a) The center-cracked test specimen (b) Stress near the crack tip at various thickness locations [26]

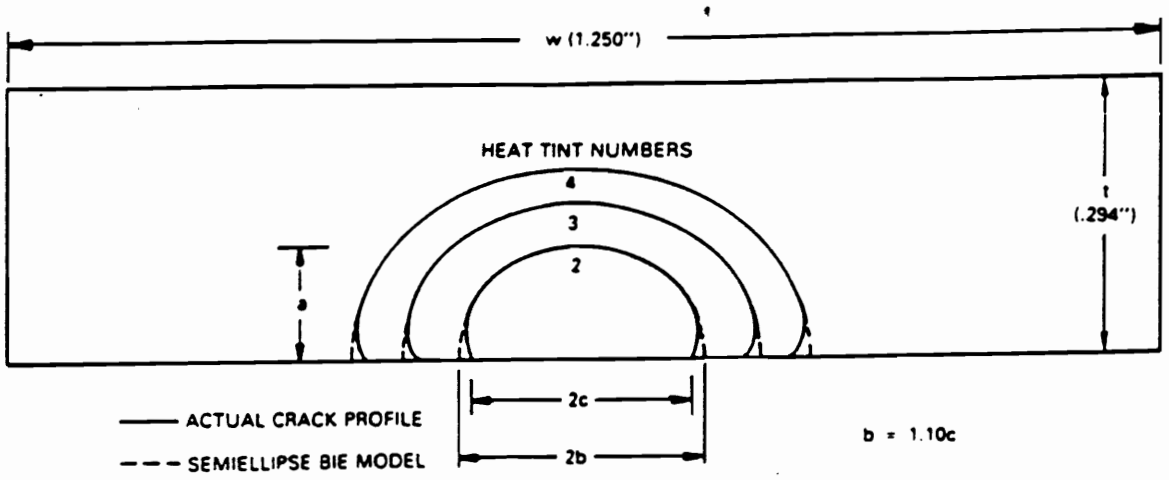

HEAT TINT LOCATIONS

HEAT TINT NUMBER	b/a	a/t	2 c/w
1	1 40	.153	.091
2	1.10	.402	189
3	1.16	.564	.281
4	1.21	.693	.358
5	1.40	.780	460

(a)

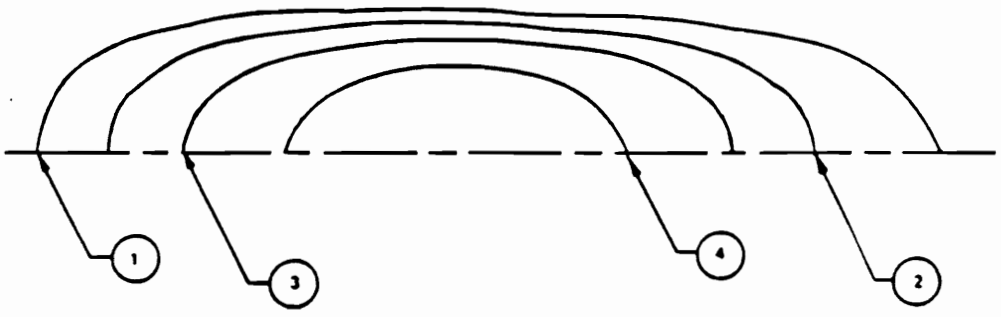

(b)

Figure 2.12. (a) Crack shapes determined for a tension specimen (b) Surface flaw contours for a four point bending specimen [26]

displacement equations by replacing the singularity 1/2 by a variable λ and sought the value of λ which satisfied the experimentally measured displacements.

They used a double-beam illumination technique to obtain the displacement field on the surface of a polyvinyl chloride (PVC) pipe. The pipe properties are Young's modulus E = 2964 MPa, Poisson's ratio $\nu = 0.35$. The coordinate system used by Dally et al. is shown in Fig.(2.13). Series solutions of displacements together with experimental data are used to establish the loss of inverse square-root singularity when cracks intersect a free surface at right angles. It also reconfirms the work of several investigators. Benthem [14-17], Bazant and Estenssoro [13], and Smith and Epstein [36] obtained the values of λ as shown in Table 3. The results given in Table 3 correspond to the eigenvalues of the displacement field λ_u which are related to the eigenvalues of the stress field through the relationship $|\lambda_\sigma| = 1 - \lambda_u$.

2.11 The Work of Raju and Newman

In 1982, Raju and Newman [31] published a paper in which they calculated stress intensity factor influence coefficients for a wide range of semi-elliptical surface cracks on the inside or outside of a cylinder. Stress intensity factors for surface cracks in cylinders were obtained by using a three-dimensional finite element method. An elastic cylinder of wall thickness, t, internal radius, R, and length, 2b, containing a semi-elliptical surface crack of length 2c and depth a on the inner surface of the cylinder is shown in Fig.(2.14). In this analysis, Poisson's ratio was assumed to be 0.3.

The finite element models include singularity elements along the crack front and linear-strain elements elsewhere. That means the singularity elements produced a square-root singularity in stress and strain at the crack front. The crack surfaces were subjected to four stress distributions: uniform, linear, quadratic, and cubic. Those four

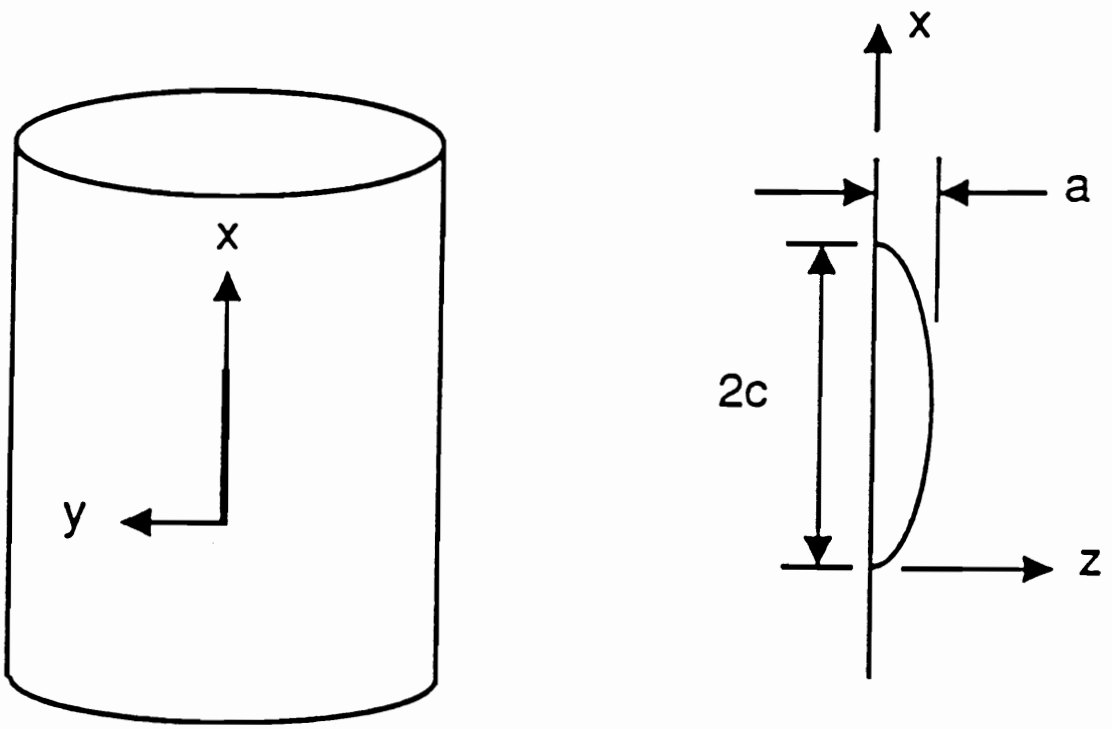

Figure 2.13. Coordinate system of a crack in PVC pipe [28]

Table 3. Values of displacement singularity by various investigators [28]

Poisson's Ratio ν	Benthem (Theory)	Bazant (Theory)	Smith (Experiment)	Dally et al. (Experiment)
0.15	0.5164	0.516	....	....
0.30	0.5481	0.546	....	....
0.35	....	....	....	0.55
0.40	0.5871	0.587	0.58	....
0.48	....	....	0.63	....
0.50	0.6619	....	....	....

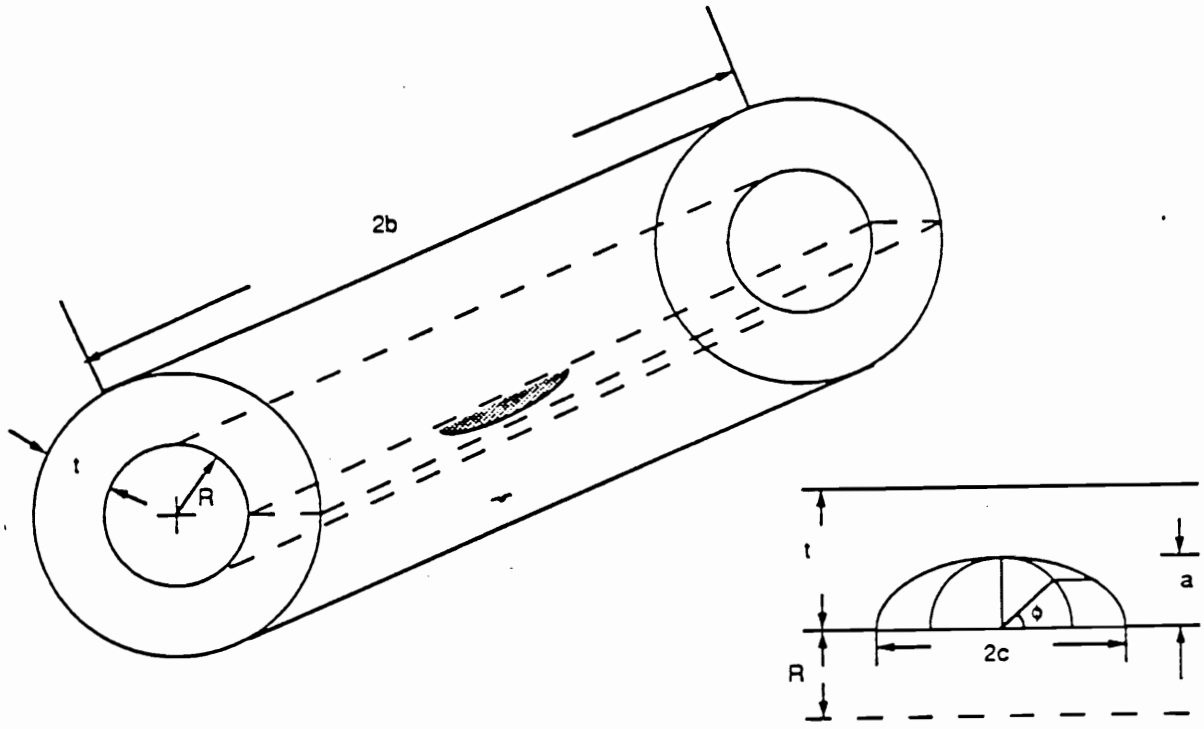

Figure 2.14. Internal surface crack in a cylinder used by Newman and Raju [31]

stress distributions can be superimposed to obtain stress intensity factors for other stress distributions, like internal pressure or thermal shock. Fig.(2.15) shows the result of Raju and Newman.

2.12 The Work of Atluri and Associates

In 1978, Atluri and Kathirsean [32] used a three-dimensional displacement hybrid finite element method to evaluate stress intensity factors for external and internal unpressurized and pressurized semi-elliptical inner surface cracks in pressurized cylinders. For crack front elements, the hybrid displacement model was developed which contained the square root and inverse square root singularity of displacements and stresses and the stress intensity factors were solved along with the unknown nodal displacements.

In 1982, Atluri and Nishioka [33] published another paper in which they used the Finite Element Alternating Method (FEAM) to determine stress intensity factors for semi-elliptical surface flaws in a cylindrical pressure vessel. The geometries of this problem are given in Fig.(2.16). They combined two basic solutions as follows:

(1) Find the analytical solution for an elliptical crack in an infinite solid body with arbitrary loading on the crack surface.

(2) Use the finite element method or boundary element method to calculate a numerical solution for the stresses in an uncracked solid at the location of the crack.

By the method of superposition, the magnification factors for internally pressurized cylinders are rederived by using the polynomial influence functions. Fig.(2.17) shows

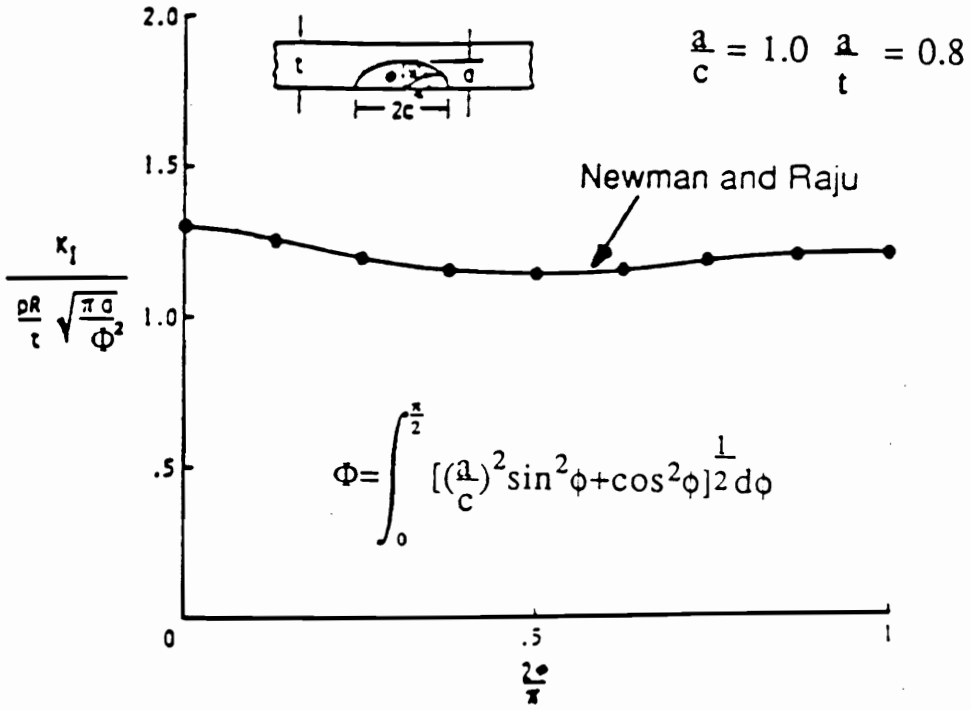

Figure 2.15. Distribution of stress intensity factor for surface cracks in an internally pressurized cylinder by Newman & Raju [31].

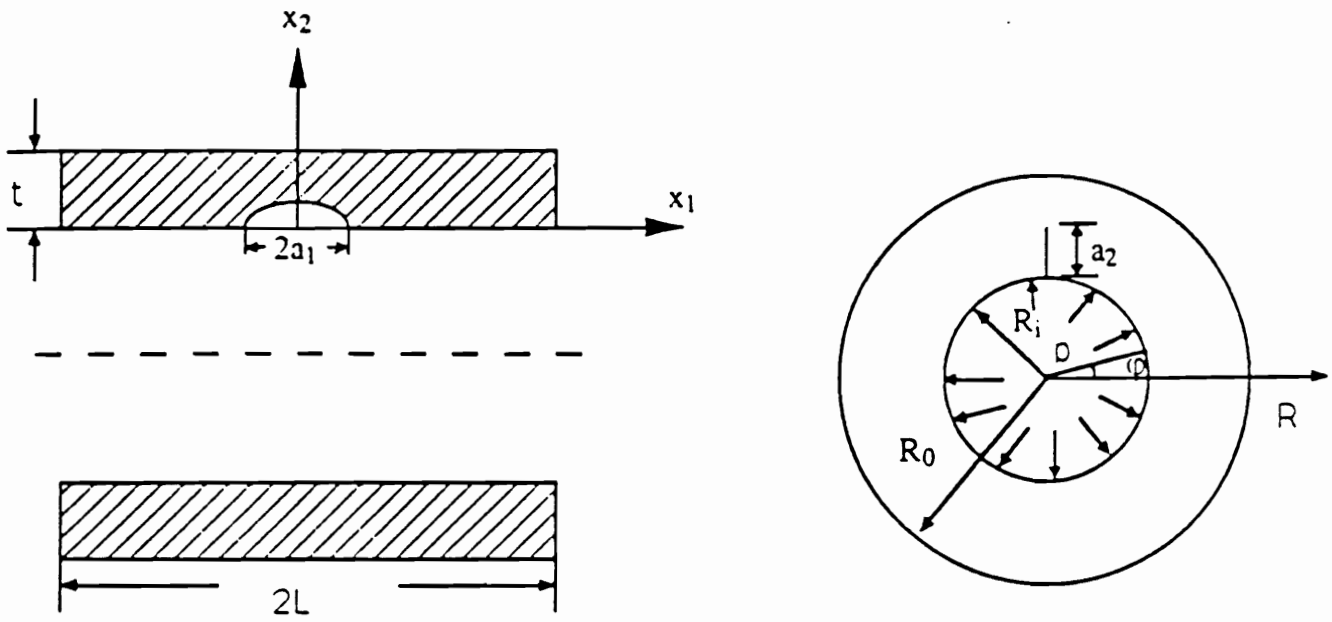

Figure 2.16. The geometry of flawed cylinder used by Atluri and Kathrisean [32]

the results for the magnification factors for an inner semi-elliptical surface crack in a pressurized cylinder.

2.13 The Work of Tan and Fenner

In 1978, Tan and Fenner [34] used the boundary integral equation method to solve the problem of an internally pressurized thick-wall cylinder with a semi-elliptical surface crack. The boundary integral equation (BIE) method basically is the transformation of the partial differential equations applicable throughout the solution domain into a set of integral equations over the boundary. The BIE method reduces the size of the computational problem, and increases solution accuracy.

The geometry of the crack is shown in Fig.(2.18). Fig.(2.19) illustrates the variation of stress intensity factors K_I along the crack front. For internally pressurized cylinders with semi-elliptical surface flaws, they predicted that the value of the stress intensity factor decreases slightly along the crack front from the center of the semi-elliptical crack, reaching a minimum before increasing rapidly at the internal surface of the cylinder.

2.14 The Work of Kobayashi and Associates

In 1976, Kobayashi and his associates [35] used two-dimensional finite element analysis in estimating the stress intensity factors of a pressurized semi-elliptical crack at the internal surface and an unpressurized semi-elliptical crack at the external surface of an internally pressurized cylinder.

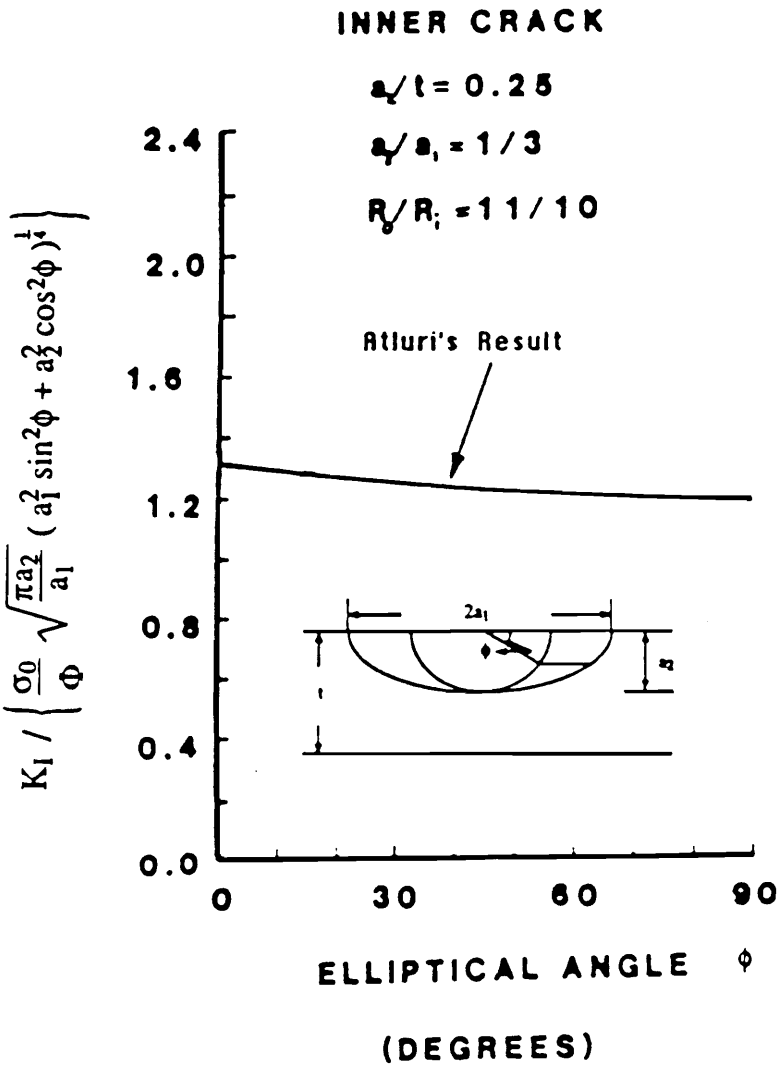

Figure 2.17. Magnification factor for an inner semi-elliptical surface crack in a pressurized cylinder [33].

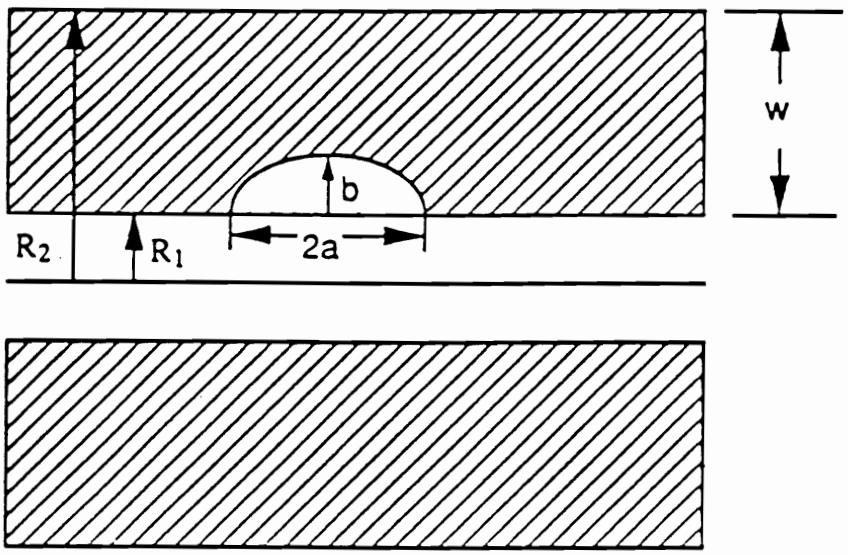

Figure 2.18. The geometry used by Tan and Fenner for semi-elliptical surface crack in a thick walled cylinder [34].

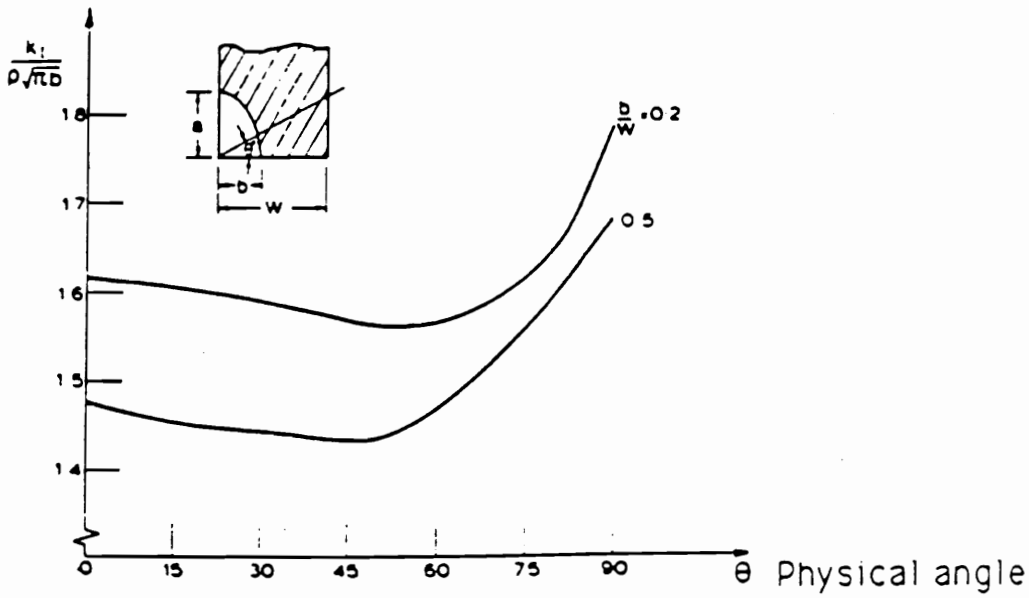

Figure 2.19. Variations of stress intensity factor along the crack front by Tan and Fenner [34].

Kobayashi et al. applied a " correction " of flat plate solutions by " curvature correction factors " estimated from two-dimensional analysis. Curvature effects of the cylinder are determined by comparing two-dimensional finite element solutions of fixed-grip, single edge-notch plates and single edge notched cylinders.

In the solution procedures of Kobayashi, the effect of the back surface on the crack was ignored and this may be critical in the case of oblong cracks when the cracks penetrate deeper into the thickness of the pressure vessel wall. Fig.(2.20) shows the results obtained by Kobayashi and his associates.

2.15 Experimental Work of Smith, et al.

For over a decade, Smith and his associates [36-46] have worked toward the development of an optical experimental method for the measurement of the stress singularity values and prediction of the distribution of the stress intensity factors in three-dimensional cracked body problems. Smith, et al. used the " stress freezing photoelasticity " technique to investigate those problems. Many problems are so complicated that reliable analytical solutions are not available, Smith et al. developed experimental procedures to confirm the analytical or numerical work that had been done or to estimate results when solutions were not available.

Smith and Epstein attempted to measure the variation of the stress singularity order through the thickness for a four point bending specimen with artificial crack at the center. Fig.(2.21) shows the geometry used by Smith. The lowest eigenvalue for stress λ_o versus depth into the specimen half thickness is shown in Fig.(2.22). In order to adapt measured variations in λ_o at the free surface to the framework of LEFM, Smith and Epstein have suggested in prior work the use of a quantity K_{cor}, the "corresponding" stress intensity factor, which replaces the quantity $(K_{I_{oAP}}/r^{\lambda_o})$ by $(K_{corAP}/r^{1/2})$ so that

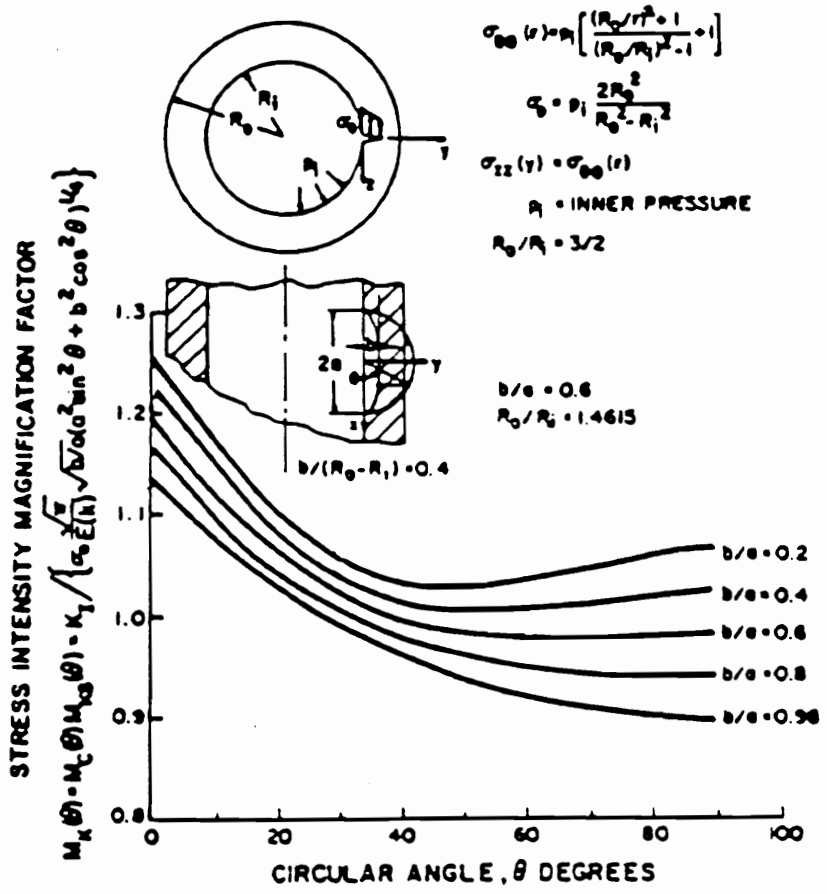

Figure 2.20. Stress intensity magnification factor of a pressurized inner semi-elliptical crack in a pressurized cylinder [35].

the dimensions of the SIF are restored. K_{cor} becomes the SIF which would exist if the free surface effect were not present and the dimensional substitution leads to $K_{cor} = K/2\lambda_e$. Fig.(2.23) indicates the " corresponding " K_I versus the specimen half thickness.

Smith and Lloyd also measured the dominant stress singularity values for semi-elliptical cracks in finite thickness plates and the distributions of the stress intensity factors along the crack border. The specimen geometry is shown in Fig.(2.24). The results of the stress singularity values and the variations of K_I are shown in Fig.(2.25) and Fig.(2.26). Rezvani modified Epstein's experimental work for a natural through edge crack in four point bending specimens which the author was involved in. The results of the stress singularity variation through the thickness are shown in Fig.(2.27). The value of λ_u at the free surface is used in modifying the algorithm for determining λ_e at that point.

2.16 Problem Definition

The problem proposed to be studied here experimentally consists of a longitudinal semi-elliptical crack of depth " a " and length " 2c " located at the center of the inner surface of a pressurized cylinder with a star- shaped cutout. There are two goals in this thesis.

(a) First, by using appropriate algorithms, the value of the dominant eigenvalue λ_e is estimated experimentally when the border of a surface flaw emanating from the finger of a star shaped cutout in a cylinder under internal pressure intersects the inner surface of the star finger. Experimental values are to be compared with the existing literature.

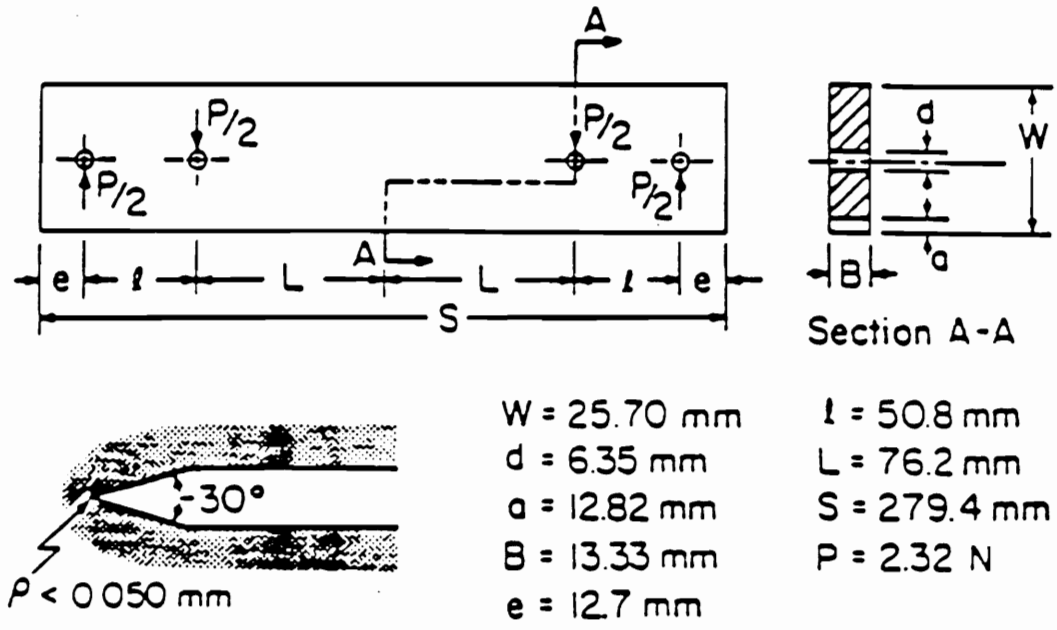

Figure 2.21. The specimen geometry used by Smith and Epstein [36]

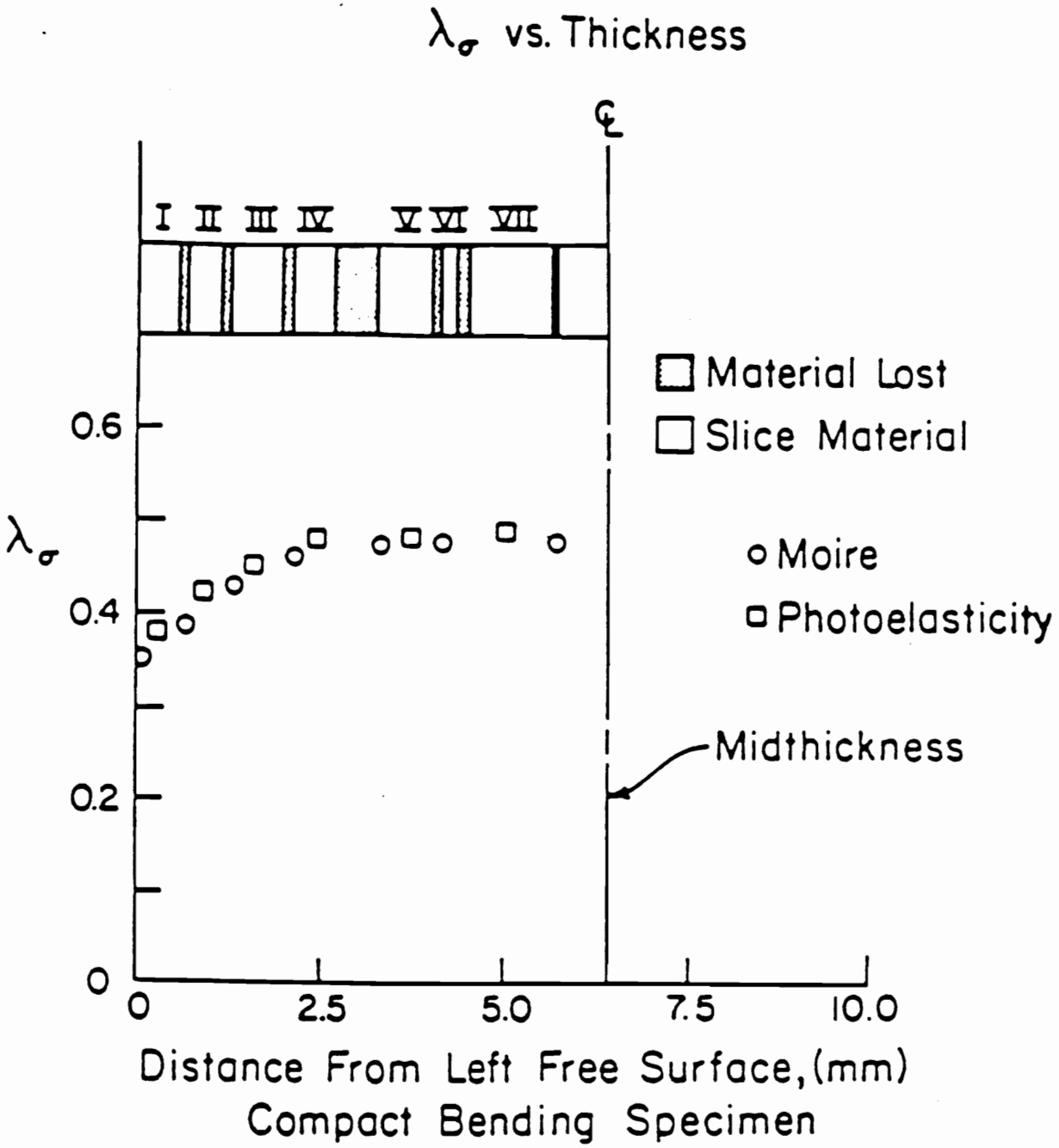

Figure 2.22. Epstein's variations of dominant stress eigenvalue [36]

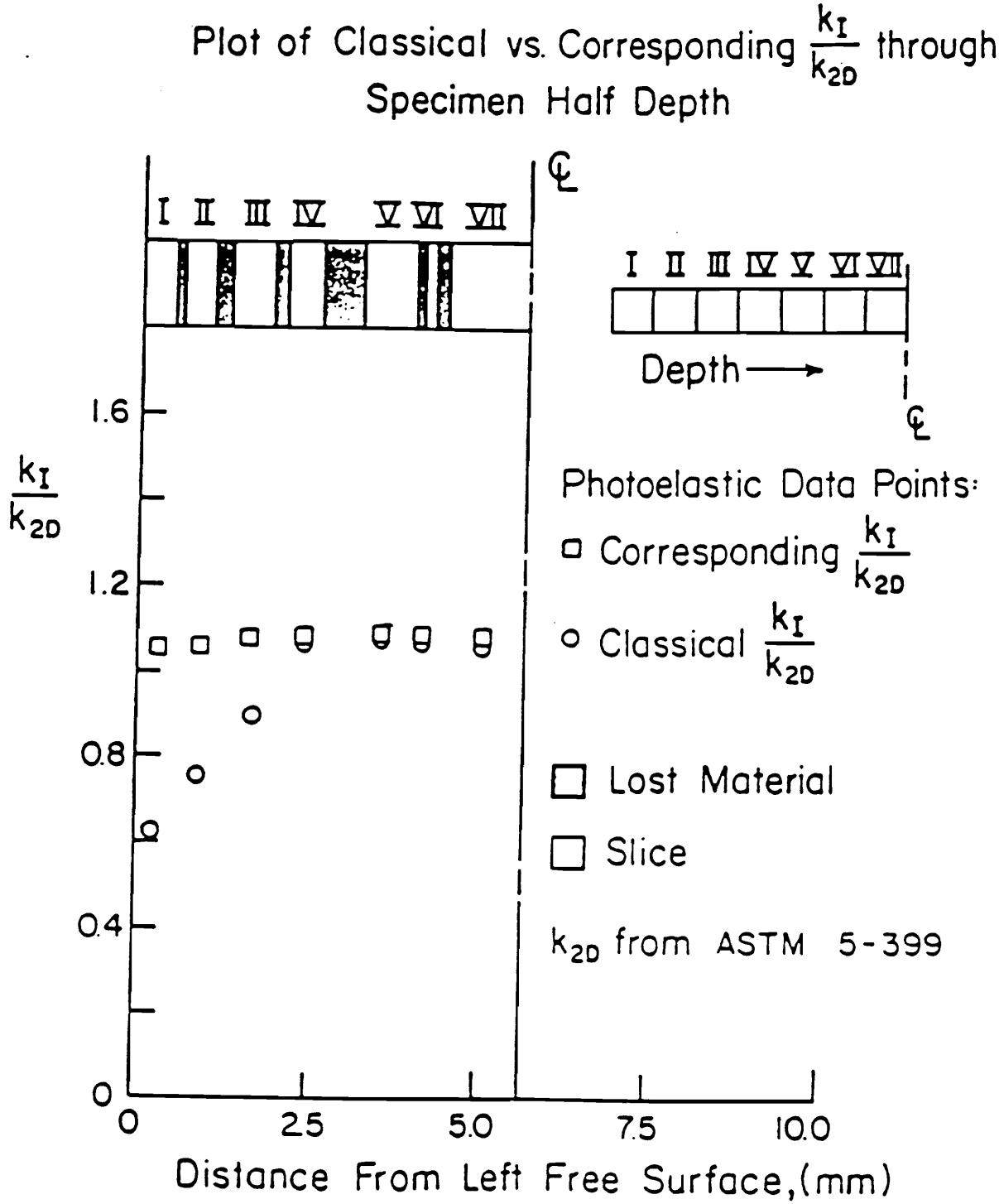

Figure 2.23. Plot of the "corresponding" S.I.F vs. LEFM S.I.F by Epstein [36]

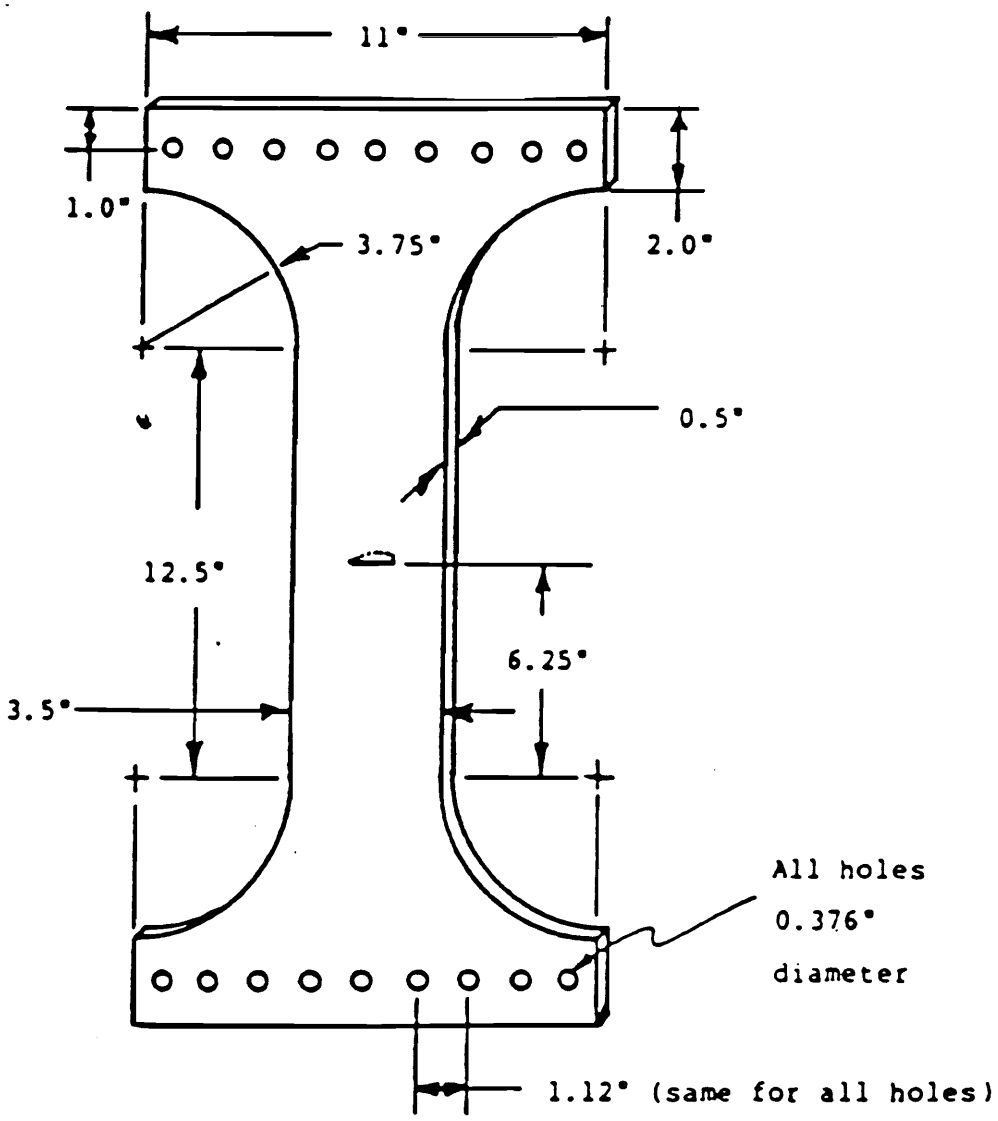

Figure 2.24. The specimen geometry used by Smith and Lloyd [37]

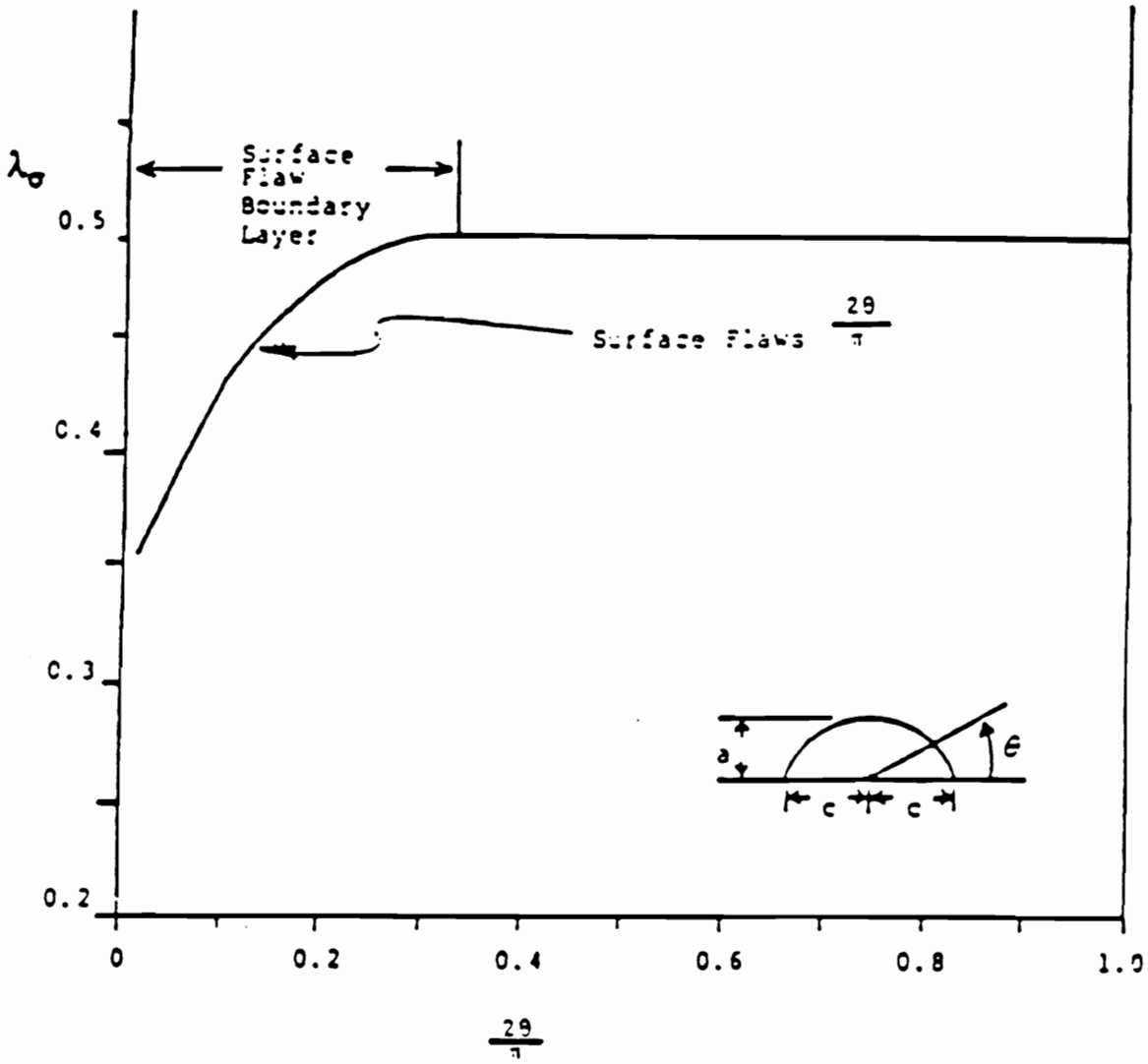

Figure 2.25. The distributions of the stress singularity for surface flaw in wide tension plate [38].

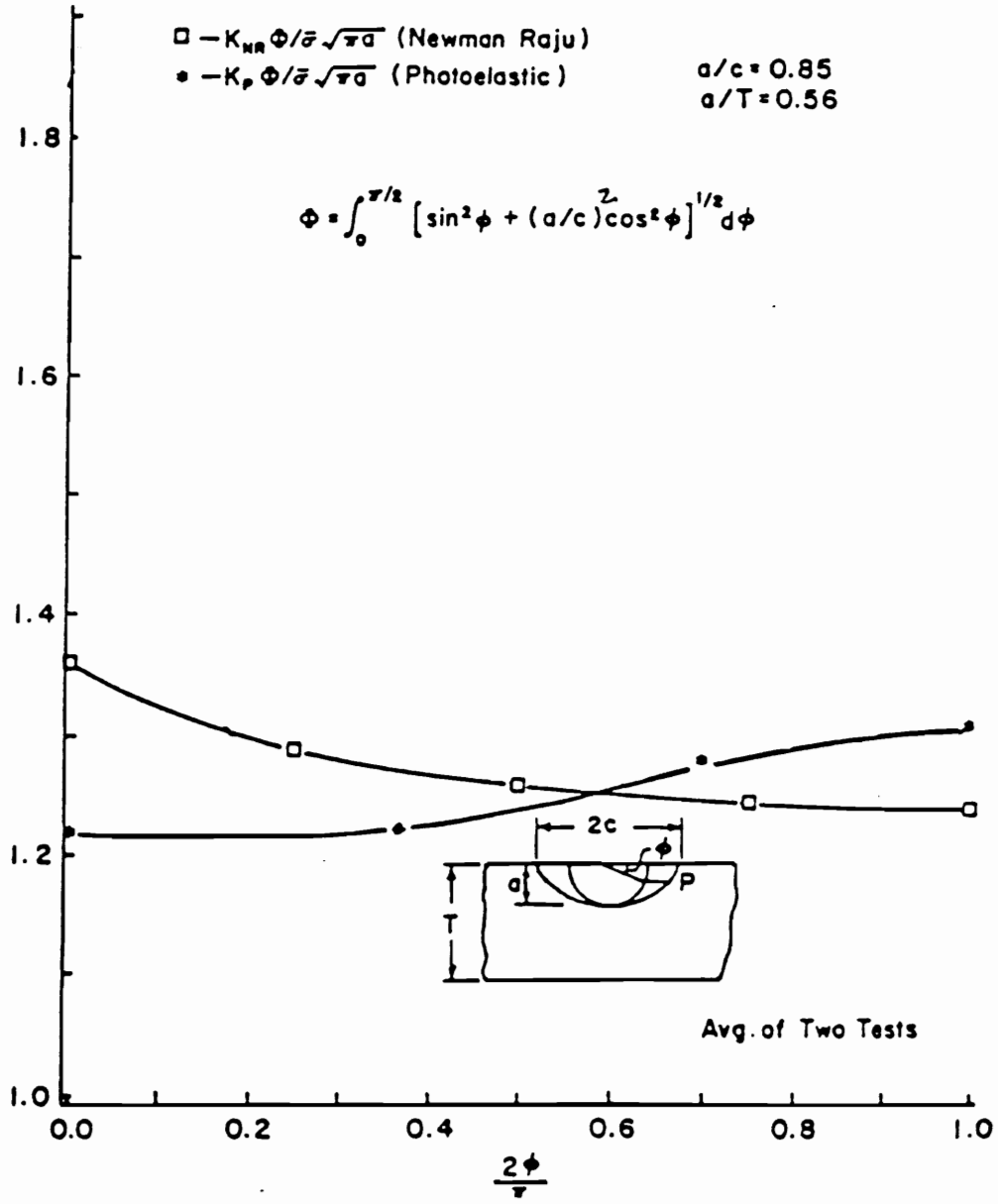

Figure 2.26. The distributions of the stress intensity factors along the crack front for the wide tension plate [39].

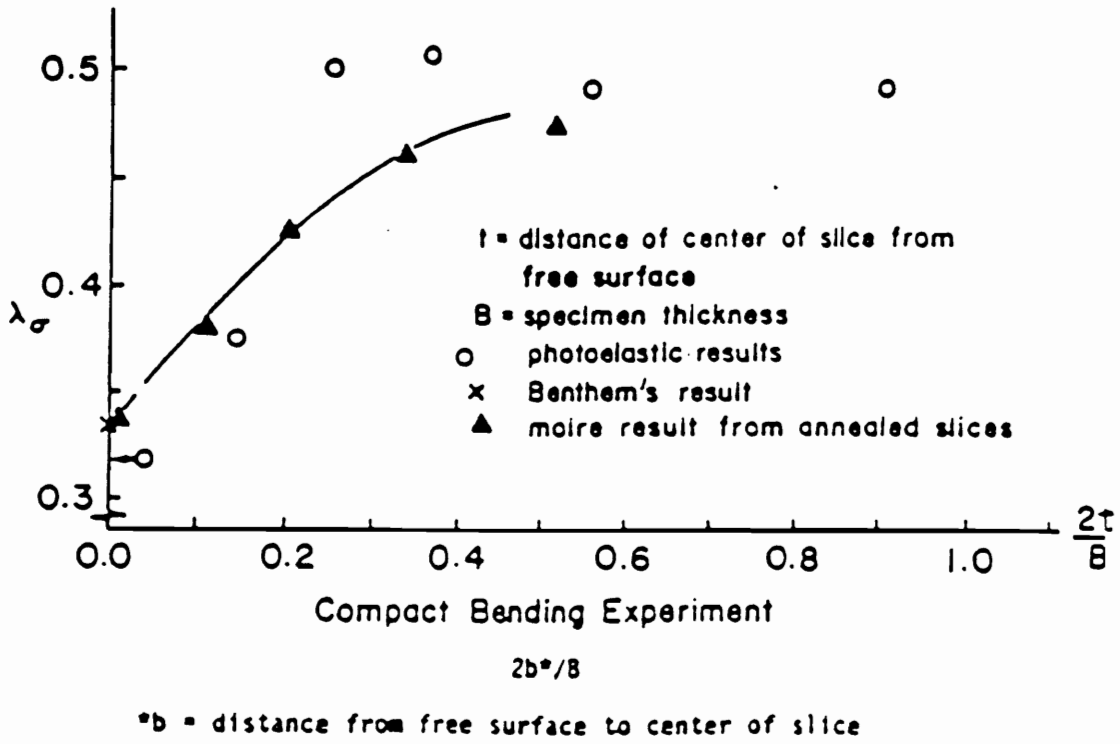

Figure 2.27. Stress singularity variation through thickness for natural crack [40].

(b) Secondly, by using appropriate linear elastic fracture mechanics algorithms for shallow, moderate and deep naturally grown surface flaws as described in [2], the distributions of the stress intensity factor can be determined and by comparing with numerical solutions for surface flaws in cylinders, the degree of uniformity of the S.I.F. distributions can be shown.

(c) Thirdly, taking advantage of this uniformity, a two dimensional weight function approach can be used to predict the maximum S.I.F. for the rocket motor geometry.

3.0 Experimental Method in Linear Elastic Fracture Mechanics

3.1 Introduction

An experimental " stress freezing photoelasticity " technique will be applied for the analysis of crack tip phenomena. This chapter will include the material behavior, specimen geometry, preparation of specimen, calibration test, experimental procedures, and experimental set-up. The Tardy compensation method [47] and the Partial mirror fringe multiplication [48]-[49] will be applied in the experiments. Appendix A will briefly explain those two applications.

3.2 Material Behavior

Test specimens were cylinders with star-shaped cutouts made from stress freezing photoelastic material known as epoxy PLM-9. The photoelastic models were cast around a star shaped core and within an external cylindrical RTV rubber mold at the

Measurements Group Laboratories. Epoxy PLM-9 has diphase characteristics. Mechanical behavior of the material at the room temperature is Kelvin-like Fig.(3.1); its response is viscoelastic. However, when heated to its " critical temperature ", the viscous coefficient μ approaches zero and one is left with purely elastic behavior (E= Young's modulus). That means such materials exhibit a time dependent response to load at room temperature with a $\nu = 0.36$, but when loaded above critical temperature, the time dependency vanishes and the material behaves as a linear elastic, nearly incompressible material ($\nu = 0.5$) [50].

Epoxy PLM-9 has a critical temperature of about $235^{0}F - 245^{0}F$. At room temperature, its Young's modulus is 480 Ksi (3.3 GPa) and it has a stress fringe constant, f, of 60 psi/fringe/in (10.5 KPa/fringe/m). At critical temperature, the value of Young's modulus decreases to 6000 psi (0.04 GPa), and the value of f is reduced to 2.7 psi/fringe/in (473 Pa/fringe/m). Above the critical temperature, the material stiffness is about 2% of its room temperature value and its material stress fringe value is about 5% of its room temperature value.

3.3 Specimen Geometry

The geometry of the specimens used in this project is shown in Fig.(3.2). The cracked cylinder under internal pressure is a three dimensional Mode I test specimen. The specimen is loaded with internal pressure. The model contains a semi-elliptical part through crack and is modelled from the stress freezing epoxy PLM-9. The slices are perpendicular to the crack border and those slices form a two-dimensional plane. Fig.(3.3) shows a typical mode I ischromatic pattern for a frozen stress slice cut perpendicular to the flaw border and crack surface.

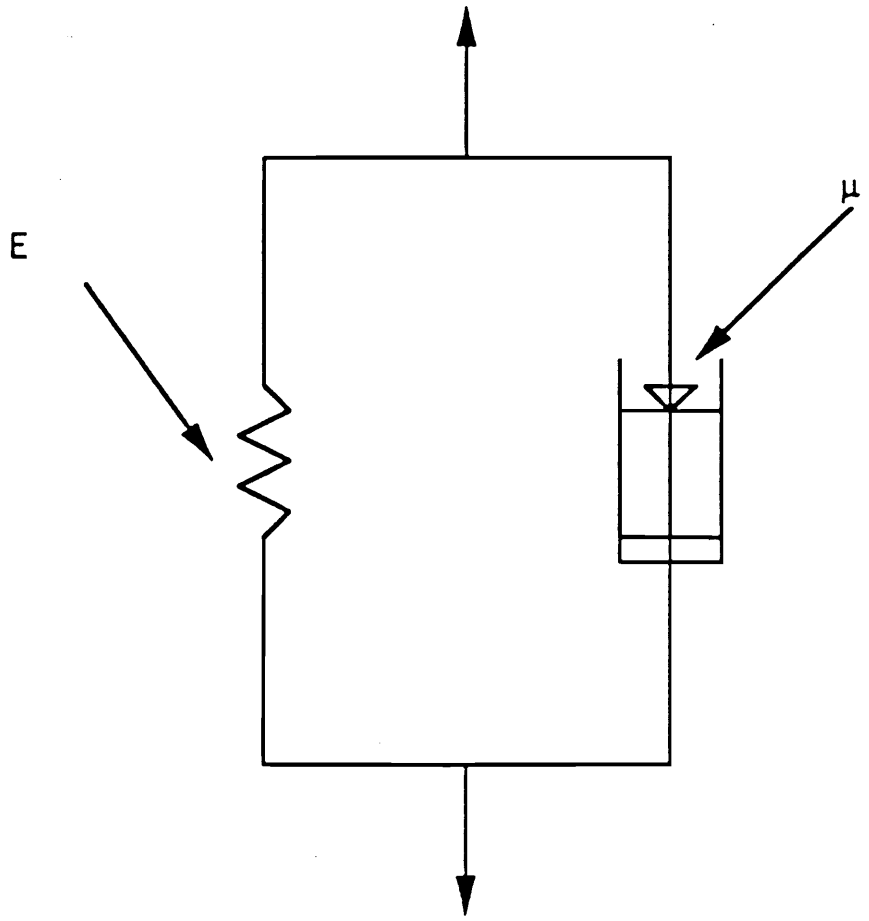

E = Young's Modulus

μ = First Coeff. of Viscosity

Figure 3.1. Kelvin material

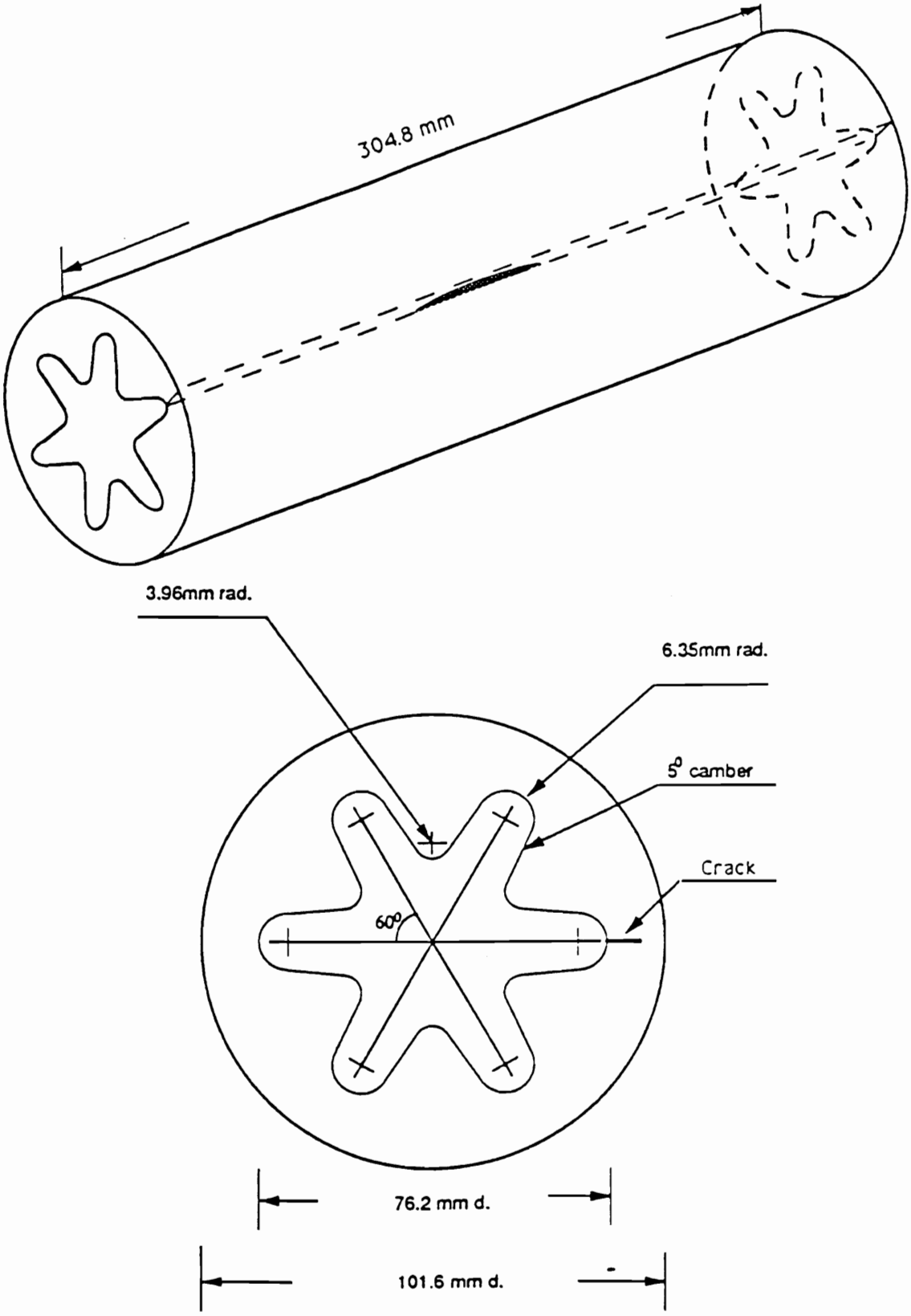

Figure 3.2. The geometry of the cylinder with star-shaped cutout

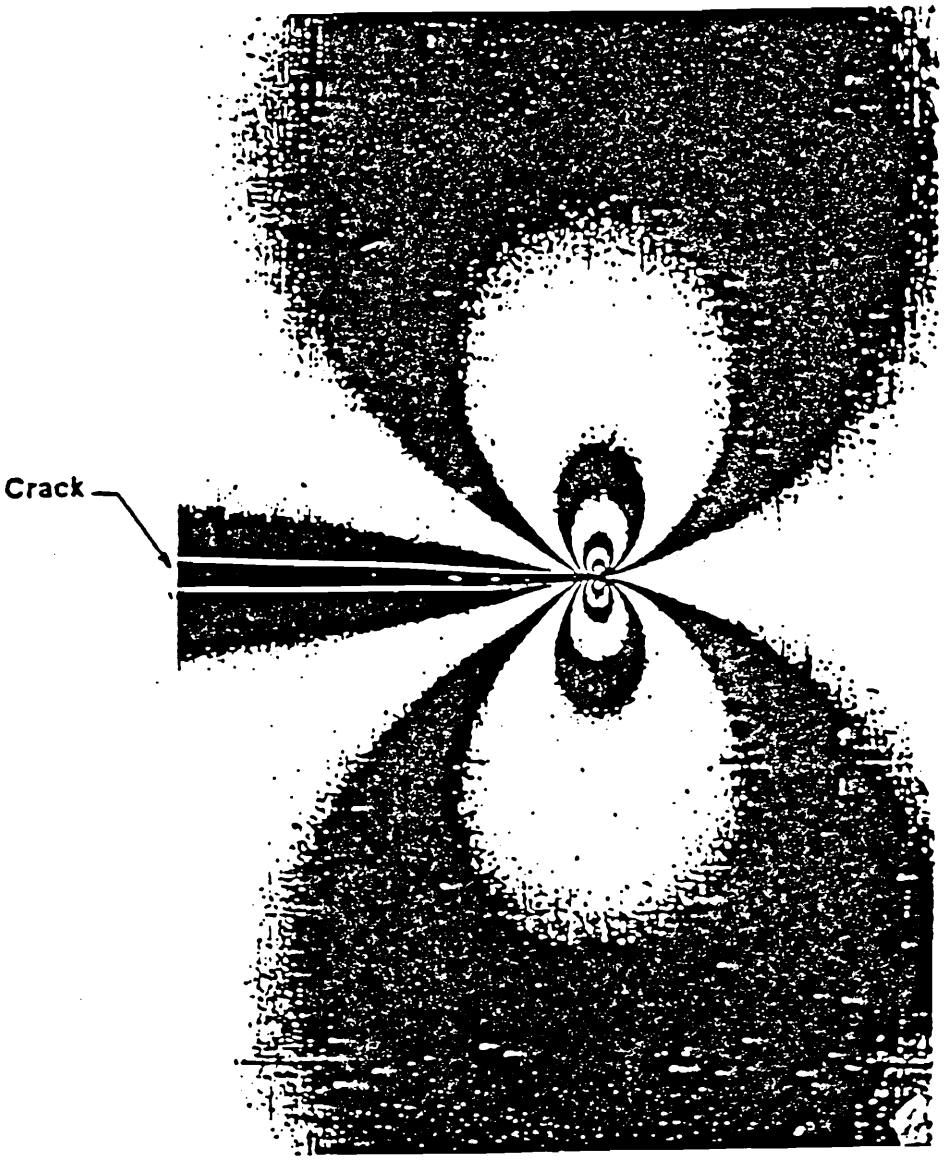

Figure 3.3. A typical mode I isochromatic pattern

3.4 Specimen Preparation

Cylinders with star-shaped cutouts were cast by the Measurement Group Laboratories. The dimensions of a specimen are shown in Fig.(3.2). A hole with 0.25″ (6.4mm) diameter is drilled through the wall of the cylinder with star-shaped cutout in order to receive a special sharp round tipped blade Fig.(3.4) held normal through the hole to touch the center of a diametrically opposite finger. A natural starter crack is inserted into the cylinder by striking the special blade held normal to the inner surface of the centerline of a star finger with a hammer. A single starter crack emanates dynamically a short distance from the blade tip and quickly arrests.

After the crack was made, using ″ liquid plastic ″ PLM-9 (supplied by the Measurement Group Laboratories) as adhesive, a small epoxy PLM-9 plug of about 0.25″ (6.4mm) diameter was inserted to fill the drilled hole. Furthermore, using a band saw, two 4.5″x4.5″ (11.4cmx11.4cm) PSM-9 plates were cut as top and bottom end caps. A hole was drilled through the middle of the bottom end cap in order to let the pressure hose pass through it. Then, liquid plastic PLM-9 was used again to bond the top and bottom caps together with the cylinder with star-shaped cutout Fig.(3.5).

3.5 Calibration Test and Determination of the Critical Temperature

Although the specimen material was PLM-9 , some difference from batch to batch for the value of the stress fringe constant and critical temperature occurred. For this reason, it is always necessary to calibrate each batch of photoelastic material at the time of the test [51].

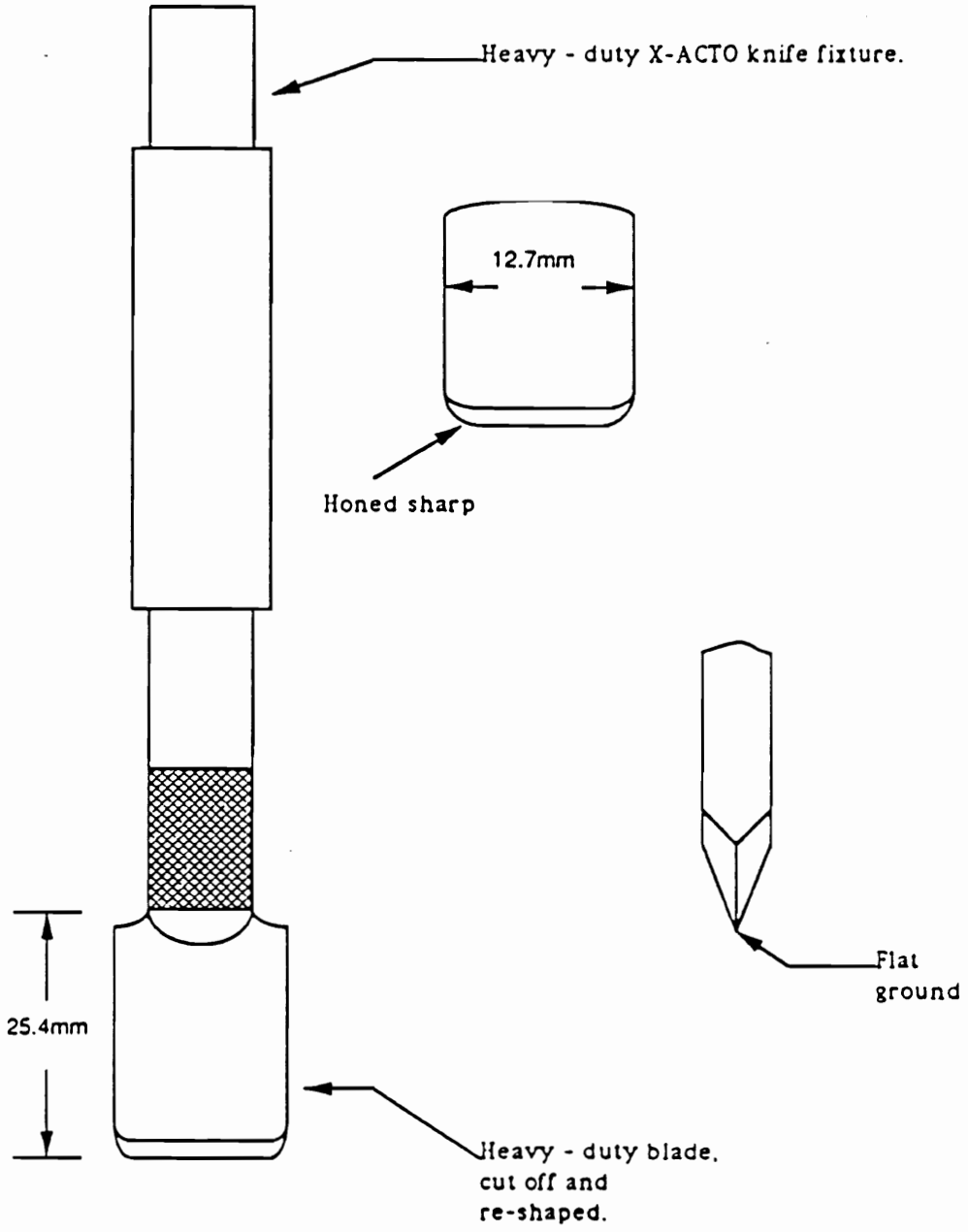

Figure 3.4. Dimension of a special sharp round tipped blade

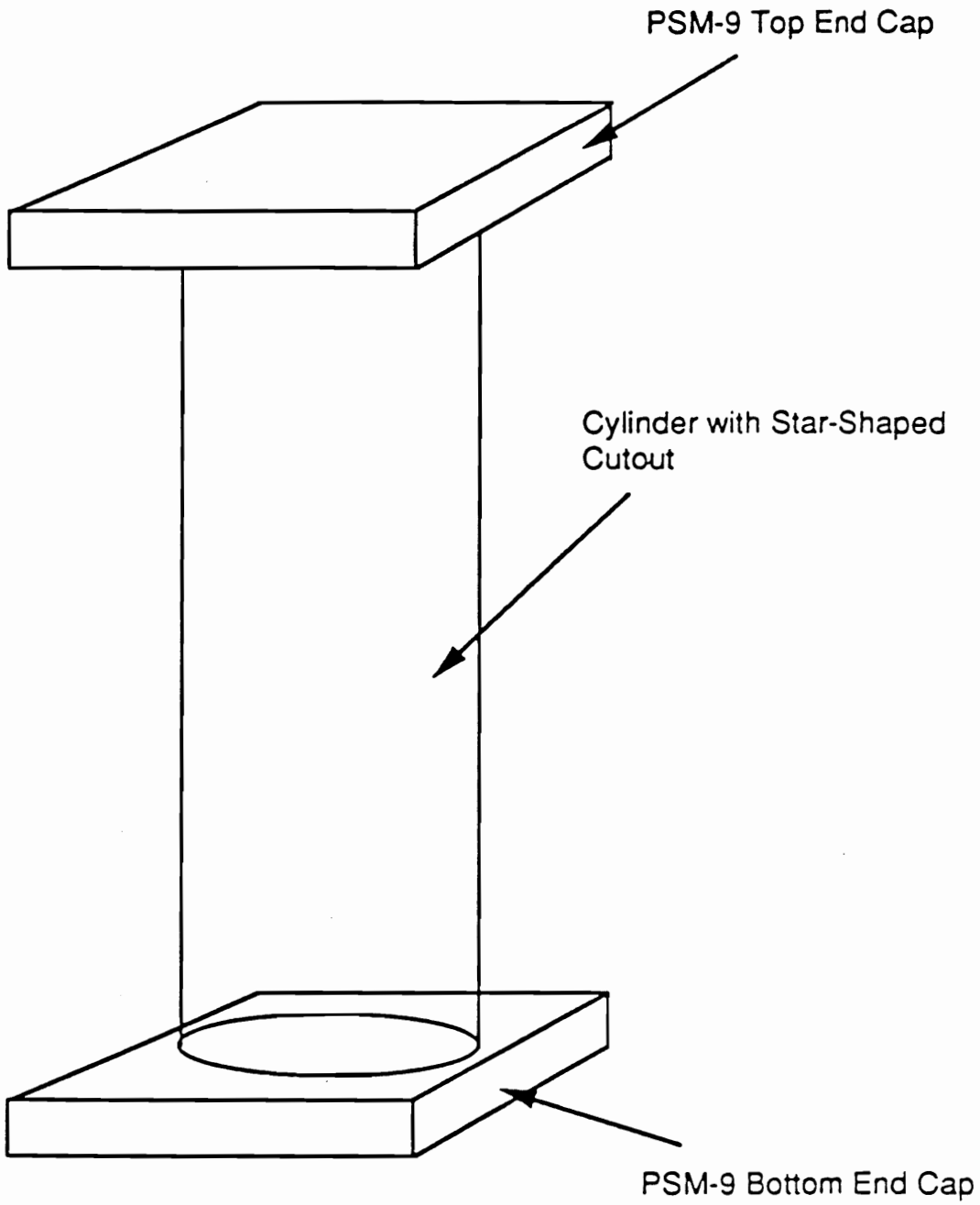

Figure 3.5. Cylinder with star-shaped cutout bond with end caps

A beam of 1"x 8"x 0.5" (25.4mm x 203.2mm x 12.7mm) was made of PLM-9 which was manufactured from the same batch as the cylinder with star-shaped cutout. Then, using a guide, four holes with 0.25" (6.4mm) diameter were drilled as shown in Fig(3.6). Fig.(3.6) presents the set-up of the calibration test. The beam was placed in the thermally-controlled oven. Then the beam was stress frozen. Two polariscope sheets were put on front and back of the oven in order to locate the critical temperature. Fringe data read from the center of the beam were used with the bending theory to determine the fringe constant. The results of the tests for critical temperature and stress fringe constant are shown in Table 4.

3.6 Experimental Set-up

Test specimens were placed in a thermally-controlled oven. A hole is drilled through the middle of the bottom plate to let the air pressure hose pass through. The test specimens have 27lbs (12.3Kg) weight on the top of the cap. This weight is approximately equal to the vertical force due to the internal pressure p = 6.9psi (47.6kPa) that the compressed air supplies. The set-up allows the free longitudinal thermal expansion of the cylinder with a star-shaped cutout with the dead weight on the top of the cylinder so as to effectively eliminate axial stresses in the cylinder. The loading system consists of (a) pressure gauge (b) pressure regulator (c) air valve.

The pressure regulator is a Model 10 Kendall Air Regulator manufactured by Fairchild Industrial Products Division. A pressure regulator along the pressure air passage can keep a constant pressure inside the cylinder with star-shaped cutout in case there is a small leak from the bonding seam of the cylinder and the caps. Simultaneously, the pressure regulator also can provide a uniform pressure independent of the supply pressure.

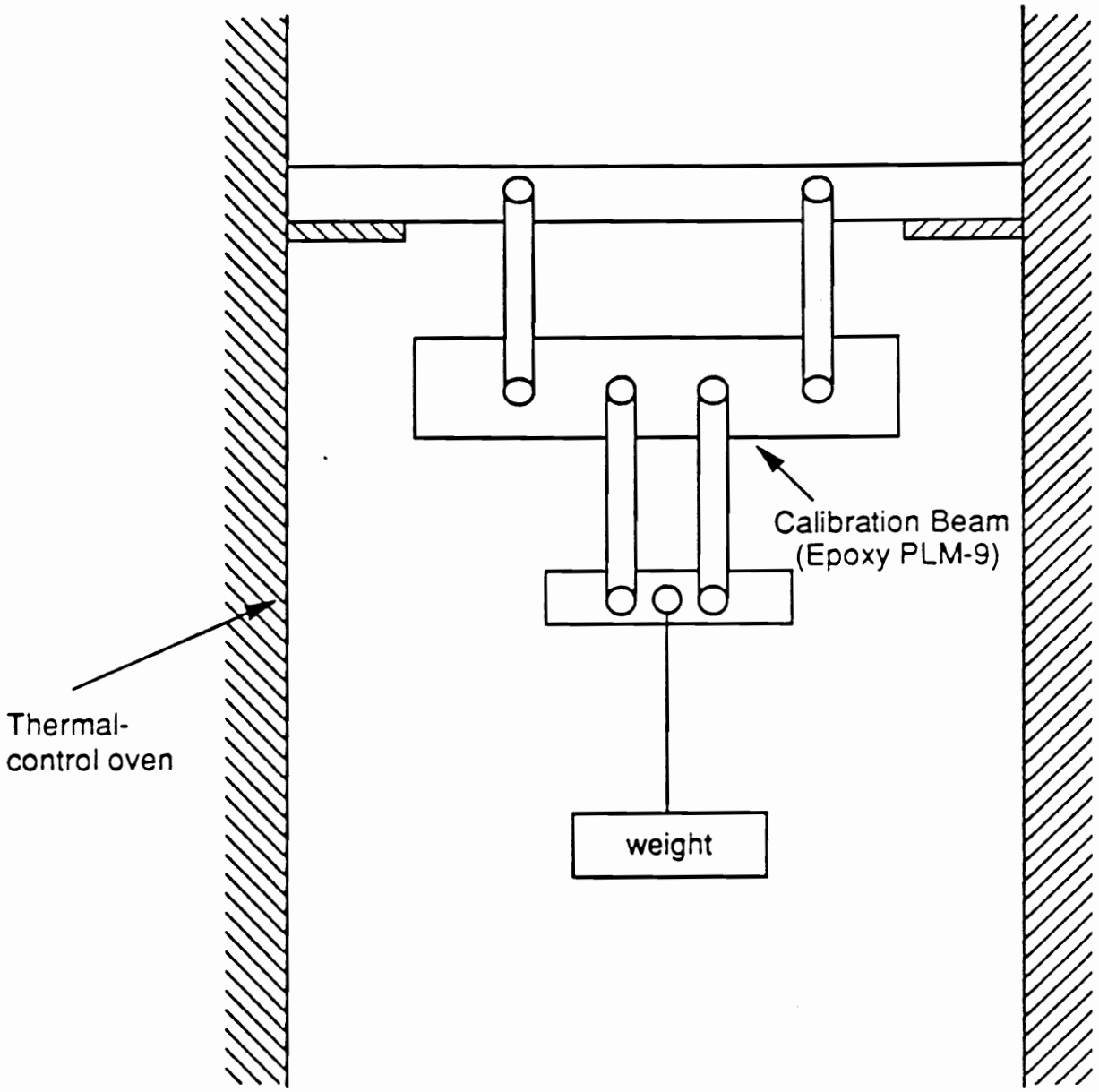

Figure 3.6. The set-up of calibration test

Table 4. Epoxy PLM-9's critical temperature and fringe constant

Test #	Stress Fringe Constant "f" psi/fringe/in (kPa/fringe/m)	Critical Temperature T^0F (T^0C)
T0	2.68 (0.49)	245 (118.3)
T1	2.68 (0.49)	235 (112.7)
T2	2.66 (0.49)	235 (112.7)
T3	2.59 (0.48)	235 (112.7)
T4	2.63 (0.48)	235 (112.7)
T5	2.77 (0.51)	235 (112.7)
T6	2.48 (0.45)	235 (112.7)
T7	2.73 (0.50)	235 (112.7)

The pressure gauge is a Model LM Heise Gauge manufactured by Heise Bourdon Tube Company, Inc.. It is a very sensitive pressure gauge. It registers 0.006 psig (0.00414 Newton/cm) by its smallest scale and can measure from 0 psig (0 Newton/cm) to 30 psig (20.685 Newton/cm). Its maximum hysteresis is 0.03 psig (0.0207 Newton/cm) at room temperature and it is accurate to 0.1% of full scale, including the effect of the hysteresis.

A compressed air tank supplies the pressurized air. The air passes through the air valve, the regulator and pressure gauge. The loading system is shown in Fig.(3.7).

3.7 Experimental Procedures

After stress freezing, the stress in the material is given by the stress-optical law [52]

$$\tau_{max} = \frac{nf}{2t} \tag{3.1}$$

where

τ_{max} : maximum in-plane shearing stress

n : isochromatic fringe order

f : stress fringe constant

t : the thickness of the slice

The test procedure was as follows.

(1) Tap in a natural starter crack smaller than desired size. Section 3.4 shows the detail of the blade and holder.

(2) The second step involves stress freezing in a thermally- controlled oven. Fig.(3.8) shows the freezing stress cycle. When the temperature rises to the critical temperature, sufficient pressure is applied to grow the crack to its desired size. It is

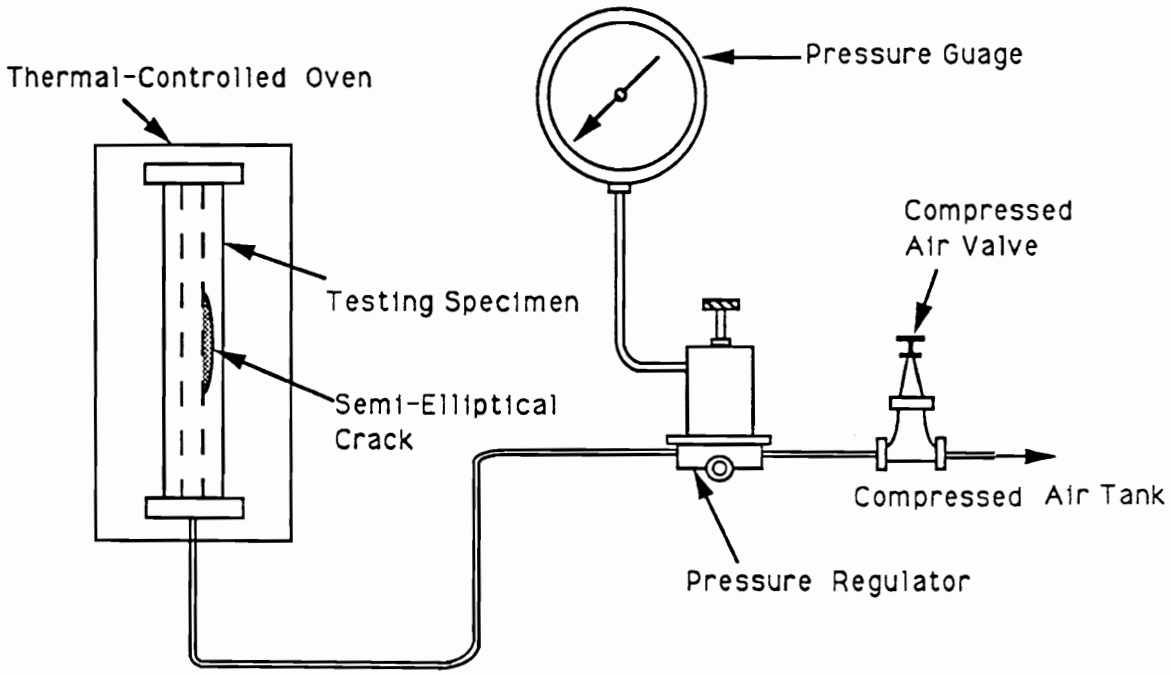

Figure 3.7. Experimental set-up and loading system

important that the test specimen have a certain amount of dead weight on the top of the end cap. The weight is approximately equal to the internal pressure multiplied by the area of the star-shape on the top of the model in order to eliminate the longitudinal axial stress in the cylinder with star-shaped cutout. After the starter crack extends to the desired size, then the internal pressure is reduced in order to stop the crack growth.

(3) The pressurized model is cooled to the room temperature, at the cooling rate of 2.5^{0}F/hr. Pressure removal will produce negligible recovery. The specimen is sliced without altering the fringe or deformation patterns and in plane mutually orthogonal to the crack border and flaw surface (parallel to the nz plane in Fig.(3.9)). Fig(3.10) shows the geometry of the cracked test model and slice locations. The thickness of the slices is about 0.5mm. Then, a thick ring slice is removed about 50.8mm from the end cap which is about 12.7mm thick. Fig.(3.11) shows the symmetrical stress fringe patterns for the ring slice. A Buehler Isomet diamond saw [53] is used to cut thin slices from the stress frozen models. The diamond saw blade turns at adjustable slow speeds between 0 and 300 rpm. The bottom part of the saw blade rotates through an oil which acts as a coolant and lubricant. That means, by using low speed and the oil one can minimize heat in the slice and eliminate heat induced birefringence in the slice. The slices are then stored in an oven to avoid moisture absorption. A photograph of a crack profile taken from the frozen specimen is shown in Fig.(3.12). Fig.(3.13) shows a typical near crack-tip fringe pattern for an interior slice.

(4) These slices are analyzed in a fringe multiplication system by using both the Partial mirror fringe multiplication [48-49] and the Tardy method [47] for the photoelastic analysis. The system used to analyze the slice is shown in Fig.(3.14). The system consists of a Model 051 photoelastic polariscope fitted with a set of partial mirrors and a laser light source. Appendix A briefly discusses the system. This system allows the tandem application of the Post partial mirror fringe multiplication and

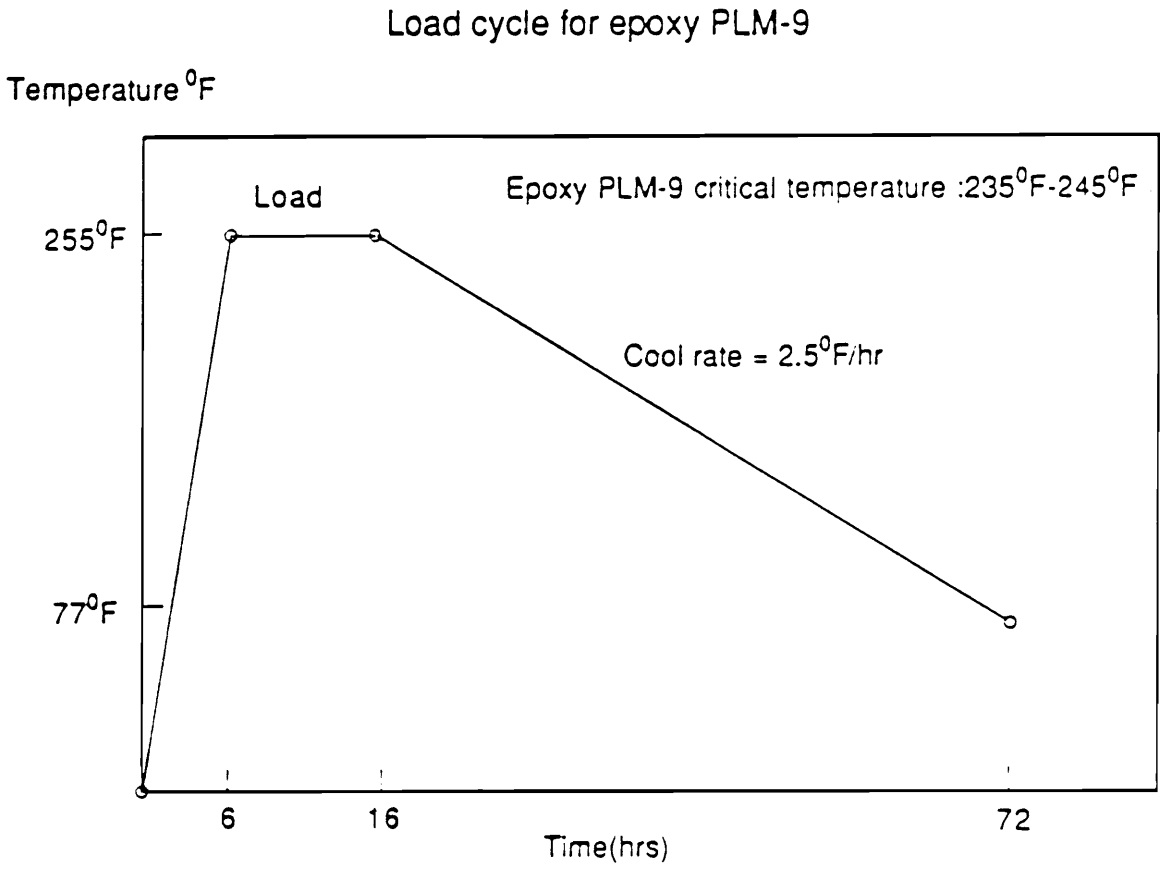

Figure 3.8. Epoxy PLM-9 freezing stress cycle

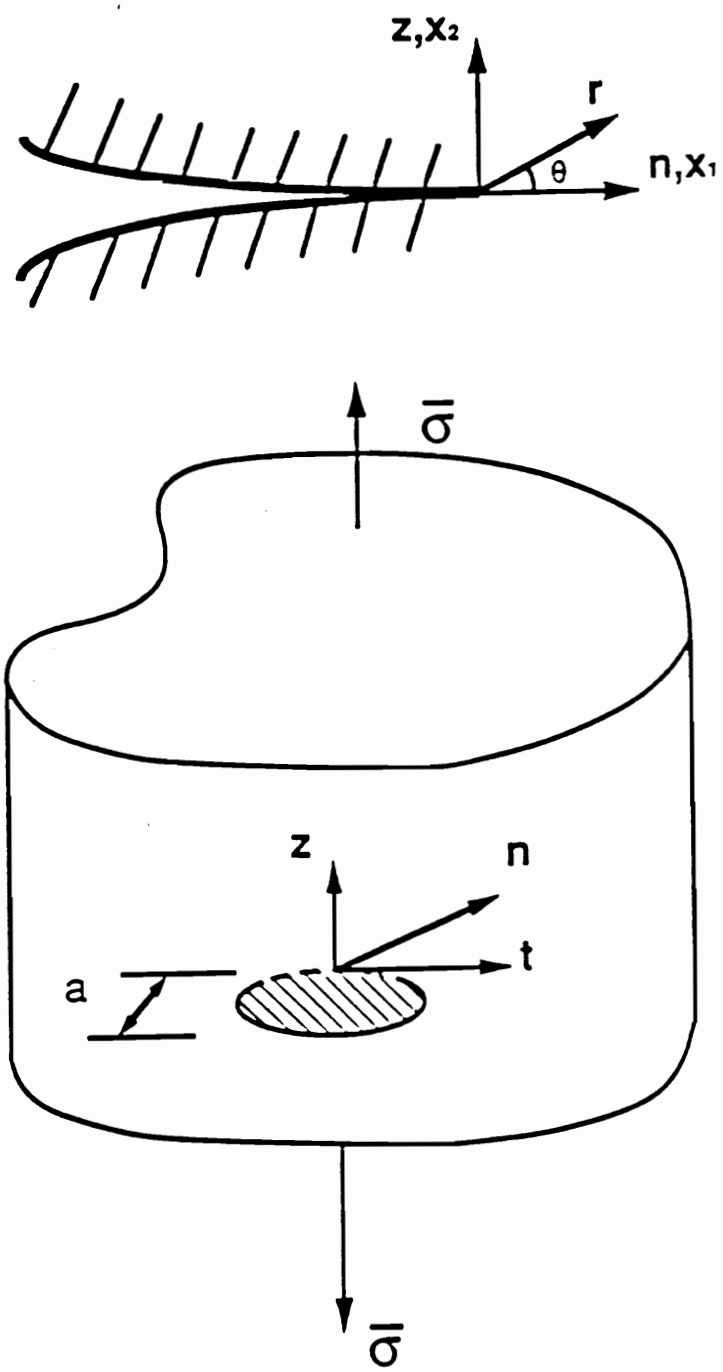

Figure 3.9. Near tip coordinates

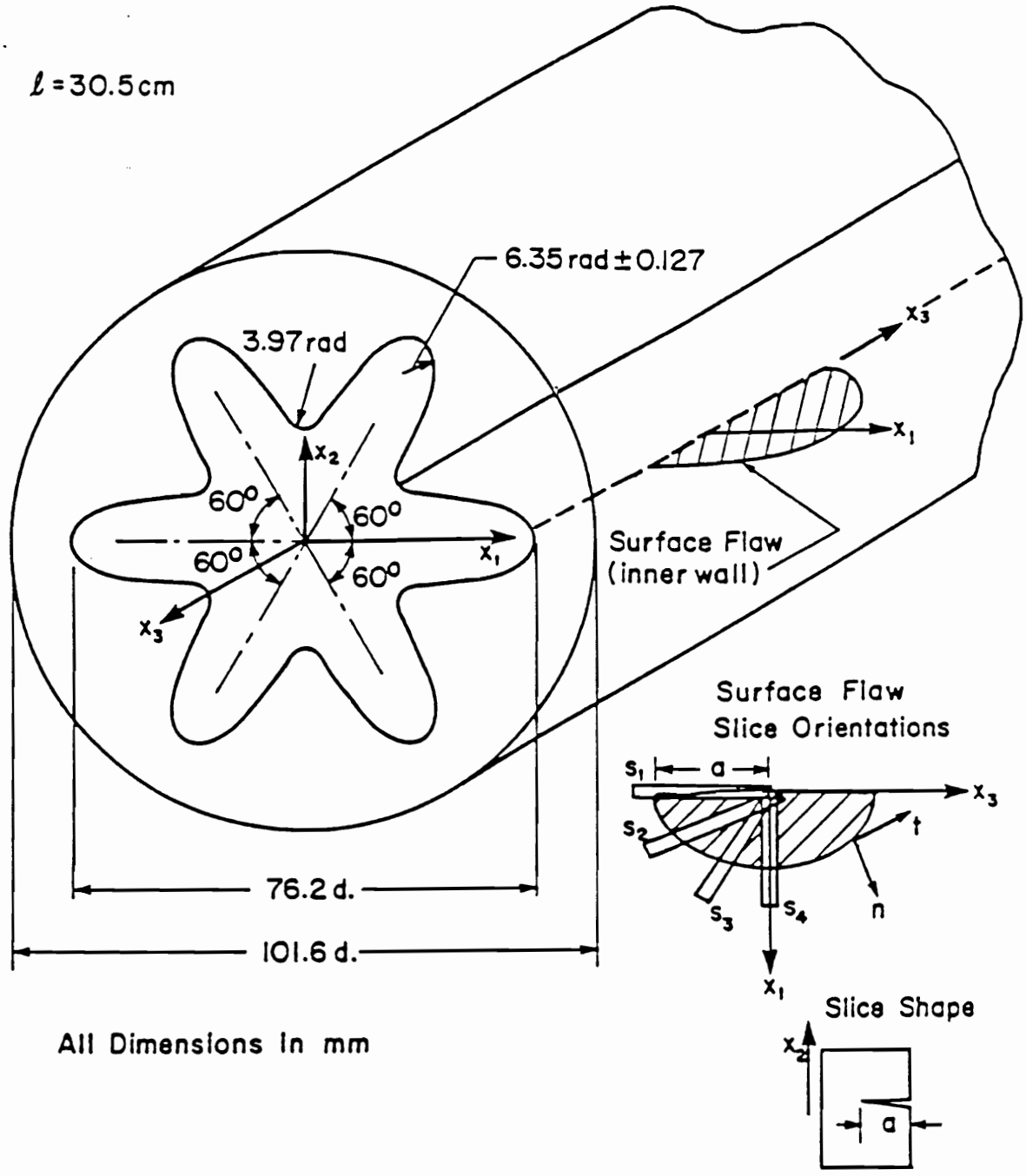

Figure 3.10. The geometry of cracked test model and slice locations

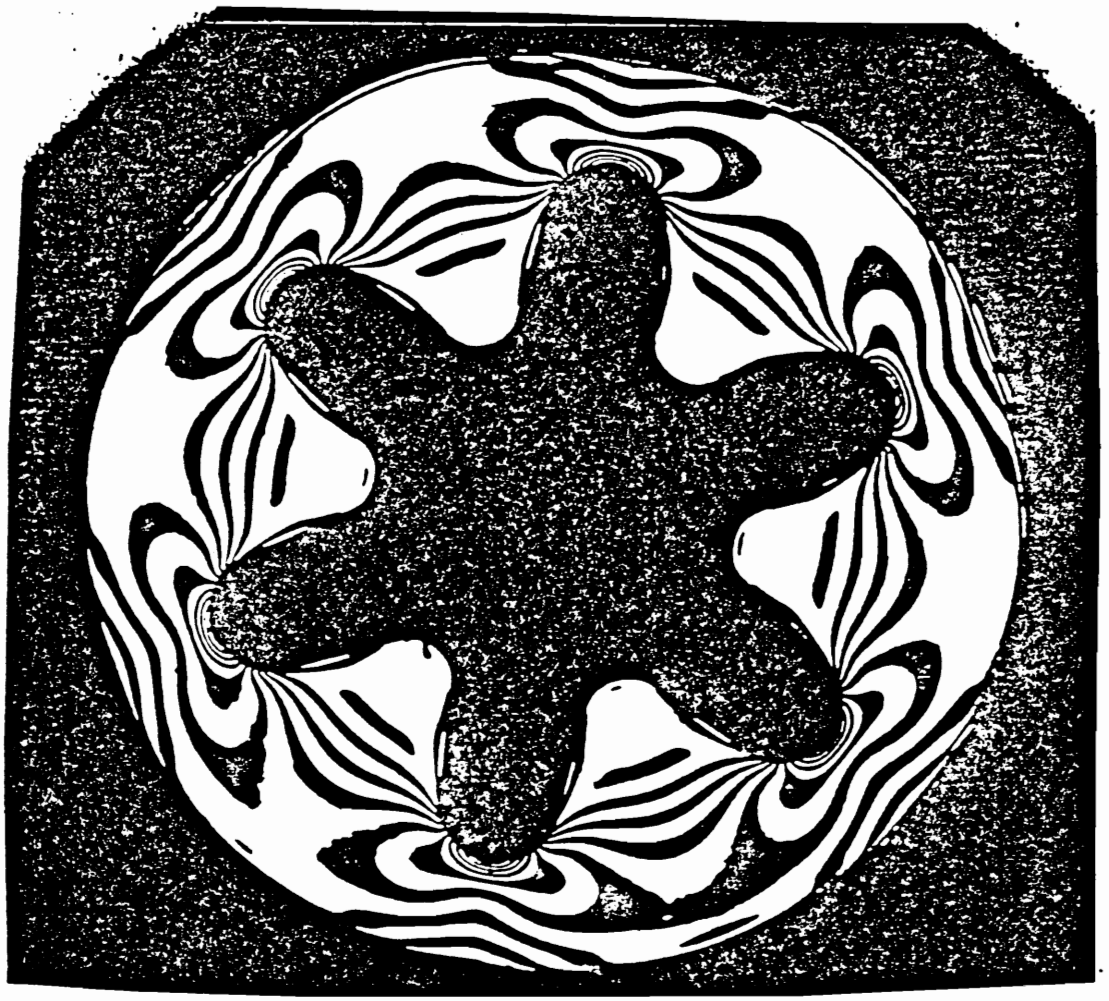

Figure 3.11. Stress fringe patterns of the ring slice (Thickness = 12.7mm)

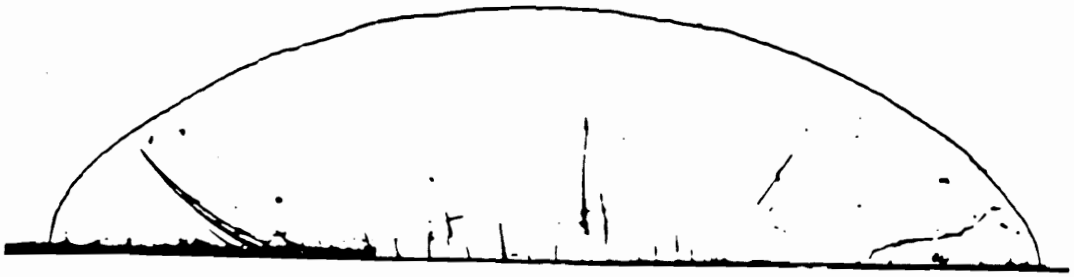

Figure 3.12. The picture of the crack profile

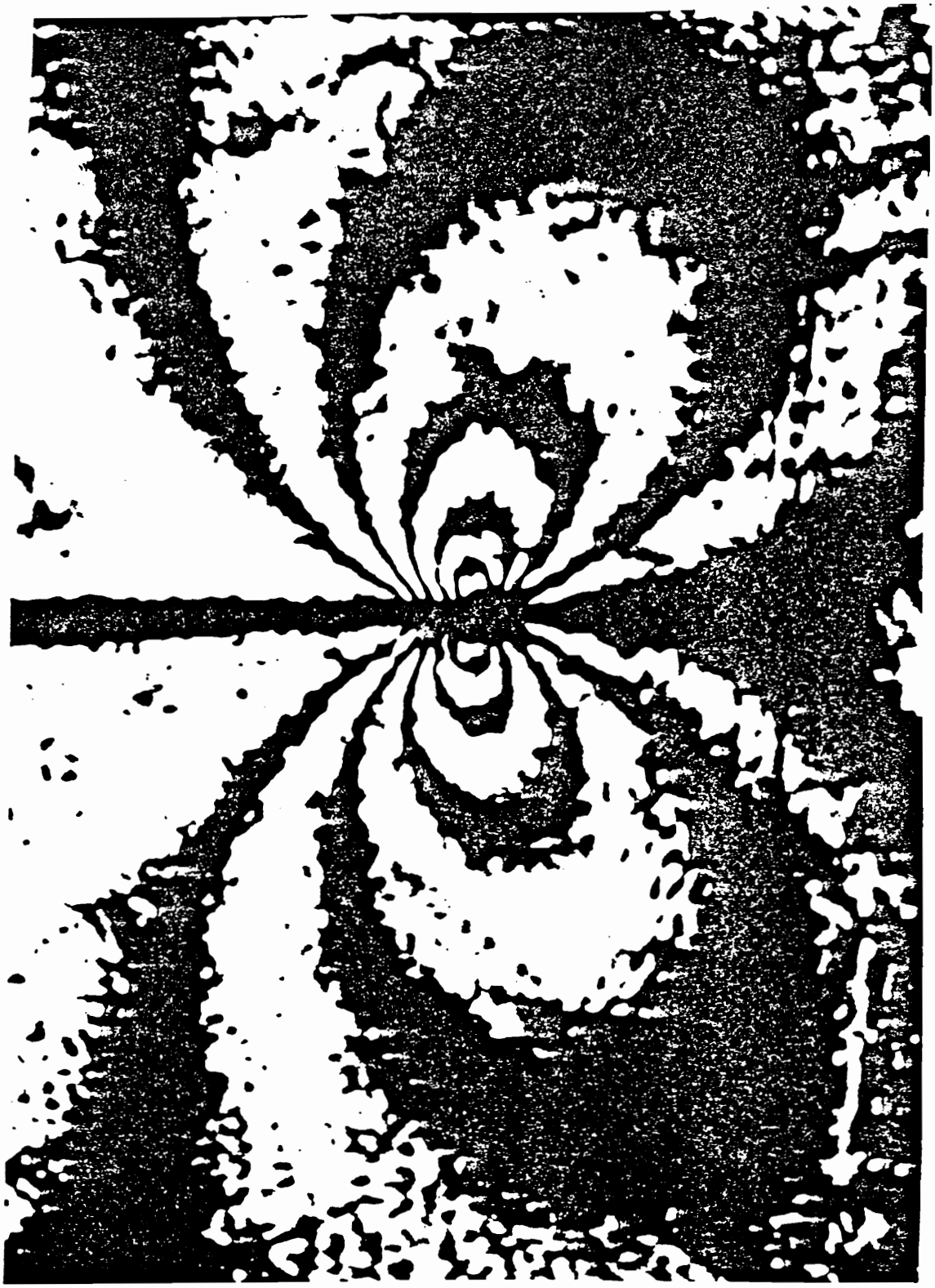

Figure 3.13. A near crack tip fringe pattern for interior slice with multiplications of 9

Tardy compensation. In this system, one can keep loads small in order to avoid large deformation around the crack tip. Fig.(3.15) shows fringe patterns with multiplications of 1, 5, 17. The data are taken along the line $\theta = \frac{\pi}{2}$. Then , the technique of Tardy compensation is used to obtain fractional fringe orders and thus allow computation of $K_{I(AP)}$ at many points near the crack tip. The $K_{I(AP)}$ is called an "apparent" stress intensity factor which will be described in the next chapter. The analysis of the surface slice is the most difficult part, due to the fact that the surface slice has a variable thickness. The variation of thickness must be considered in the photoelastic analysis. Fig.(3.16) shows the surface slice with variable thickness in the fringe multiplication unit. In order to consider this effect, a computer program called " T-0 sas " (see Appendix B) is developed.

(5) The fringe order data are digitized and fitted to an algorithm described in chapter 4 for converting photoelastic data into stress intensity factors. Then, using a least squares fit to establish a linear $\frac{(K_I)_{AP}}{p(\pi a)^{1/2}}$ versus $(\frac{r}{a})^{1/2}$ zone, the linear part can be extrapolated across the non-linear zone to determine the normalized stress intensity factor $\frac{K_I}{p(\pi a)^{1/2}}$ at the crack tip. That means the mode I linear elastic fracture mechanics (LEFM) algorithm for photoelastic data allows extraction of stress intensity factors values for each slice. We also find a linear zone where the crack border intersects an inner star surface and Benthem's analysis [14] - [17] suggests that the inverse square root singularity order no longer exists at the inner star boundary. The algorithm for this case is also described in chapter 4.

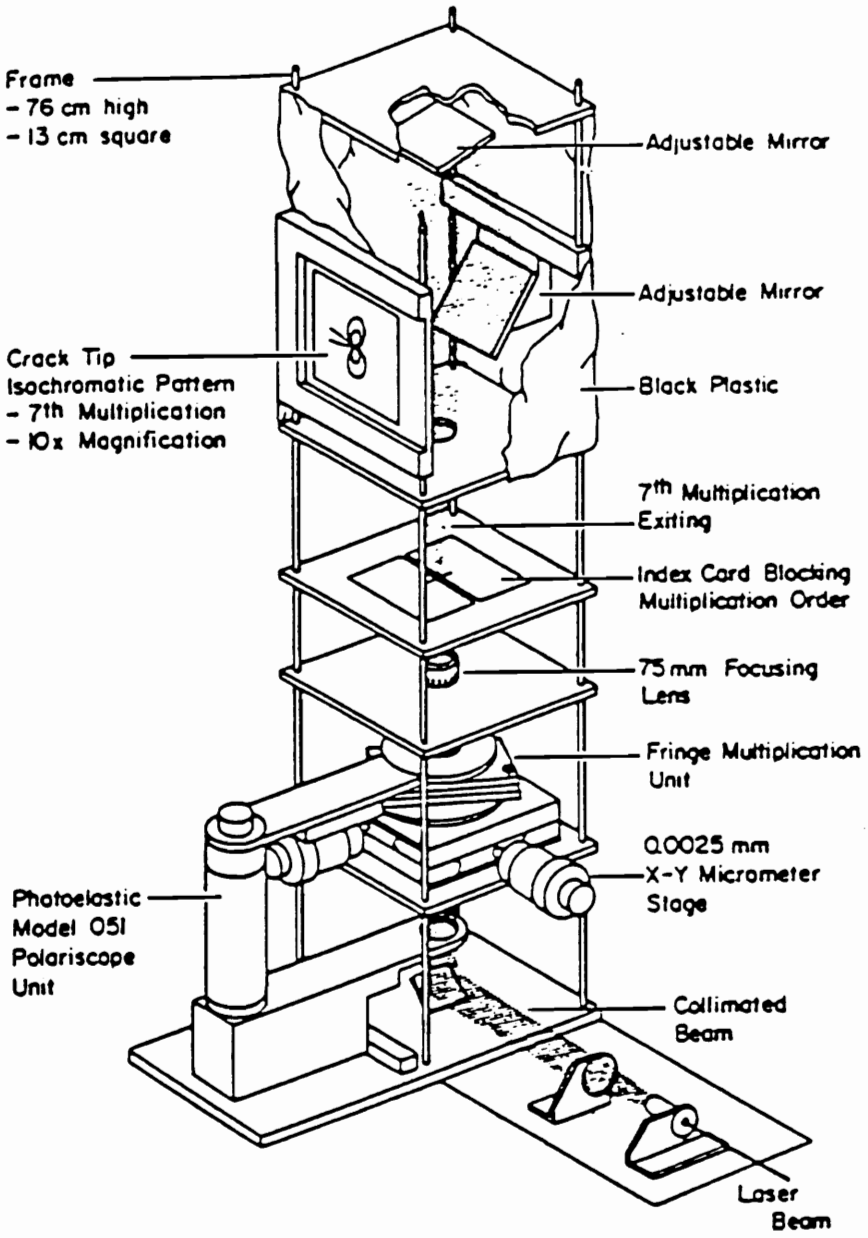

Figure 3.14. The fringe multiplication system [36]

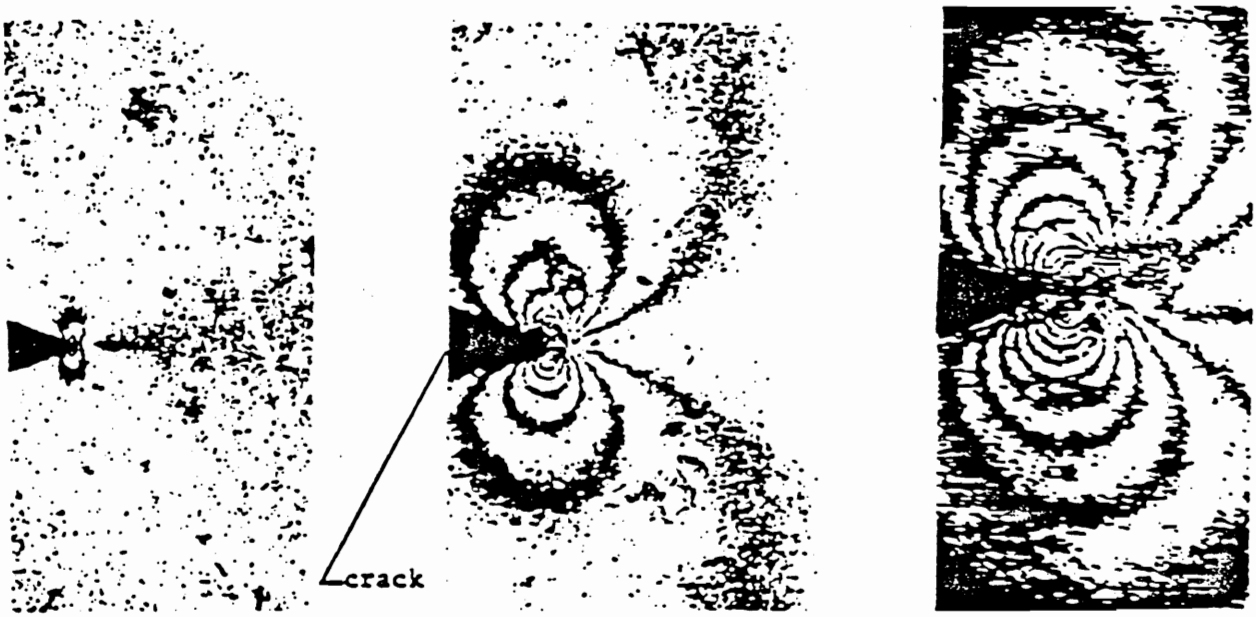

Figure 3.15. Fringe patterns with multiplications of 1, 5, 17 [36]

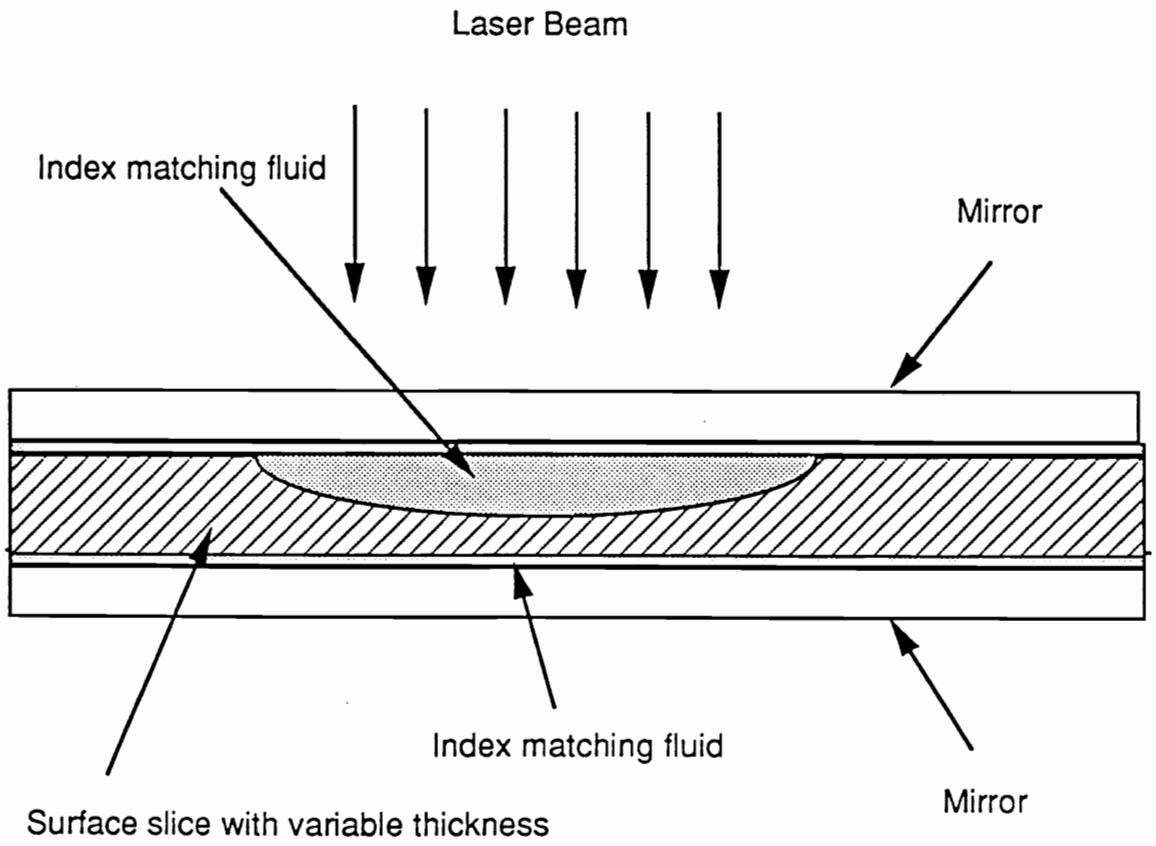

Figure 3.16. Surface slice with variable thickness in the multiplication unit

4.0 Analytical Considerations

4.1 Introduction

Irwin [54] introduced the concept of the stress intensity factor (S.I.F) with its inverse square root stress singularity. The same form of singularity order was used by Williams [55] in his two-dimensional eigenfunction biharmonic expansion. Kassir and Sih [56] extended the concept of the inverse square root singularity to three-dimensional elliptical flaws embedded in infinite bodies.

Sih noted that the inverse square root singularity existed along a flaw border in the interior, but the order is no longer half when the crack intersected a free surface. Benthem [17] used three-dimensional separation of variables for a quarter infinite crack in half space and also found a loss of the inverse square root singularity.

Irwin [54] was the pioneer of experimental procedures to determine the mode I stress intensity factors for two-dimensional problem. Smith [57] has developed the technique for extracting the value of the stress intensity factor from photoelastic data for both two and three-dimensional problems.

4.2 Mode I LEFM Algorithm for Photoelastic Data

Sih and Kassir [56] have demonstrated that for the case of an embedded elliptical flaw, the singular stresses lie in a plane mutually orthogonal to the flaw border and the crack surface. It may take the same functional form as the Irwin [54] field equations for the two-dimensional problem by using a set of local coordinate axes Fig.(3.9). Using this concept, we may describe the near-tip stresses in LEFM for two-dimensional problems as:

$$\sigma_{ij} = \frac{K_I}{(2\pi r)^{\frac{1}{2}}} f_{ij}(\theta) - \dot{\sigma_{ij}}(\theta) \qquad i,j = 1,2 \tag{4.1}$$

where:

σ_{ij} = near-tip in-plane singular stress components

K_I = Mode I Stress Intensity Factor (SIF)

$\dot{\sigma_{ij}}$ = near-tip contribution of non-singular stresses.

From experience, in three-dimensional problems the $\dot{\sigma_{ij}}$ terms may vary in the t direction along the flaw border, but they can be considered constant along a normal to the flaw plane at a point on the border. From Eq. (4.1), we may write:

$$\sigma_{11} = \frac{K_I}{(2\pi r)^{\frac{1}{2}}} \cos\frac{\theta}{2}\left[1 - \sin\frac{\theta}{2}\sin\frac{3\theta}{2}\right] - \dot{\sigma} \tag{4.2a}$$

$$\sigma_{22} = \frac{K_I}{(2\pi r)^{\frac{1}{2}}} \cos\frac{\theta}{2}\left[1 + \sin\frac{\theta}{2}\sin\frac{3\theta}{2}\right] \tag{4.2b}$$

$$\sigma_{12} = \frac{K_I}{(2\pi r)^{\frac{1}{2}}} \left[\sin\frac{\theta}{2}\cos\frac{\theta}{2}\cos\frac{3\theta}{2}\right] \tag{4.2c}$$

where (r,θ) are polar coordinates with origin at the crack tip. From the maximum shearing stress :

$$\tau_{max}^2 = \frac{1}{4}\{(\sigma_{11} - \sigma_{22})^2 + 4\sigma_{12}^2\} \tag{4.3}$$

By measuring the photoelastic stress fringes from the mode I loading in a direction normal to the crack plane $\theta = \frac{\pi}{2}$ and substituting Eq.(4.2) into (4.3) and expanding the equation in a series form with truncation to the same order as equation (4.2), then we obtain:

$$\tau_{max}^2 = \frac{K_I^2}{8\pi r} + \frac{k_I \dot{\sigma}}{4(\pi r)^{\frac{1}{2}}} + \frac{(\dot{\sigma})^2}{4} \tag{4.4}$$

From the equation (4.4), where $(\dot{\sigma})^2$ is small relative to $8\tau_{max}^2$ and $\frac{\dot{\sigma}}{\sqrt{8}}$ represents the contribution of the non-singular stress state to the maximum shear stress, τ_{max} is in the X_1X_2 plane:

$$\tau_{max} = \frac{K_I}{(8\pi r)^{\frac{1}{2}}} + \frac{\dot{\sigma}}{\sqrt{8}} \tag{4.5}$$

From the stress optical law [52], the equation for relating the maximum in-plane shear stress to the isochromatic fringe order is:

$$\tau_{max} = \frac{nf}{2t} \tag{4.6}$$

where:

n = photoelastic fringe order

f = material fringe value

t = thickness of slice

Now define an "apparent" S.I.F

$$(K_I)_{AP} = \tau_{max}(8\pi r)^{\frac{1}{2}} \tag{4.7}$$

and normalizing with respect to $p(\pi a)^{\frac{1}{2}}$

where:

p = internal pressure

a = depth of the semi-elliptical crack

Then we write:

$$\frac{(K_I)_{AP}}{p(\pi a)^{\frac{1}{2}}} = \frac{K_I}{p(\pi a)^{\frac{1}{2}}} + \frac{\dot{\sigma}}{p}\left(\frac{r}{a}\right)^{\frac{1}{2}} \tag{4.8}$$

From the Eq.(4.8) one can find the linear zone in a plot of $\frac{(K_I)_{AP}}{p(\pi a)^{\frac{1}{2}}}$ versus $\left(\frac{r}{a}\right)^{\frac{1}{2}}$ with a slope $\frac{\sigma^0}{p}$. By taking sufficient photoelastic data and fitting a straight line in the linear zone, the line can be extrapolated across the non-linear zone very close the crack tip to the origin in order to obtain an accurate estimate of $\frac{K_I}{p(\pi a)^{\frac{1}{2}}}$.

4.3 Photoelastic Algorithm Accounting for Variable Eigenvalue

By combining Benthem's analysis with the above LEFM approach, one can construct a variable λ algorithm to describe a quasi two dimensional stress state for layers inside the body normal to the flaw border and the crack surface as follows: Using Benthem's analysis and the LEFM results as a guide, one may construct a two dimensional stress function $f(\zeta)$of the form:

$$Z = \frac{f(\zeta)}{\zeta^{\lambda_\sigma}} \tag{4.9}$$

where λ_σ is the stress singularity order. ζ is a complex variable ($re^{i\theta}$). Expanding $f(\zeta)$ in a MacLaurin series about the crack tip, one gets:

$$f(\zeta) = \frac{K_{\lambda_\sigma}}{\sqrt{2\pi}} + a_1\zeta + a_2\zeta^2 + \cdots \tag{4.10}$$

where K_{λ_σ} may be designated as a stress eigenfactor. For the plane problem [58], [59],

$$\sigma_{11} = Re(Z) - x_2 Im(Z') \tag{4.11a}$$

$$\sigma_{22} = Re(Z) + x_2 Im(Z') \tag{4.11b}$$

$$\sigma_{12} = -x_2 Re(Z') \tag{4.11c}$$

where:

$$Re(Z') = \frac{\partial Re(Z)}{\partial x_1} = \frac{\partial Im(Z)}{\partial x_2} \tag{4.12}$$

Now substituting Eq.(4.10) in Eq.(4.11), one obtains:

$$\sigma_{11} = \frac{K_{\lambda_\sigma}}{\sqrt{2\pi}\, r^{\lambda_\sigma}} \{ \cos \lambda_\sigma\theta - \lambda_\sigma \sin\theta \sin(\lambda_\sigma + 1)\theta\} - \dot{\sigma} \tag{4.13a}$$

$$\sigma_{22} = \frac{K_{\lambda_\sigma}}{\sqrt{2\pi}\, r^{\lambda_\sigma}} \{ \cos \lambda_\sigma\theta + \lambda_\sigma \sin\theta \sin(\lambda_\sigma + 1)\theta\} \tag{4.13b}$$

$$\sigma_{12} = \frac{K_{\lambda_\sigma}}{\sqrt{2\pi}\, r^{\lambda_\sigma}} \{\lambda_\sigma \sin\theta \cos(\lambda_\sigma + 1)\theta\} \tag{4.13c}$$

where:

$K_{\lambda\sigma}$ = the stress eigenfactor.

λ_σ = the stress singularity may be different from $\frac{1}{2}$.

Furthermore, from the equation (4.13), one can calculate τ^2_{max} as follows:

$$\tau^2_{max} = \frac{1}{4} \{(\sigma_{11} - \sigma_{22})^2 + 4\sigma^2_{12}\} \tag{4.14}$$

and assuming $\frac{\dot{\sigma}(2\pi)^{\frac{1}{2}} r^{\lambda_\sigma}}{K_{\lambda_\sigma}\lambda_\sigma \sin\theta} < 1$ and truncating to the same order as Eqs.(4.13), one obtains [60]:

$$\tau_{max} = \frac{\lambda_\sigma K_{\lambda_\sigma} \sin\theta}{\sqrt{2\pi}\, r^{\lambda_\sigma}} + \frac{\dot{\sigma}}{2} \sin(\lambda_\sigma + 1)\theta \tag{4.15}$$

Along $\theta = \frac{\pi}{2}$, Eq.(4.15) reduces to

$$\tau_{max} = \lambda_\sigma \frac{K_{\lambda_\sigma}}{\sqrt{2\pi}\, r^{\lambda_\sigma}} + \frac{\dot{\sigma}}{2} \sin(\lambda_\sigma + 1)\frac{\pi}{2} = \lambda_\sigma \frac{(K_{\lambda_\sigma})_{AP}}{\sqrt{2\pi}\, r^{\lambda_\sigma}} \tag{4.16}$$

and for $\lambda_\sigma = \frac{1}{2}$, the LEFM case is recovered. Meanwhile, one expects LEFM to prevail away from the inner star boundary, so one may assume $\lambda_\sigma = \frac{1}{2}$; then one can obtain $\dot{\sigma}$ from the slope of a plot of $\frac{(K_I)_{AP}}{p(\pi a)^{\frac{1}{2}}}$ versus $(\frac{r}{a})^{\frac{1}{2}}$ to determine the value of the non-singular term on the right side of Eq.(4.15). Then define τ_0 as

$$\tau_0 = \frac{\dot{\sigma}}{2} \sin(\lambda_\sigma + 1)\frac{\pi}{2} \tag{4.17}$$

From Eq.(4.17), τ_0 varies as λ_σ varies. At the inner star surface the value of τ_0 is different from the τ_0 in the interior of the specimen. That means that the LEFM determinations of $\dot{\sigma}$ shows that it begins to change significantly a short distance from the inner star surface. From the Eq.(4.3), in LEFM, one defines $\tau_0 = \frac{\dot{\sigma}}{\sqrt{8}}$. Thus τ_0 can be determined from the slope of the normalized K_{IAP} versus $\sqrt{r}$ plot. Owing to the geometry of the star-shape, the slice's thickness t is variable at the inner star surface. Then we use the variable thickness of the slice to calculate λ_σ and K_I. However the LEFM algorithm is expected to prevail away from the inner star surface. Then one assumes that τ_0 is a constant value for the inner region at different points along the crack border, where plane strain dominates, and the value of τ_0 is assumed zero at the inner star surface. Comparison of surface slice data with moire results in prior work has indicated that τ_0 approaches zero at the free surface, and that assumption is made in this work. From Eq.(4.15), τ_{max} reduces to:

$$\tau_{max} = \lambda_\sigma \frac{K_{\lambda_\sigma}}{\sqrt{2\pi}\, r^{\lambda_\sigma}} + \tau_0 \tag{4.18}$$

Then taking the natural log of both sides:

$$\ln(\tau_{max} - \tau_0) = \ln(\lambda_\sigma \frac{K_{\lambda_\sigma}}{\sqrt{2\pi}}) - \lambda_\sigma \ln r \tag{4.19}$$

When τ_0 is determined, one can plot $\ln(\tau_{max} - \tau_0)$ versus $\ln r$ and calculate λ_σ as the slope of the linear range.

5.0 Results and Conclusions

5.1 Introduction

The results of the experimental program consist of two major parts. The first one shows how to measure the stress singularity order " λ_σ ". The value of λ_σ is found near where the crack border of the specimen intersects the inner star surface. A series of frozen stress experiments have been conducted on surface flaws of varying aspect ratios in pressurized specimens in order to measure the lowest order stress singularity. The loss in the inverse square root singularity in the stress where the crack intersects the inner surface is most significant in nearly incompressible ($\nu = 0.50$) materials. Such materials include solid rocket propellants, composite material matrices and rubber, where the effect is maximized by the high Poisson's ratio. One goal of the study is to measure directly the value of the lowest order eigenvalue at the star surface where the crack intersects the inner star surface at right angles and to compare with Benthem's result.

Secondly, due to the lack of an analytical solution for measuring the distribution of the S.I.F along the crack border of the surface flaws in motor grain geometries, a

refined technique using the frozen stress photoelastic method was applied to estimate Mode I stress intensity factor distributions along the border of the surface flaws in cylinders with star-shaped cutouts under internal pressure. The resulting stress intensity factor distributions compare favorably with the predictions obtained in the Newman-Raju analysis of the surface flaws in pressurized circular cylinders and with the results of a weight function approach (two-dimensional analysis). In evaluating the results, it was found that surface slices in shallow cracks showed mixed mode behavior, and this is discussed in the section 5.5.

5.2 Results of the Stress Singularity Order for Photoelastic Tests

Using the variable λ_σ algorithm, the value of λ_σ can be determined, but the procedures are not straightforward because of the non-singular stress term in Eq.(4.15) and the three dimensional nature of the near-tip stress state at the inner star surface.

Since Linear Elastic Fracture Mechanics (LEFM) is expected to prevail away from the inner surface, the value of τ_0 can be determined there from LEFM. This means that using Eq.(4.8) one can plot $\frac{(K_I)_{AP}}{p(\pi a)^{1/2}}$ versus $(\frac{r}{a})^{1/2}$ to obtain a linear zone where the slope is proportional to τ_0.

From the variable λ_σ algorithm, one calculates τ_{max} from Eq.(4.15) along $\theta = \frac{\pi}{2}$ as one does in LEFM; then we obtain Eq.(4.16) and define $\tau_0 = \frac{\dot{\sigma}}{2} \sin(\lambda_\sigma + 1)\frac{\pi}{2}$. Next we can determine the value of τ_0 and plot $\ln(\tau_{max} - \tau_0)$ versus ln(r) to obtain λ_σ as the slope of the linear range. For the inner star surface, we cannot determine τ_0 by applying the LEFM algorithm. However, four point bending tests with moire grating on the free surface shows that, if τ_0 is set to zero at the free surface, there is a reasonable correlation between the photoelastic and moire data there. Therefore, one can assume that τ_0 decreases to zero at the free surface. Using this assumption, we can measure the

values of the stress singularity order at the inner star surfaces for the star-shaped cutout cylinders.

Experiments have been conducted on semi-elliptical cracks grown in the pressurized cylinders with star-shaped cutouts. The crack front shapes obtained in these tests are given in Fig.(5.1). Dimensions and geometry of the eight cylinders are shown in Table 5. The flaws are divided into three groups according to the depth of the cracks. The groups include the shallow crack (a/T = 0.25-0.32), the medium depth crack (a/T = 0.45-0.56), and the deep crack (a/T = 0.62-0.66).

Slices have been taken from symmetrical locations on both sides of the flaw. Fig.(5.2) shows an example of the determination of the non-singular stress $\dot{\sigma}/p$ for the deep crack in the plane strain region. According to the algorithm of chapter 4, Fig.(5.3) presents the value of the stress singularity order λ_o for the interior slice of the specimen at medium crack depth. By using the same approach, one can obtain the values of the stress singularity $\lambda_o = 1/2$ at the plane strain zone for shallow cracks and deep cracks. For the inner star surface slice, the values of the stress singularity order are given in Fig.(5.4)-Fig. (5.6).

Benthem [17], using a three-dimensional separation of variable approach for a quarter infinite crack in a half space, Fig.(2.6), shows that when the crack intersects a free surface at right angles, the square root singularity is lost; this effect is most significant in nearly incompressible materials. Benthem has found that the value of the lowest stress singularity order for Poisson's ratio of 0.5 is $\lambda_o = 0.33$. However, two different geometry specimens have been tested by Smith and his associates [40,41] under different loading conditions to measure the stress singularity order along the crack border. First, the four point bending specimens have been used to obtain straight front artificial cracks as shown in Fig.(2.18). Fig.(5.7) presents both photoelastic and moire

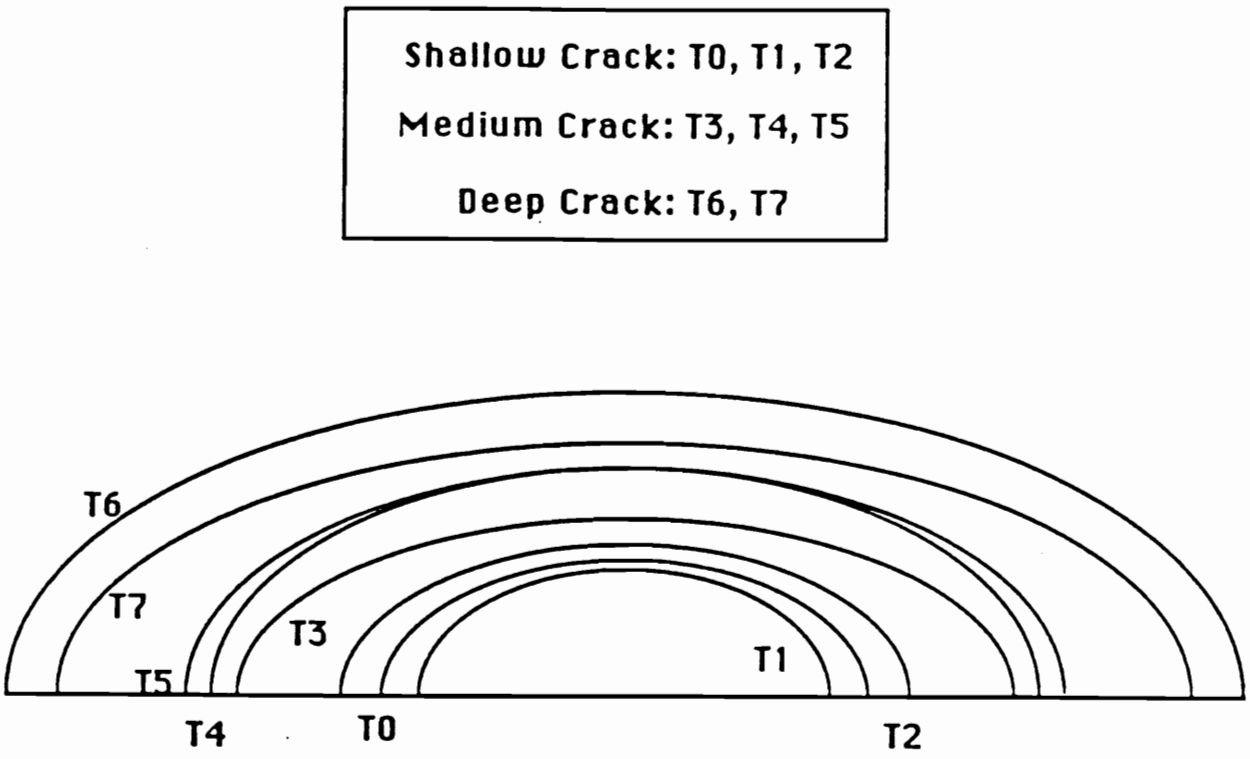

Figure 5.1. Crack front shapes for cylinder with star-shaped cutout

Table 5. Dimension and Geometry of the Test Specimens

Shallow Cracks Test	p psi (kPa)	a (mm)	c (mm)	a/c	a/T
T0	3.9 (26.9)	3.6	6.67	0.54	0.28
T1	6.9 (47.6)	3.2	6.15	0.52	0.25
T2	6.9 (47.6)	4.10	7.42	0.55	0.32
Medium Cracks Test	**p psi (kPa)**	**a (mm)**	**c (mm)**	**a/c**	**a/T**
T3	6.9 (47.6)	6.19	12.39	0.46	0.45
T4	6.1 (42.1)	6.60	12.7	0.52	0.52
T5	6.9 (47.6)	7.34	13.21	0.43	0.56
Deep Cracks Test	**p psi (kPa)**	**a (mm)**	**c (mm)**	**a/c**	**a/T**
T6	6.9 (47.6)	8.41	19.05	0.44	0.66
T7	6.9 (47.6)	7.90	17.53	0.45	0.62

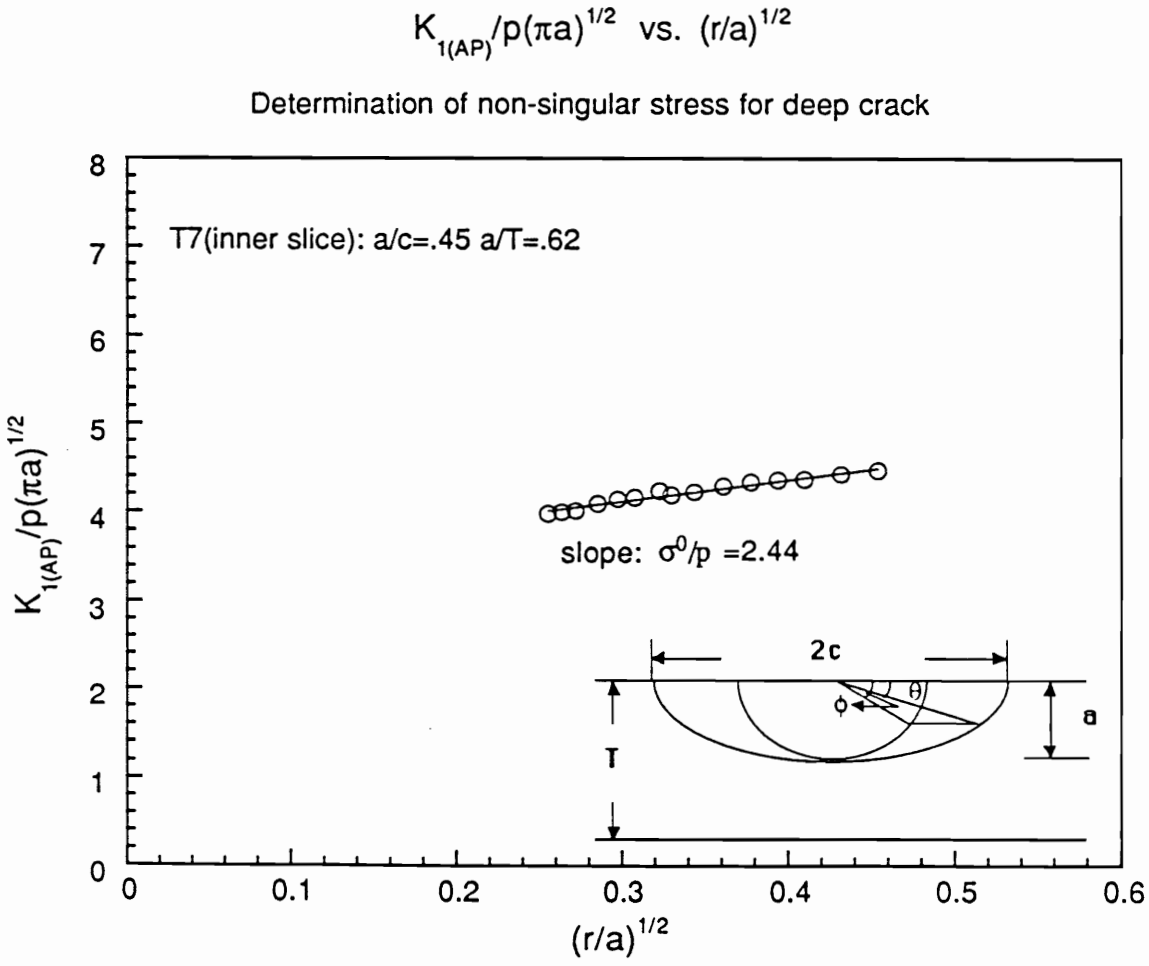

Figure 5.2. Determination of non-singular stress for deep crack

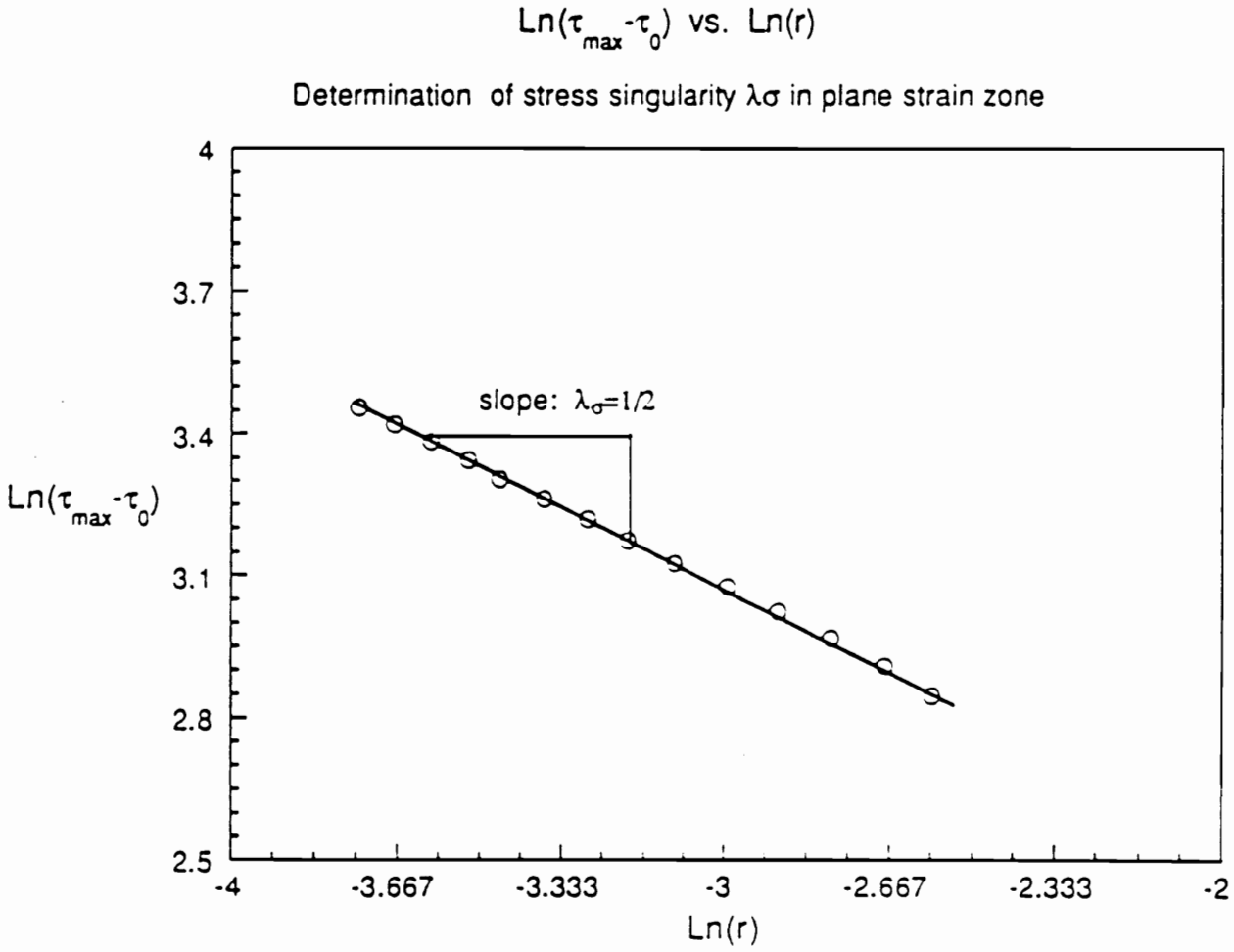

Figure 5.3. Determination stress singularity for medium crack in plane strain zone

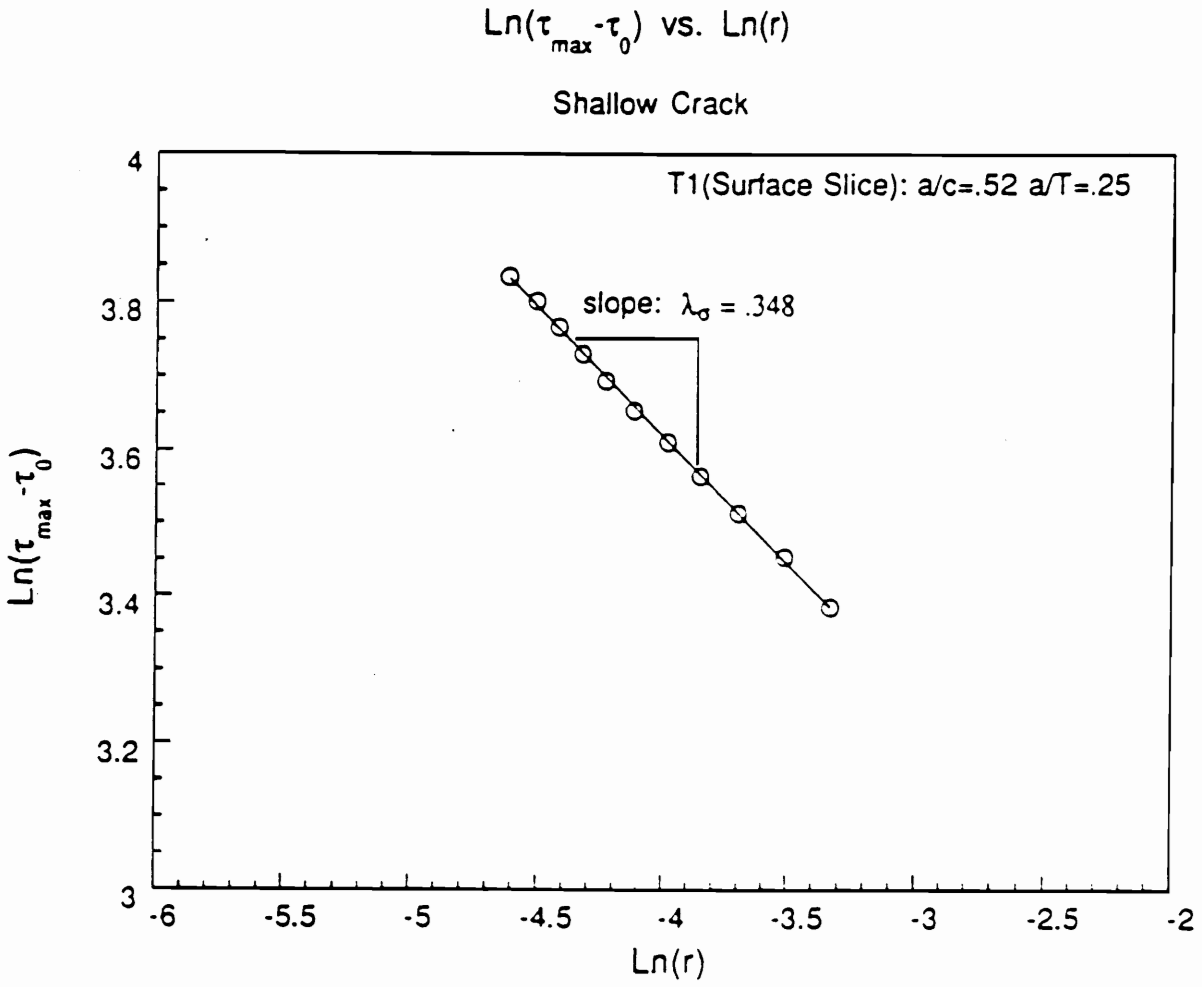

Figure 5.4. Determination stress singularity for shallow crack at inner star surface

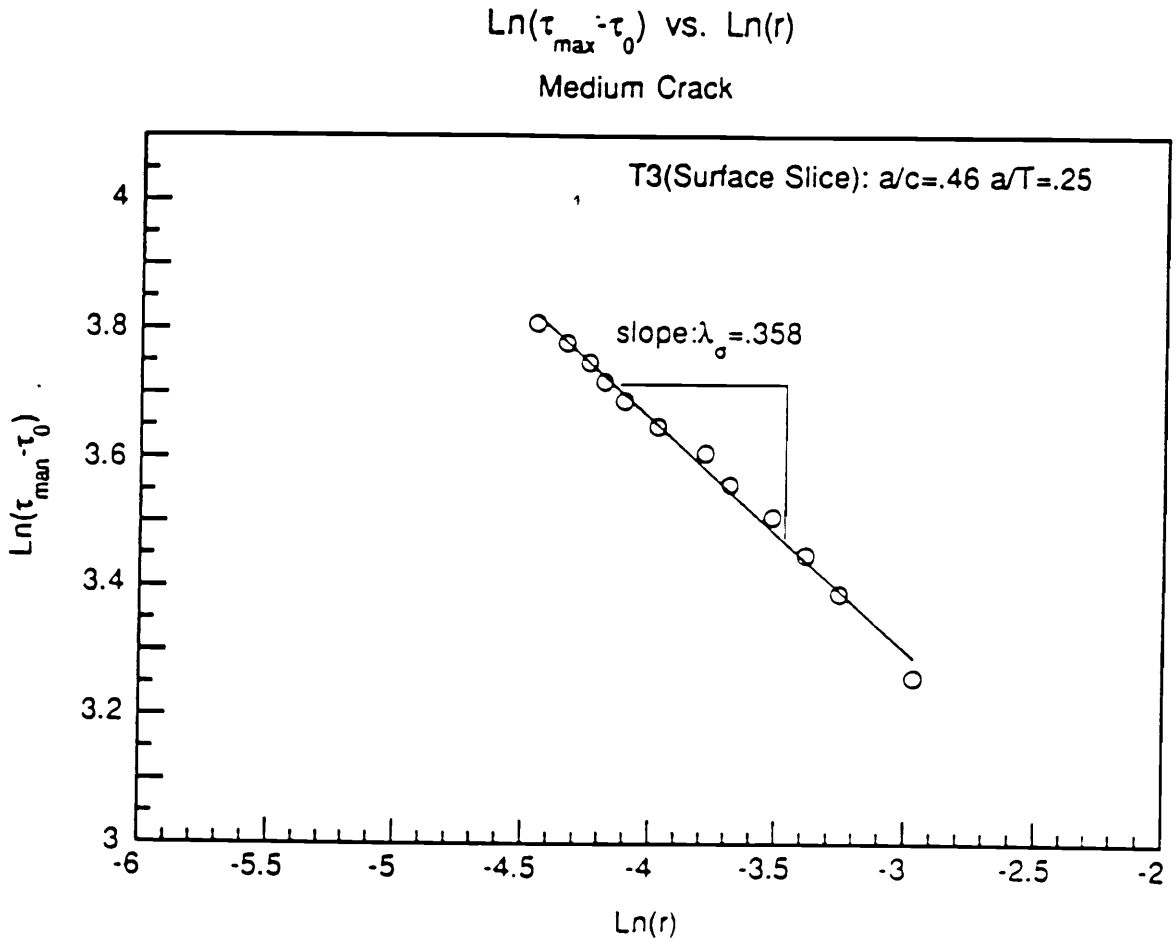

Figure 5.5. Determination stress singularity for medium crack at inner star surface

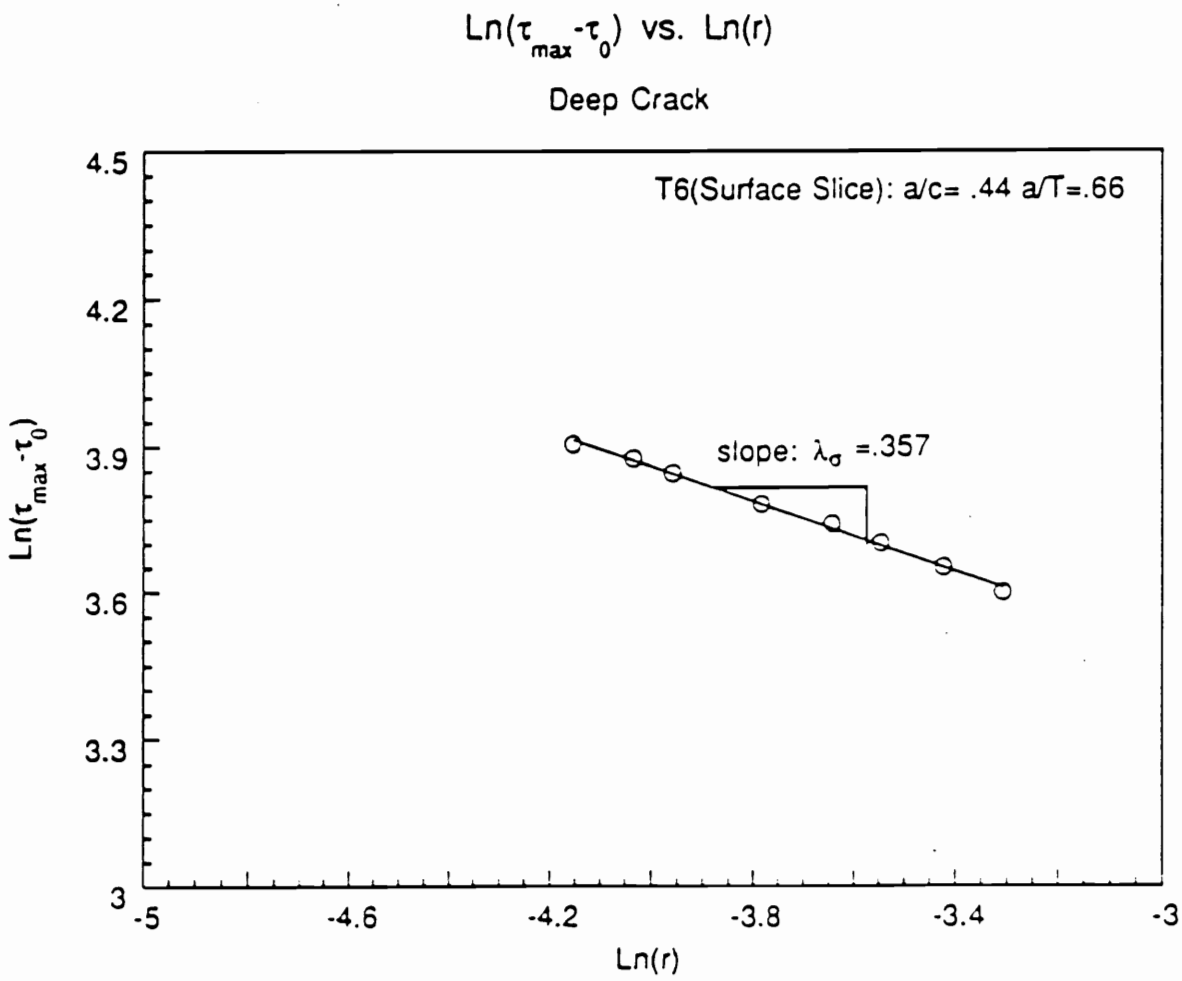

Figure 5.6. Determination stress singularity for deep crack at inner star surface

results which have been obtained from the four point bending tests. Fig.(5.7) shows that the results from the photoelastic surface slice using $\tau_0 = 0$ is in reasonable agreement with Benthem's results at the free surface. The moire results agree closely with Benthem's results at the free surface, too. Fig.(5.7) indicates that there is some difference between photoelastic and moire results. This difference is caused by the thickness of the slice for the photoelastic analysis. However, the difference is small enough to be considered acceptable. For the surface flaws in wide tension plates, Fig.(5.8) shows similar photoelastic results obtained from the crack border of surface flaws for different aspect ratios (a/c) under Mode I loading.

For the pressurized cylinder with star-shaped cutout experiments, the ratios of a/c are 0.52, 0.56, 0.54 and the ratios of a/T are 0.28, 0.25, 0.32 for the shallow cracks (T0, T1 and T2), respectively. The applied internal pressure for T1 and T2 is 6.9 psi (47.6 kPa) and for T0 3.9 psi (26.9 kPa). The stress singularity order for the shallow crack tests is given in Table 6. The table shows approximately that the linear zone in $\sqrt{(\frac{r}{a})}$ lies between 0.25 to 0.45 from the crack tip. Meanwhile, in the medium crack tests (T3, T4, and T5), both T3 and T5 have inner pressure p = 6.9 psi (47.6 kPa)and T4 has inner pressure p = 6.1 psi (42.1 kPa). The geometry of the medium surface flaws is: T3(a/c = 0.46, a/T = 0.45), T4(a/c = 0.52, a/T = 0.52), and T5(a/c = 0.43, a/T = 0.56), respectively. Table 7 presents the values of the stress singularity order along the crack border. Similarly, for the deep crack tests (T6 and T7) the internal pressure is p = 6.9 psi (47.6 kPa) in the star-shaped cutout cylinders; their a/c ratios are 0.44, 0.45, and a/T ratios are 0.66, 0.62. Table 8 shows the results of the deep crack tests. A summary of the stress singularity order for the inner surface slice and the comparison with Benthem's results are presented in Table 9. Thus, we may conclude that good experimental accuracy is obtained here. Since the photoelastic material epoxy PLM-9 has high Poisson's ratio ($\nu = 0.5$) at the critical temperature, the value

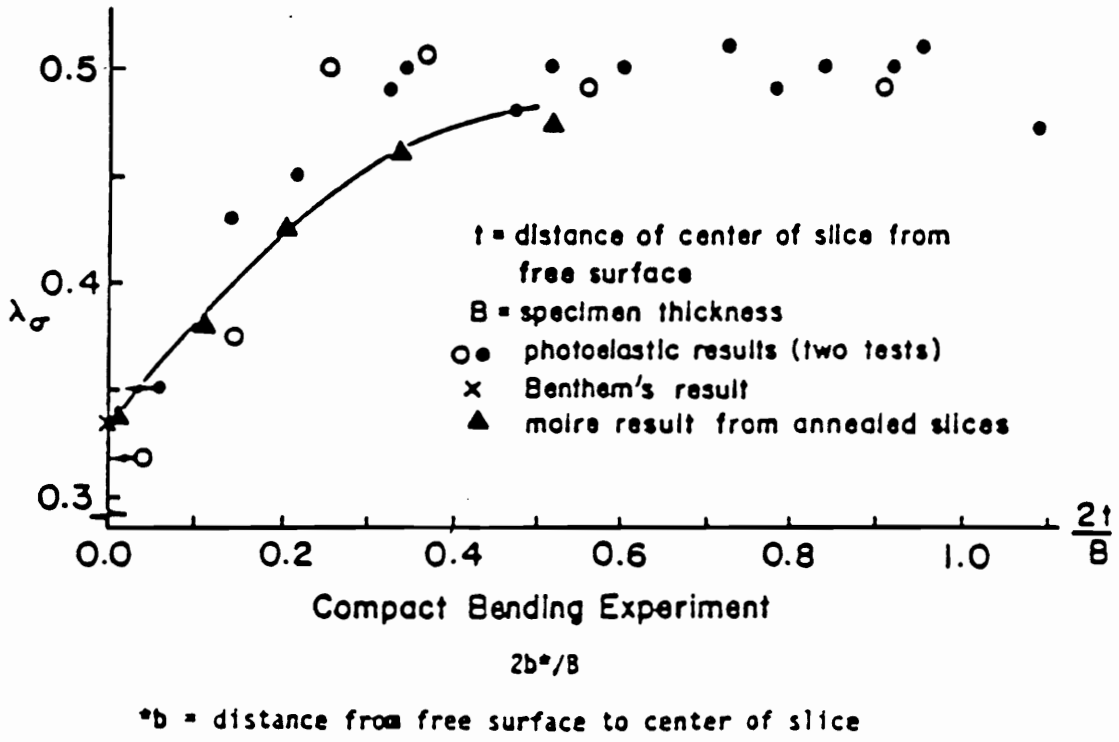

Figure 5.7. Distribution of stress singularity for four point bending specimen [38]

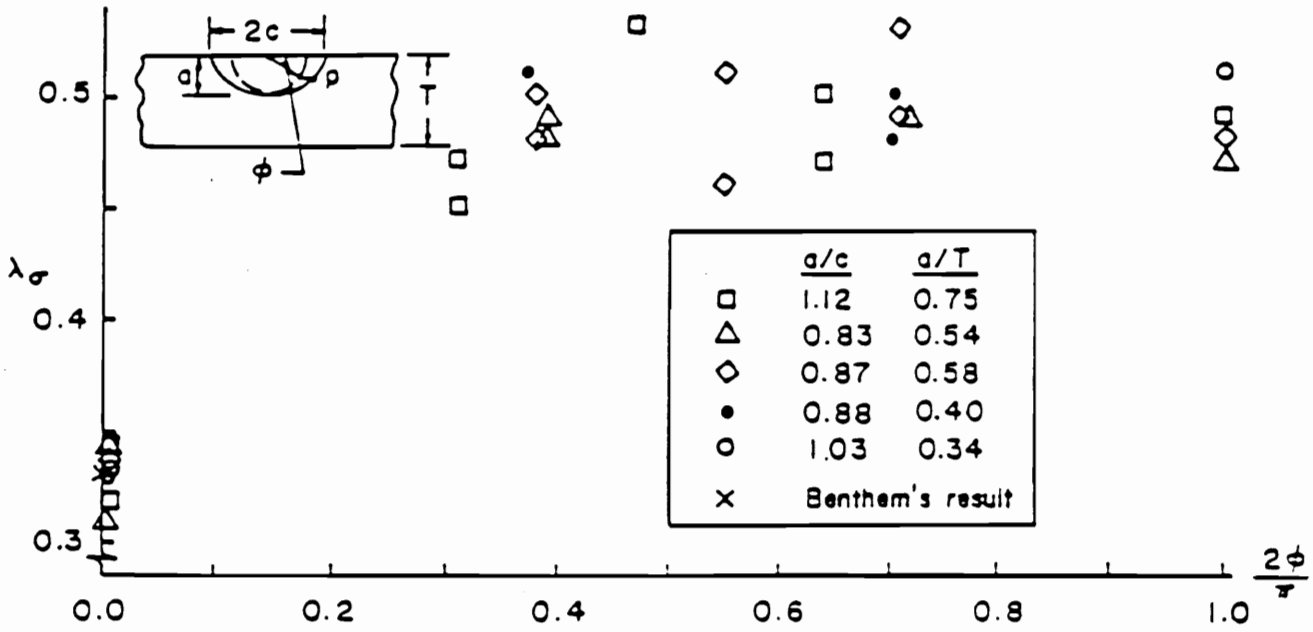

Figure 5.8. Distribution of stress singularity for surface flaw in wide tension plate [41]

of the stress singularity order at the inner star surface is expected to be significantly different from the classical value of 1/2.

As shown in the sequel, it shows from the following tables that the distributions of the singularity order are independent of the ratios a/c and a/T. To within experimental scatter, the values of the stress singularity are independent of the crack shapes and crack depths. Again one compares the pressurized star-shaped cutout cylinders' results with the results of the four point bending specimen and the surface flaws in the wide tension plate specimen. There are several differences between those tests, such as (1) loading conditions (2) specimen geometries (3) crack shapes. Both in the four point bending tests and the wide tension plate experiments, there is a free boundary at the surface. However, in the cylinder with star-shaped cutout tests, the interior pressure is applied on the inner star surface so that there is not a free inner star boundary in the rocket motor model tests. The above study suggests that the values of the stress singularity order are independent of the specimen geometries, loading conditions, crack shapes, and crack depths. The study also provides the value of the stress singularity order when the crack intersects the inner star surface at right angles under a pressurized condition. It agrees with Benthem's solution at the free surface.

In summary, one may use the optical method of "stress freezing photoelasticity" to measure near-tip three-dimensional effects in cracked bodies. This technique [42] was used to evaluate the loss in the LEFM inverse square root singularity in the neighborhood of the right angle crack border which includes free surface intersection for the four point bending specimens and the surface flaw in wide tension plate tests. The refined technique also proves that it can be applied to the complex geometry (rocket motor grain) for the surface measurement. As we can see, the above result

Table 6. The results of stress singularity for the shallow crack

Test #0	Data Zone $\sqrt{\frac{I}{2}}$	Data Zone (mm)	$\lambda_{\sigma(uncorrect)}$	$\lambda_{\sigma(correct)}$	τ_0
T0-0-1S	.26-.42	.25-.62	.35	.35	0
T0-30-1S	.25-.46	.20-.75	.33	.50	5.88
T0-60-1S	.26-.45	.25-.72	.53	.50	1.02
T0-90	.24-.42	.20-.65	.44	.50	2.15
T0-0-2S	.25-.45	.22-.72	.34	.34	0
T0-30-2S	.25-.46	.21-.76	.34	.50	1.62
T0-60-2S	.26-.49	.26-.86	.40	.50	2.23

Test #1	Data Zone $\sqrt{\frac{I}{2}}$	Data Zone (mm)	$\lambda_{\sigma(uncorrect)}$	$\lambda_{\sigma(correct)}$	τ_0
T1-0-1S	.25-.40	.22.-.52	.33	.33	0
T1-30-1S	.25-.47	.20-.78	.27	.50	16.53
T1-45-1S	.25-.46	.20-.68	.39	.50	6.48
T1-90	.25-.45	.20-.65	.43	.50	3.84
T1- 0-2S	.26-.47	.23-.70	.30	.36	0
T1-30-2S	.25-.46	.20-.67	.40	.50	5.97
T1-45-2S	.25-.46	.20-.70	.40	.50	5.86

Test #2	Data Zone $\sqrt{\frac{I}{2}}$	Data Zone (mm)	$\lambda_{\sigma(uncorrect)}$	$\lambda_{\sigma(correct)}$	τ_0
T2-0-1S	.25-.45	.33-.85	.32	.32	0
T2-30-1S	.25-.44	.25-.81	.47	.50	1.46
T2-60-1S	.25-.45	.25-.85	.35	.50	14.04
T2-90	.25-.45	.26-.86	.56	.50	3.39
T2- 0-2S	.25-.47	.25-.90	.35	.35	0
T2-30-2S	.25-.46	.25-.87	.46	.50	2.33
T2-60-2S	.25-.46	.25-.88	.40	.50	5.95

Table 7. The results of stress singularity for the medium crack

Test #3	Data Zone $\sqrt{\frac{r}{2}}$	Data Zone (mm)	$\lambda_{\sigma(\text{uncorrect})}$	$\lambda_{\sigma(\text{correct})}$	τ_0
T3-0-1S	.20-.40	.22-0.94	.38	.38	0
T3-15-1S	.25-.46	.36-1.21	.42	.500	4.57
T3-30-1S	.25-.45	.35-1.16	.44	.500	3.11
T3-45-1S	.25-.46	.37-1.19	.45	.500	2.38
T3-90	.25-.40	.37-0.95	.40	.500	9.20
T3-0-2S	.22-.47	.29-1.30	.35	.35	0
T3-15-2S	.25-.45	.35-1.17	.39	.500	5.62
T3-30-2S	.25-.46	.36-1.20	.43	.500	3.35
T3-45-2S	.25-.45	.36-1.24	.41	.500	4.33
T3-60-2S	.25-.46	.35-1.23	.40	.500	5.18

Test #4	Data Zone $\sqrt{\frac{r}{2}}$	Data Zone (mm)	$\lambda_{\sigma(\text{uncorrect})}$	$\lambda_{\sigma(\text{correct})}$	τ_0
T4-15-1S	.25-.46	.42-1.40	.45	.50	2.60
T4-30-1S	.25-.45	.41-1.34	.44	.50	3.07
T4-45-1S	.25-.46	.40-1.37	.32	.50	4.55
T4-60-1S	.25-.46	.41-1.43	.39	.50	5.36
T4-90	.25-.45	.43-1.36	.40	.50	4.83
T4-0-2S	.20-.40	.28-1.06	.36	.36	0
T4-15-2S	.25-.46	.41-1.43	.41	.50	4.95
T4-30-2S	.25-.45	.41-1.32	.41	.50	4.50
T4-45-2S	.25-.45	.41-1.31	.43	.50	3.24
T4-60-2S	.25-.45	.42-1.38	.43	.50	3.64

Test #5	Data Zone $\sqrt{\frac{r}{2}}$	Data Zone (mm)	$\lambda_{\sigma(\text{uncorrect})}$	$\lambda_{\sigma(\text{correct})}$	τ_0
T5-0-1S	.20-.39	.28-1.08	.35	.35	0
T5-7-1S	.25-.46	.43-1.5	.41	.50	4.95
T5-15-1S	.25-.46	.43-1.5	.41	.50	5.26
T5-30-1S	.25-.45	.45-1.53	.44	.50	3.67
T5-60-1S	.25-.46	.44-1.54	.40	.50	5.70
T5-90	.25-.45	.45-1.46	.43	.50	4.62
T5-7-1S	.25-.46	.45-1.52	.43	.50	4.67
T5-15-2S	.25-.46	.45-1.51	.43	50	3.97
T5-45-2S	.25-.46	.44-1.55	.34	50	13.3
T5-60-2S	.25-.46	.44-1.50	.31	50	16.0

Table 8. The results of stress singularity for the deep crack

Test #6	Data Zone $\sqrt{\frac{I}{a}}$	Data Zone (mm)	$\lambda_{\sigma(uncorrect)}$	$\lambda_{\sigma(correct)}$	τ_0
T6-0-1S	.25-.38	.39-.93	.36	.36	0
T6- 7-1S	.25-.45	.52-1.68	.41	.50	5.07
T6-15-1S	.25-.46	.52-1.76	.39	.50	6.16
T6-30-1S	.25-.46	.53-1.83	.43	.50	3.81
T6-45-1S	.25-.46	.53-1.81	.41	.50	4.80
T6-60-1S	.25-.45	.52-1.72	.40	.50	5.92
T6-90	.25-.45	.54-1.76	.43	.50	3.22
T6- 7-2S	.20-.45	.53-1.68	.40	.36	5.90
T6-15-2S	.25-.45	.53-1.77	.39	.50	5.11
T6-30-2S	.25-.46	.51-1.84	.36	.50	7.24
T6-45-2S	.25-.46	.52-1.77	.40	.50	5.59
T6-60-2S	.25-.45	.51-1.73	.40	.50	5.83

Test #7	Data Zone $\sqrt{\frac{I}{a}}$	Data Zone (mm)	$\lambda_{\sigma(uncorrect)}$	$\lambda_{\sigma(correct)}$	τ_0
T7-30-1S	.25-.45	.51-1.62	.40	.50	5.97
T4-45-1S	.25-.37	.48-1.13	..41	.50	7.46
T4-60-1S	.25-.38	.53-1.58	.38	.50	7.41
T4-90	.25-.45	.49-1.55	.25	.50	23.78
T7-0-2S	.20-.44	.52-1.55	.35	.35	0
T7-30-2S	.25-.44	..50-1.55	.40	.50	7.08
T7-45-2S	.25-.45	.49-1.58	.40	.50	7.08
T7-60-2S	.25-.41	.50-1.35	.40	.50	7.60

Table 9. Comparison of Benthem's result and Experimental results

Cracks Group	Test#	a/c	a/T	λ_σ(Exp.)	Avg.
Shallow	T0	.54	.28	.35	
Shallow	T1	.52	.25	.33	
Shallow	T2	.55	.32	.33	.34
Medium	T3	.46	.45	.36	
Medium	T4	.52	.52	.36	
Medium	T5	.43	.56	.36	.36
Deep	T6	.44	.66	.36	
Deep	T7	.45	.62	.33	.34
Benthem's Result					.33

makes it possible to measure the surface effect near the crack tip in rocket motor grain. This means that the SIF determined from LEFM at the intersection of the crack border with the inner surface is to some extent a fictitious value.

5.3 Results of the Stress Intensity Factors for Photoelastic Tests

The procedures in chapter 4 to determine the two-dimensional stress intensity factor (S.I.F) K_I are reviewed briefly. The stress intensity factor K_I is basically given by Eq.(4.8). Eq.(4.8) shows that the normalized apparent S.I.F ($\frac{(K_I)_{AP}}{p(\pi a)^{1/2}}$) varies linearly with the square root of the normalized distance from the crack tip $(\frac{r}{a})^{1/2}$ where r is measured along $\theta = \frac{\pi}{2}$. Then, one plots a set of raw photoelastic data $\frac{(K_I)_{AP}}{p(\pi a)^{1/2}}$ versus $(\frac{r}{a})^{1/2}$. Using a least squares fit, one can locate the linear zone and extrapolate it across a very near-field non-linear zone to the crack tip in order to obtain the normalized K_I ($\frac{K_I}{p(\pi a)^{1/2}}$). In all the tests conducted here, for the shallow cracks, the medium cracks, and the deep cracks, this linear range of the data occurs for the value of $\sqrt{\frac{r}{a}}$ between 0.25 and 0.45. This means that the common linear range for all slices is approximately in the region located between $\sqrt{\frac{r}{a}} = 0.25$ to 0.45. For the same crack, all slices should have approximately the same linear zone. Typical photoelastic data for estimating the stress intensity factor are presented in Fig.(5.9). It shows only the data obtained in the linear zone on a plot of normalized apparent S.I.F versus the square root of the normalized distance from the crack tip. The observations of the center slice and surface slice from a multiplication unit showing the near tip fringe patterns are given in Fig.(5.10). Due to the symmetry of the crack border, all slices have been cut from both sides of the center of each flaw. The values of S.I.F have been averaged for equal distance from the center point of the crack border.

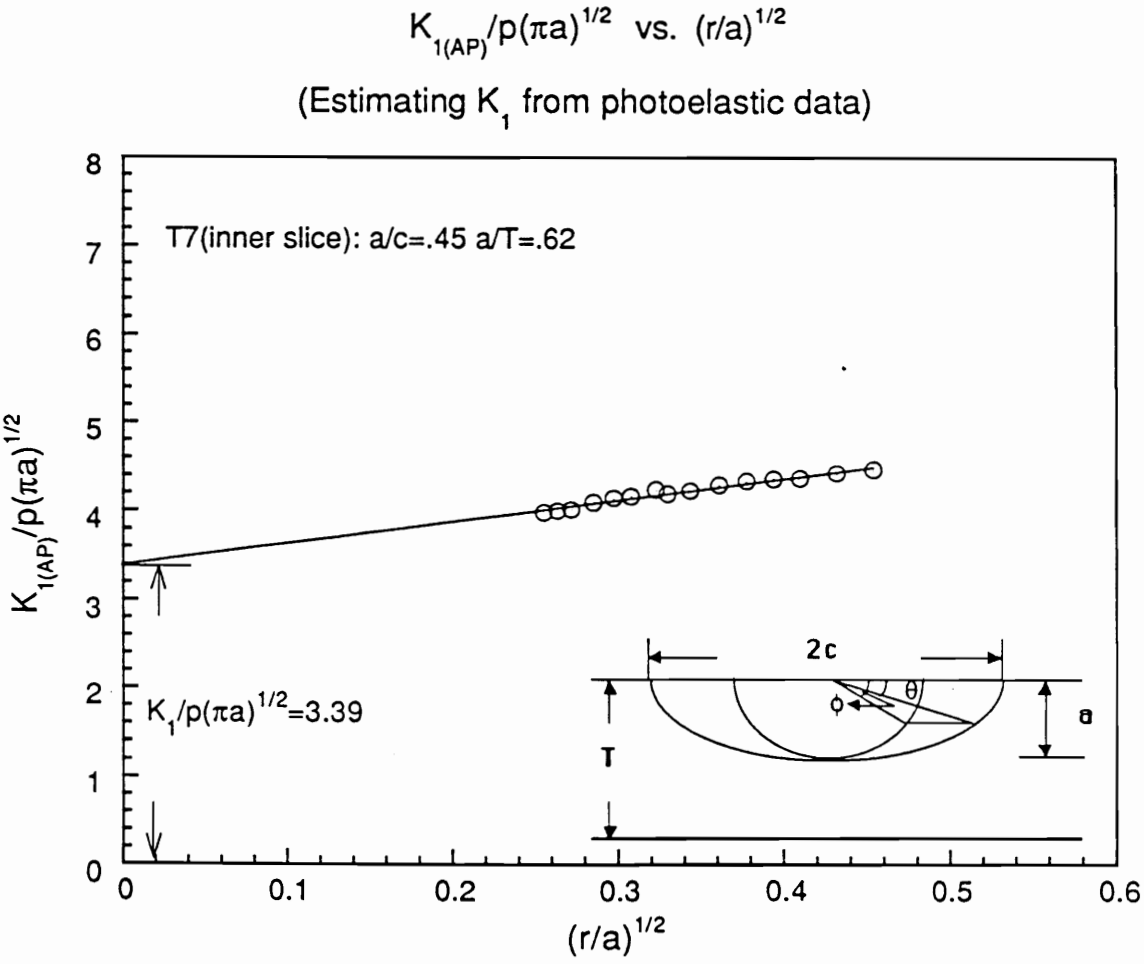

Figure 5.9. Typical data for estimating S.I.F

(a)

(b)

Figure 5.10. Fringe patterns for center (a) and surface (b) slice normal to crack plane (Mode I)

For the shallow crack tests (a/T = 0.25, 0.28, 0.32), the results are given in Table 10. The average of the results in Table 10 shows that the difference between the three shallow crack tests amounts to ±12% for both the center slice and the surface slice. The distributions of the normalized stress intensity factors times the complete elliptical integral of the second kind of correction factor (Φ) along the crack border are presented in Fig.(5.11). Figure(5.11), for the shallow crack tests (a/T < 0.40) shows that the distributions of $\frac{K_I}{p(\pi a)^{1/2}}\Phi$ around the crack front maintain an approximately upward trend from the inner surface to the maximum crack depth. Table 11 contains the results of the S.I.F for the medium crack tests (a/T = 0.43, 0.46, 0.52). Fig.(5.12) shows the distributions of the normalized S.I.F with the correction factor Φ for the medium crack. Obviously, these results suggest that as the crack grows deeper, a more uniform S.I.F distribution results around the flaw border. The results show an experimental scatter of about ±3% at the inner star surface and ±6% at the center. For the deep crack tests (a/T = 0.62, 0.66), Table 12 shows the results of the two tests. Similarly, as is clear from Fig.(5.13), the distributions of the SIF gives a fairly uniform profile along the flaw border with a scatter of about ±5.5% at the inner surface and ±1.1% at the center.

A comparison of the results from the test specimens for different ranges of a/T shows that there is more experimental scatter for the shallow cracks than the medium and the deep cracks. One of the reasons for this kind of influence is the local defects on the border of the shallow cracks. When the initial crack has been made, some irregularities have occurred on the crack front. In spite of the crack growth for a short distance, the branching cracks still have reached the crack border. The picture of the shallow crack profiles, Fig.(5.14), indicates the location of the defects.

The photoelastic slice data do not reveal any significant effects on the SIF distribution near the inner star surface. This implies that the 3D surface effect is washed

out over the thickness of the surface slice (approximately 0.5mm). However, by adjusting the variable λ_σ photoelastic algorithm to yield the same result as given by moire at the free surface (τ_0), the value of λ_σ can be accurately estimated from the photoelastic data. Therefore, this refined technique of "frozen stress photoelasticity" is again verified as appropriate to measure the three-dimensional state of the stress field in cracked bodies even in the more complicated geometry. The above figures suggest that due to the uniform distribution of the S.I.F a two-dimensional model may be used for the shallow, the medium and the deep surface flaws.

The other observation is that as the values of a/T increase the S.I.F, K_I, tends to increase in value. The result is shown in Fig.(5.15). Since the K_I is unnormalized with respect to the crack depth (a), the increasing trend can be assessed with increasing crack depth. Again Fig.(5.16) shows the plot for $\frac{K_I}{p(\pi a)^{1/2}}$ versus a/c. The plot indicates that the values of a/c increase as the values of $\frac{K_I}{p(\pi a)^{1/2}}$ increase. Since the crack depth a is normalized out of the quantity $\frac{K_I}{p(\pi a)^{1/2}}$, and T is constant, the trend of increasing can be attributed directly to a crack shape effect associated with decreasing crack length (c).

5.4 Two Dimensional Analysis - A Weight Function Approach

The weight function concept comes from work done by Bueckner [61] for edge cracked strips. Rice [62] showed that the stress intensity factor and the displacement field for a given flaw geometry and loading enables the construction of a weight function which depends only on geometry. Hence, with this weight function, the stress in-

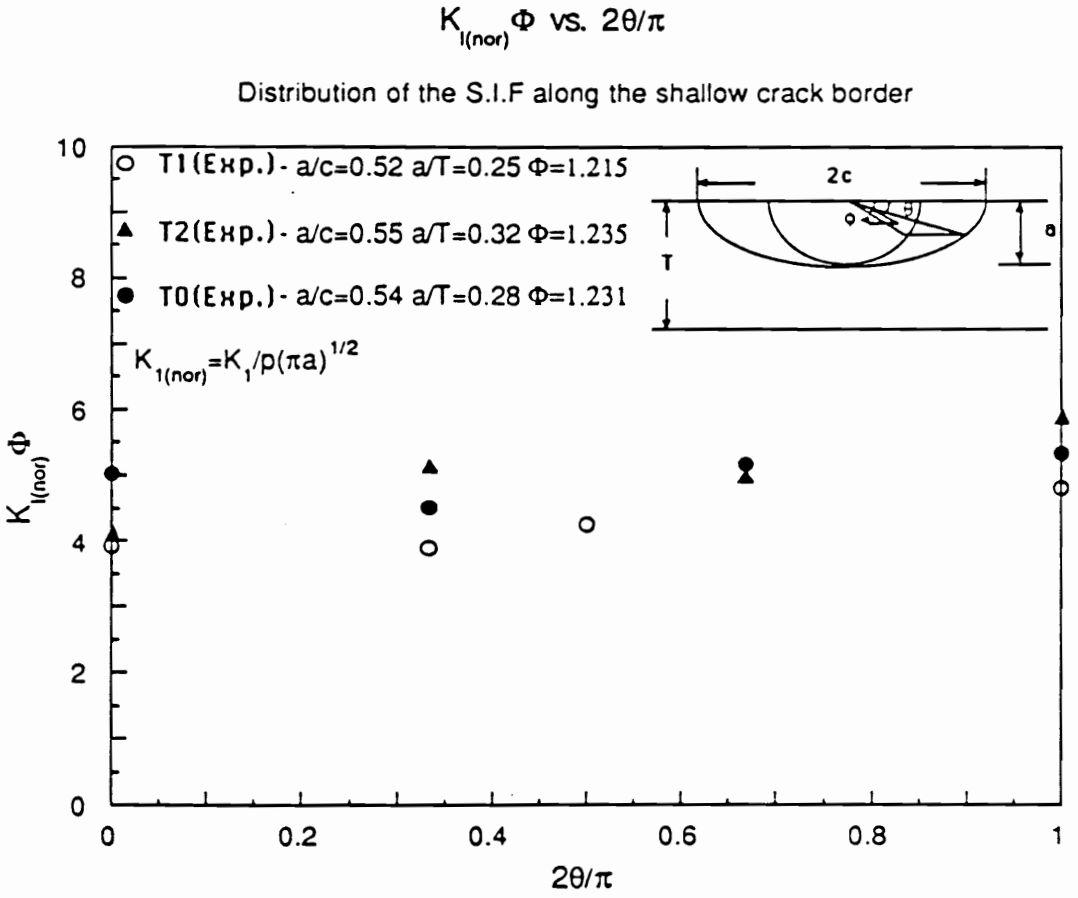

Figure 5.11. Distributions of S.I.F for shallow cracks

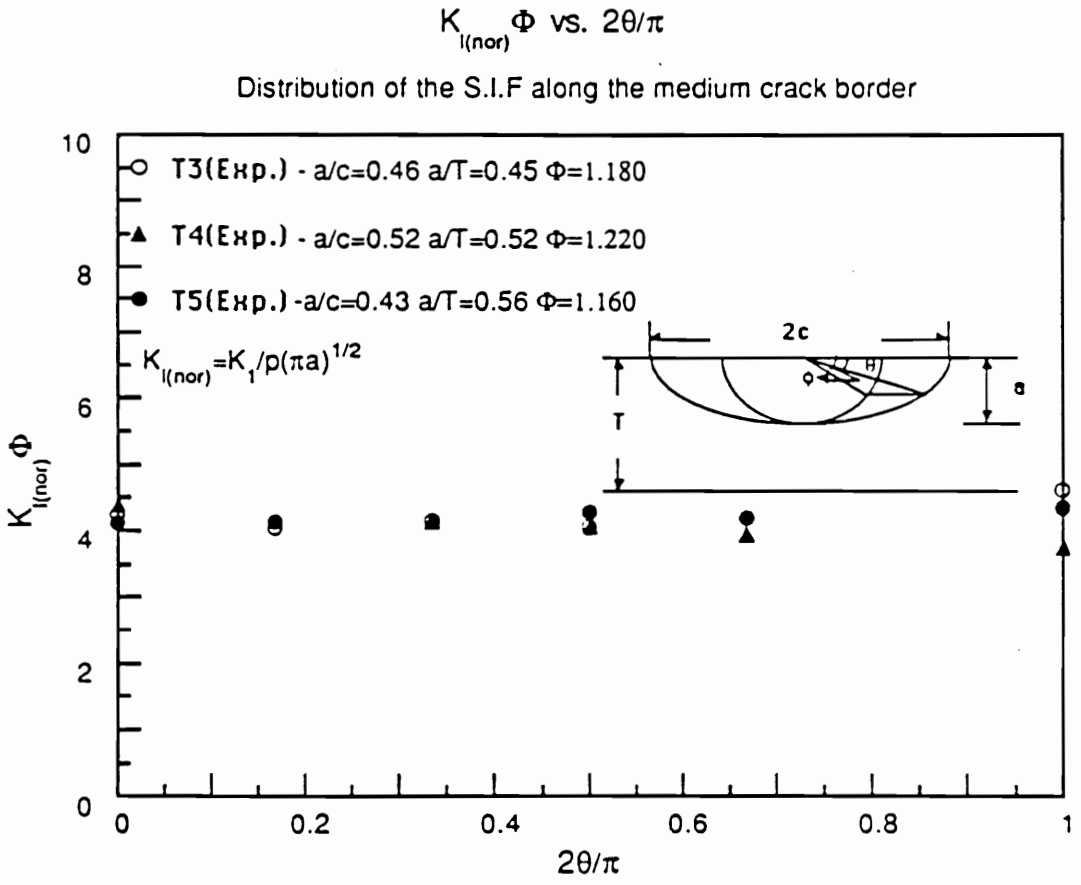

Figure 5.12. Distributions of S.I.F for medium cracks

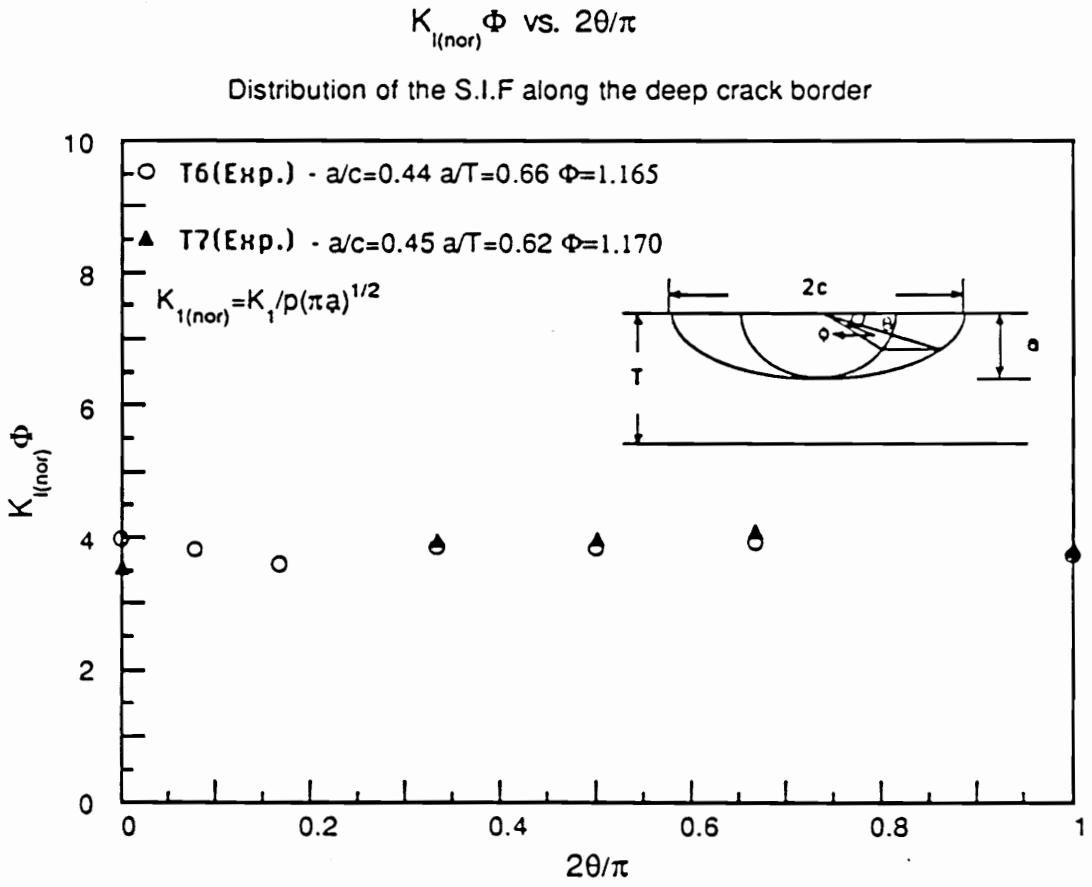

Figure 5.13. Distributions of S.I.F for deep cracks

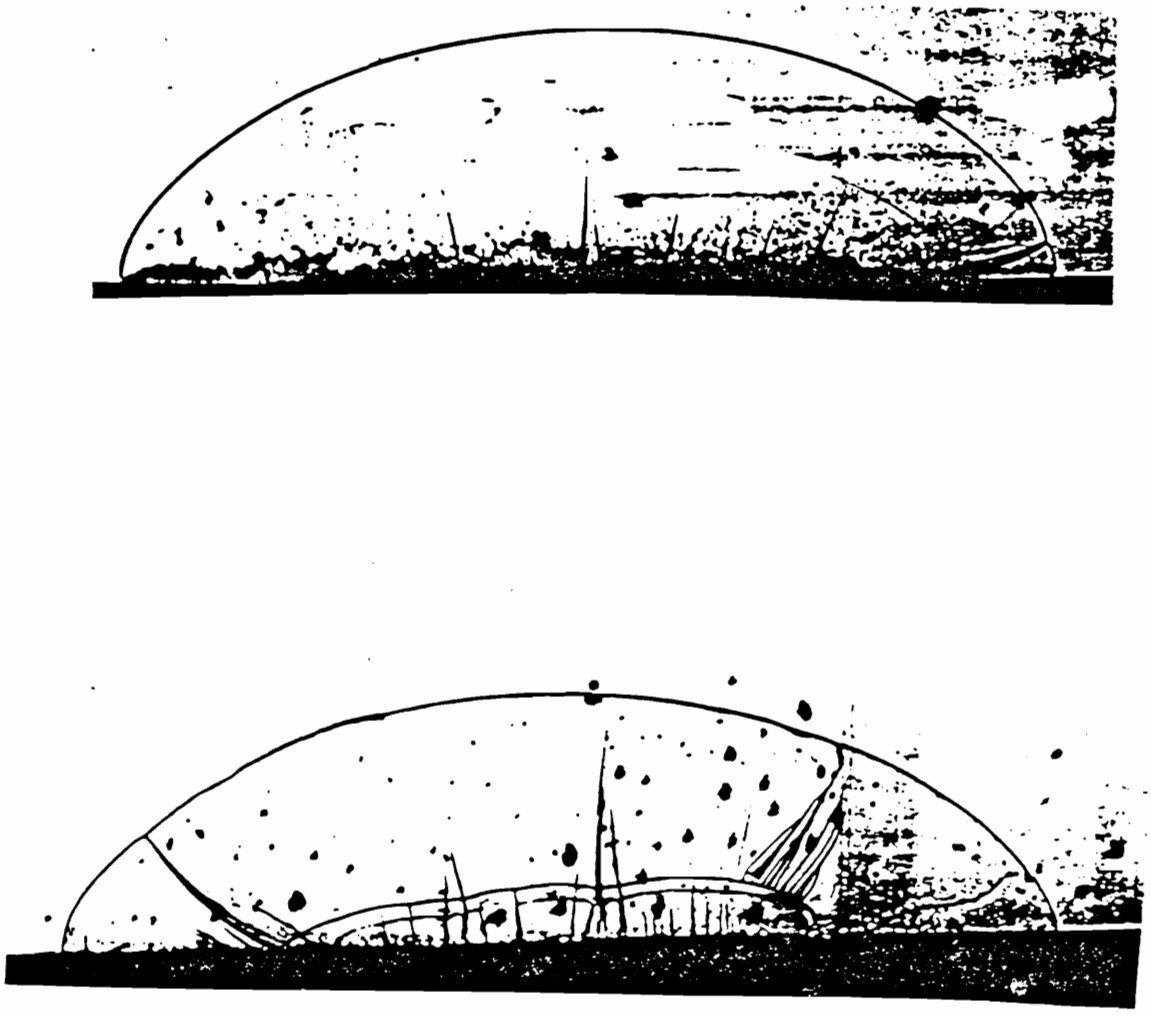

Figure 5.14. Shallow crack profiles

Table 10. The results of S.I.F along the crack border for the shallow crack

T0	K_1	$K_{1(nor)}$	$K_{1(nor)}\Phi$
T0-0	13.10	4.08	5.03
T0-30	11.75	3.66	4.51
T0-60	13.46	4.20	5.17
T0-90	13.94	4.35	5.35
Average	13.06	4.07	5.02

a/c=.54 a/T=.28 a=3.6mm c=6.67mm p=26.9kPa Φ=1.231

T1	K_1	$K_{1(nor)}$	$K_{1(nor)}\Phi$
T1-0	14.03	3.23	3.92
T1-30	13.92	3.21	3.90
T1-45	15.72	3.62	4.40
T1-90	17.21	3.96	4.82
Average	15.22	3.51	**4.26**

a/c=.52 a/T=.25 a=3.2mm c=6.15mm p=47.6kPa Φ=1.215

T2	K_1	$K_{1(nor)}$	$K_{1(nor)}\Phi$
T2-0	16.49	3.36	4.15
T2-30	20.49	4.17	5.15
T2-60	19.89	4.05	5.00
T2-90	23.81	4.85	5.99
Average	20.17	4.10	5.07

a/c=.55 a/T=.32 a=4.10mm c=7.42mm p=47.6kPa Φ=1.235

$$\Phi=\int_0^{\frac{\pi}{2}}[(\frac{a}{c})^2\sin^2\phi+\cos^2\phi]^{\frac{1}{2}}d\phi$$

Table 11. The results of S.I.F along the crack border for the medium crack

T3	K_1	$K_{1(nor)}$	$K_{1(nor)}\Phi$
T3-0	20.35	3.59	4.24
T3-15	19.71	3.48	4.11
T3-30	19.97	3.52	4.15
T1-45	19.53	3.45	4.07
T3-90	22.35	3.94	4.62
Average	20.38	3.60	4.14

a/c=.46 a/T=.45 a=6.19mm c=12.39mm p=47.6kPa Φ=1.180

T4	K_1	$K_{1(nor)}$	$K_{1(nor)}\Phi$
T4-0	20.83	3.60	4.39
T4-30	19.70	3.40	4.15
T4-45	19.32	3.34	4.08
T4-60	18.76	3.25	3.96
Average	19.65	3.39	4.14

a/c=.52a/T=.52 a=6.60mm c=12.7mm p=42.1kPa Φ=1.220

T5	K_1	$K_{1(nor)}$	$K_{1(nor)}\Phi$
T5-0	23.04	3.55	4.12
T5-15	23.18	3.57	4.14
T5-45	24.00	3.70	4.29
T5-60	23.53	3.63	4.20
T5-90	24.40	3.76	4.36
Average	23.63	3.64	4.22

a/c=.43 a/T=.56 a=7.34mm c=13.21mm p=47.6kPa Φ=1.160

$$\Phi=\int_0^{\frac{\pi}{2}}[(\frac{a}{c})^2\sin^2\phi+\cos^2\phi]^{\frac{1}{2}}d\phi$$

Table 12. The results of S.I.F along the crack border for the deep crack

T6	K_1	$K_{1(nor)}$	$K_{1(nor)}\Phi$
T6-0	24.02	3.42	3.98
T6-7	23.11	3.29	3.83
T6-15	21.72	3.09	3.60
T6-30	23.32	3.32	3.86
T6-45	23.22	3.31	3.85
T6-60	23.70	3.37	3.92
Average	23.18	3.30	3.84

a/c=.44 a/T=.66 a=8.41mm c=19.05mm p=47.6kPa Φ=1.165

T7	K_1	$K_{1(nor)}$	$K_{1(nor)}\Phi$
T7-0	20.73	3.04	3.56
T7-30	23.11	3.39	3.97
T7-45	23.25	3.41	3.99
T7-60	23.89	3.50	4.10
T7-90	22.30	3.27	3.83
Average	22.66	3.32	3.89

a/c=.45 a/T=.62 a=7.90mm c=17.53mm p=47.6kPa Φ=1.170

$$\Phi=\int_0^{\frac{\pi}{2}}[(\frac{a}{c})^2\sin^2\phi+\cos^2\phi]^{\frac{1}{2}}d\phi$$

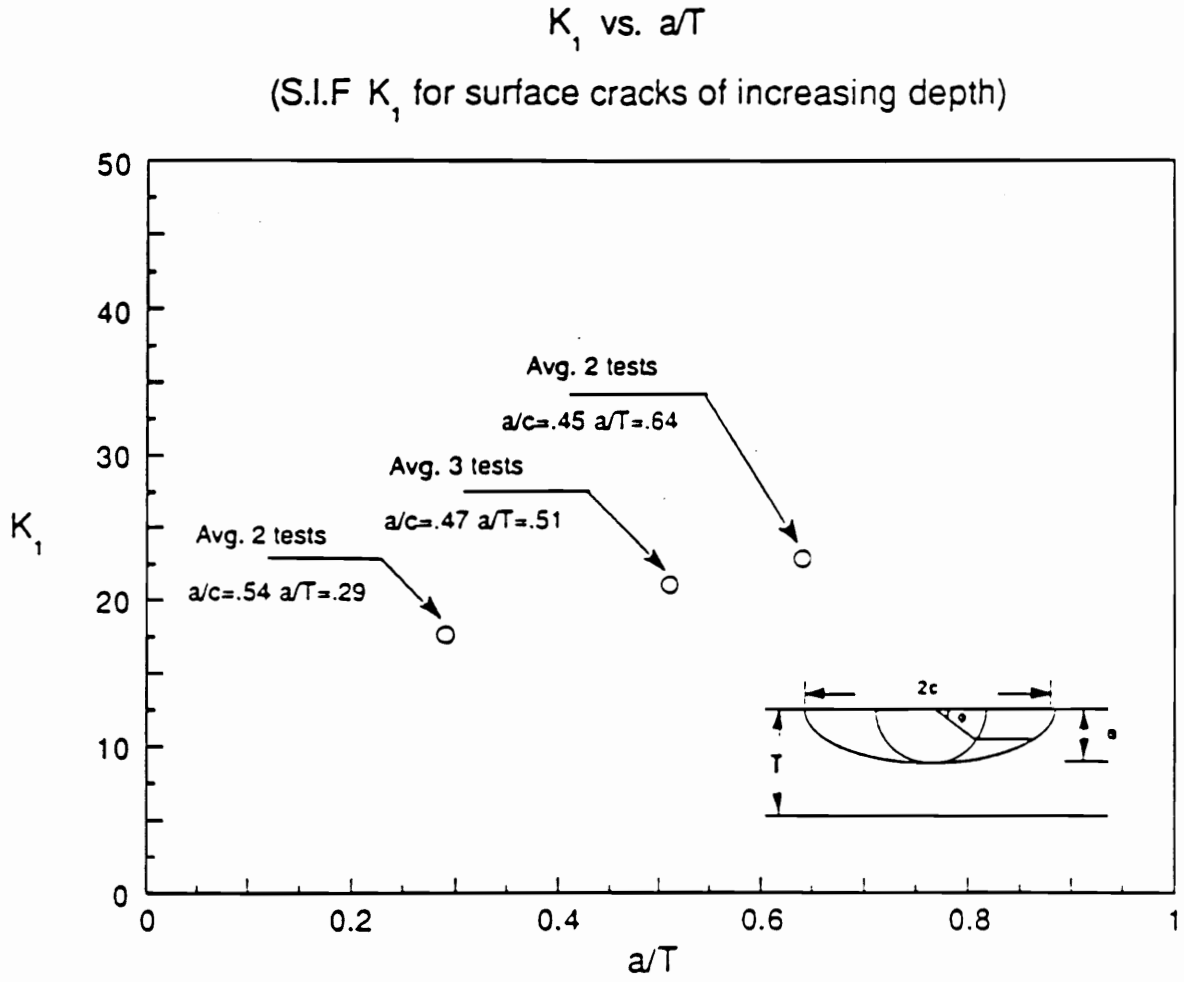

Figure 5.15. Stress intensity factor for surface cracks of increasing depth

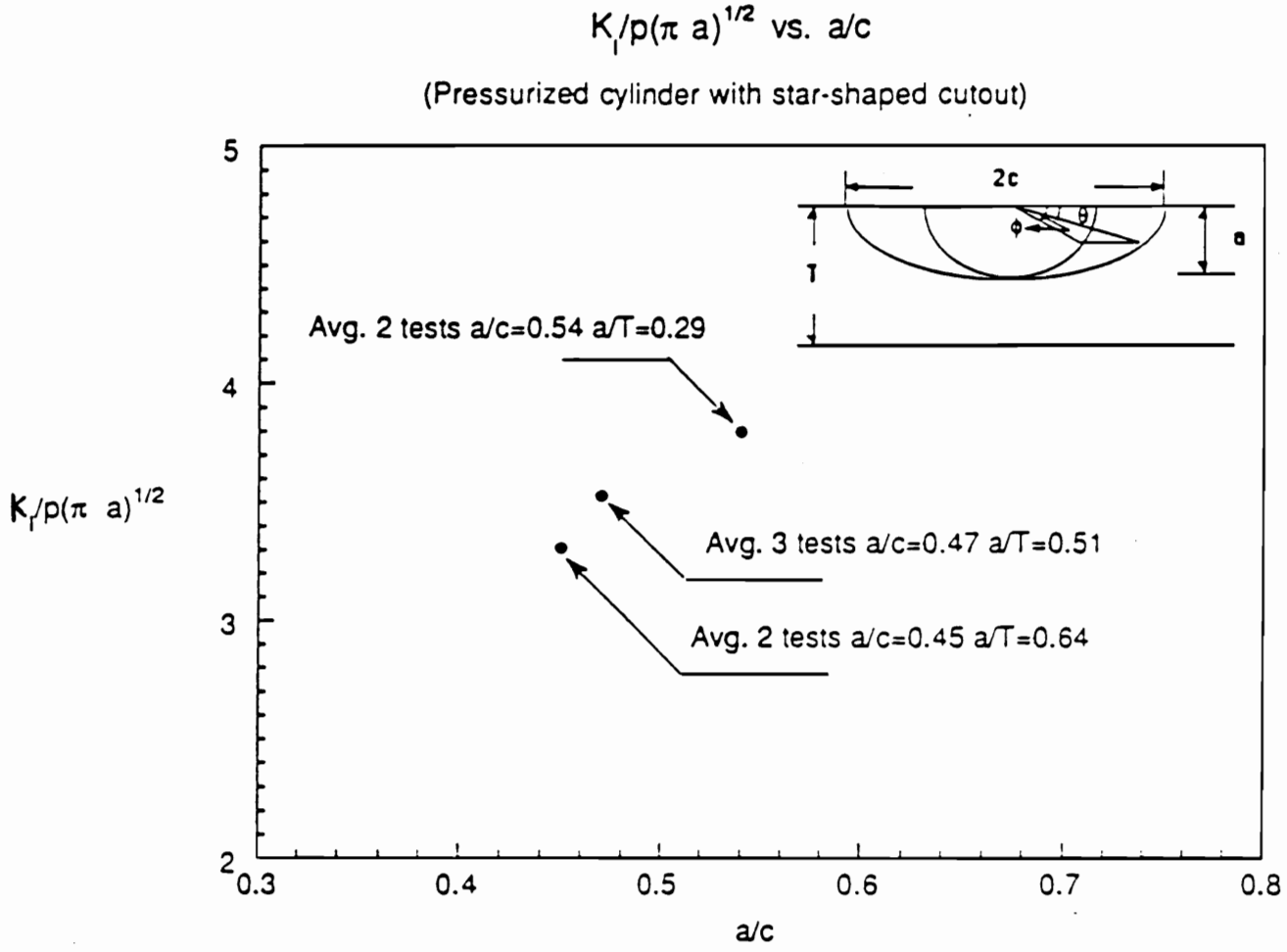

Figure 5.16. Normalized stress intensity factor for surface cracks of decreasing length

tensity factor K_I for any other symmetric loading applied to the same geometry can be obtained.

The experimental results suggest that the stress intensity factor is approximately constant around the crack front. To take advantage of these results, a weight function approach computes a two-dimensional stress intensity factor K_I using the stress distribution in the uncracked motor grain model from the Bowie [63] radial crack in a circular ring solution.

After the test was run, a ring was cut out of the photoelastic motor grain model at a distance half way between the end cap and the central crack. The ring has a thickness of 12.7 mm (0.5 in). The ring was placed in a polariscope and a picture of a dark field of isochromatic fringes was taken Fig.(3.11). Then, a stress separation by the "Rapid Method" [64] was applied to separate the principal stresses σ_1 and σ_2 Fig.(5.17) from the photograph. The crack surface loading p(x) Fig.(5.18) as the unflawed hoop stress occurring along a radial line coinciding with the desired path of crack propagation can be determined.

The reference problem used to construct the weight function consists of a radially cracked ring under internal pressure applied along the crack axis, which was solved by Bowie [63] using a modified mapping collocation technique. Taking Bowie's solution, a weight function was constructed to solve for the crack face loading p(x) shown in the Fig.(5.19). The stress intensity factor for a crack of length " a " subjected to the p(x) loading was found to be given by

$$K_I = \frac{H}{K_B} \int_0^a p(x) \frac{\partial \eta}{\partial a} dx \tag{5.1}$$

where

H - the constant $\frac{E}{1-\nu^2}$ for plane strain, and E is elastic modulus, ν is Poisson's ratio.

K_B - Bowie's stress intensity factor solution for a radial crack in a circular ring under internal pressure.

p(x) - the pressure loading perpendicular to the crack surface from the uncracked star shaped cutout.

η - the crack displacements along the crack length for a radial crack in a circular ring under internal pressure.

The crack displacement field was approximated with a conic section given by Grandt [64]-[66] for fitting radially cracked rings. When the crack surface loading is defined as the unflawed hoop stress occurring along a radial line coinciding with the desired path of crack propagation in star shaped cutout, stress intensity factor calculations are readily obtained from Eq.(5.1) by the linear superposition method.

Since there are not three dimensional analytical solutions of the stress intensity factor for cracked star shaped cutout, one may recommend a weight function approach for simplified stress analysis. That means the problem of the cracked star shaped cutout may be converted into the problem of the radially cracked circular ring in order to predict the stress intensity factor K_I.

Experimental results for cracked star shaped cutout under internal pressure agrees closely with a weight function method's analytical results (see Table 13 for comparison). Although the present method does not compute "K_I" directly from the star shaped cutout, reasonable K_I estimates for the cracked motor grain model should be possible from a weight function approach.

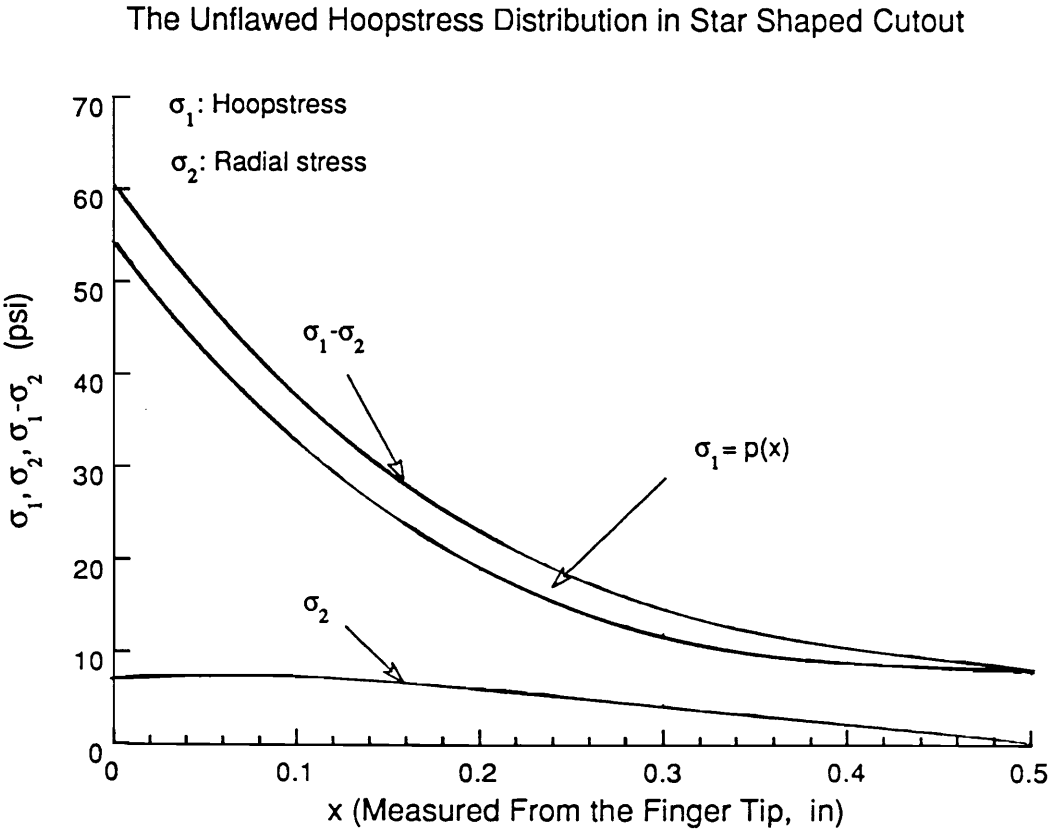

Figure 5.17. The unflawed hoopstress distribution in star shaped cutout

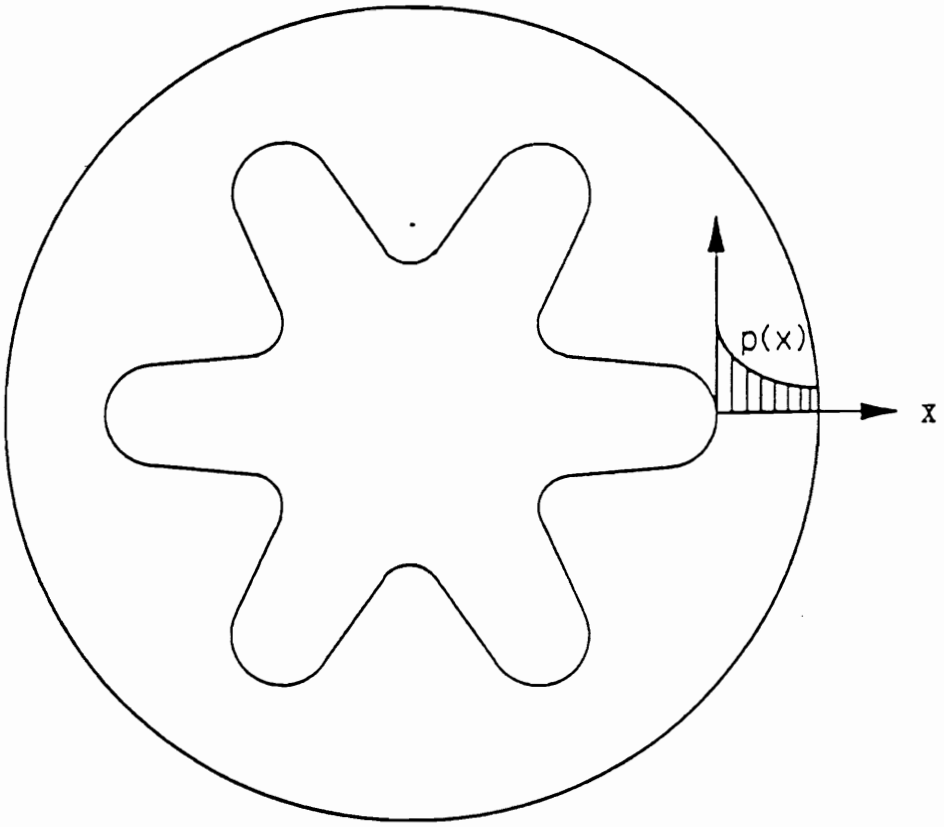

Figure 5.18. The crack surface loading p(x) in star shaped cutout

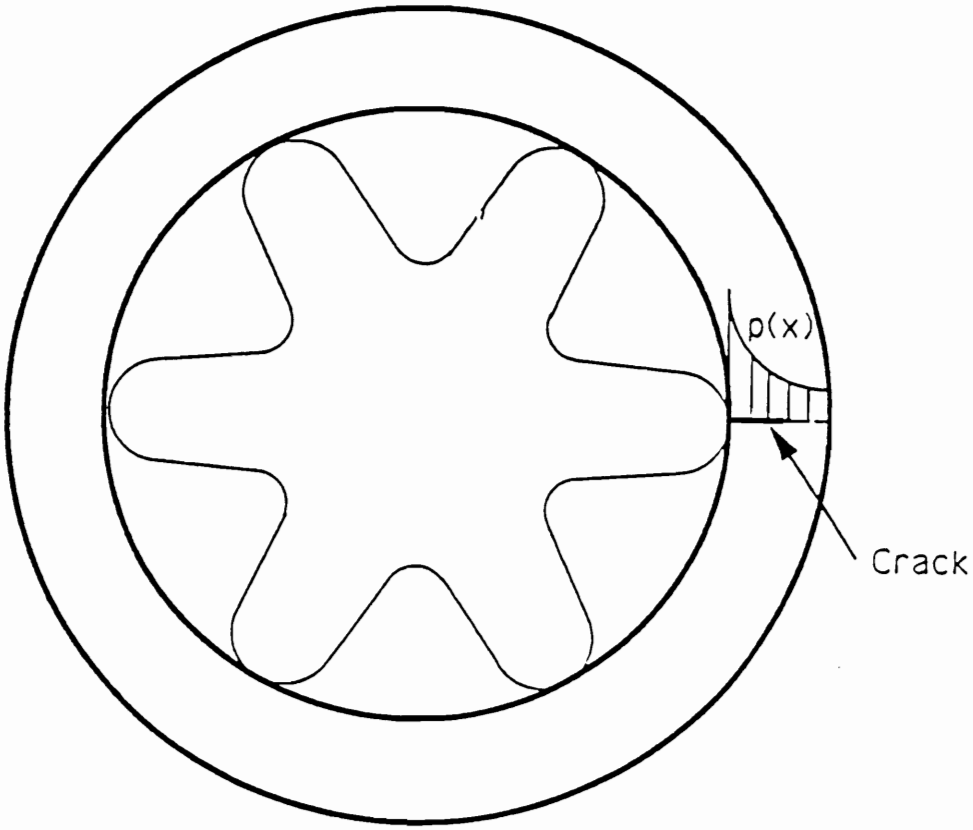

Figure 5.19. Loading of flawed ring

Table 13. Comparison experimental results with weight function approach results

	Experimental Results for Star Shaped Cutout $psi\sqrt{in}$ ($kPa\sqrt{m\ m}$)	A Weight Function Approach for Radial Crack in a Circular Ring $psi\sqrt{in}$ ($kPa\sqrt{m\ m}$)	Error %
Shallow Crack	17.69 (614.20)	17.89 (621.14)	1.1
Moderate Crack	21.10 (732.59)	21.62 (750.65)	2.4
Deep Crack	22.88 (794.39)	23.07 (800.99)	1.0

5.5 Three Dimensional Analysis - Equivalent Radius for Cylinder with Star-shaped Cutout

Since there is neither an analytical nor a numerical three-dimensional solution of the same geometry problem available to correlate the experimental results, one can consider use of Newman and Raju's [31] approximate numerical solution for an internal surface crack in a pressurized circular cylinder to compare the distributions of the SIF along the crack border with the experimental results. Newman and Raju use a three-dimensional finite element method to find the stress intensity factors along the semi-elliptical crack border. In Newman and Raju's solution, the ratio of crack depth to crack length (a/c) is from 0.2 to 1.0; the ratio of crack depth to wall-thickness (a/T) ranges from 0.2 to 0.8; and the ratio of wall thickness to vessel radius (t/R) is 0.1-0.25. They evaluate the stress intensity factor from the Mode I stress intensity factor influence coefficients for a wide range of semi-elliptical internal surface cracks in cylinders. The Newman and Raju coefficients were computed for the present experiments.

In order to convert the Newman and Raju solution to the cylinders with star-shaped cutouts, an equivalent inner radius is found for the star-shaped cutout cylinders. First one can use a quadratic interpolation method to adapt the test geometries and calculate the influence coefficients. Then, by keeping the crack depth the same as that of the cracked specimens, the equivalent radius is adjusted to compare the experimental results with the numerical solutions until their results are approached closely. A comparison between the experimental results and the approximate Newman and Raju solution is presented in Fig.(5.20)-Fig(5.22). As can be seen from Fig.(5.20), one can find the numerical solution at an equivalent radius R = 1.62 in (41.1mm) and R = 1.48 in (37.6mm) to match the center slice and the inner surface slice for the shallow crack tests, respectively. Then, one can use the linear interpolation method to

modify the Newman and Raju numerical solution for the rest of the slices. An excellent agreement has been found to about ±0.7% between the experimental results and the Newman and Raju solution. The Newman and Raju numerical solution also agrees with the average of the stress intensity factors in the medium crack tests within the range ±2% for the center and inner surface slice. The equivalent radii of the medium crack tests are R = 1.5 in (38.1mm) and R = 1.47 in (37.3mm) for the upper and lower bound, respectively. Similarly, for the deep crack tests, an excellent agreement exists between Newman and Raju's analysis and the experimental results within about ±0.7% for the center and surface slice. The equivalent radii are very close for the upper bound and lower bound. They are R = 1.42 in (36.1mm) and R = 1.41 in (35.8mm).

In the shallow flaws (a/T < 0.4), the front surface effect dominates the values of the stress intensity factor, K_I. Due to the star-shaped front surface effect, Newman and Raju's numerical solution can not be used directly to predict the distributions of the S.I.F in the star-shaped cutout cylinder. Therefore, the modified Newman and Raju solution is used to describe the experimental results. For the moderate flaws (0.40 < a/T < 0.56), both the front and back surface effects may influence the stress intensity factor. For the deep flaws (a/T > 0.56), the back surface effect dominates the values of the K_I. Apparently, for deeper flaws, K_I can be accurately described by the solution of the Newman and Raju equivalent circular cylinder problem with inner crack under internal pressure. It is clear from the above description that this mathematical model can be used to predict the distributions of the S.I.F along the crack border in the pressurized star-shaped cutout cylinder.

Moreover, Fig.(5.23) shows a plot of unnormalized stress intensity factor K_I versus maximum crack depth a. In the pressurized cylinder with star-shaped cutout tests, when the maximum penetration depth a is less than 0.18 in (4.57mm), the Newman and Raju approximate numerical solution can be used to predict the stress intensity

factor at the location of the maximum crack depth. That means one may use an equivalent inner radius R = 1.62 in (41.1mm) circular cylinder to predict the value of stress intensity factor in a cylinder with star-shaped cutout. Of course, the maximum crack depth a is the same in the equivalent circular cylinder and the cylinder with star-shaped cutout. When the value of the maximum crack depth a is between 0.18 in (4.57mm) and 0.331 in (8.41mm), one can use a series of different equivalent radii circular cylinders to estimate S.I.F in the cylinder with star-shaped cutout. It is clear from the Fig.(5.21)-(5.22) that the Newman and Raju's numerical solution is in excellent agreement with the experimental results when the maximum crack depth a = 0.28 in (7.11mm) or a = 0.33 in (8.38mm). Using Newman and Raju's solution to predict the medium and the deep flaws in a cylinder with star-shaped cutout, one can represent reasonably S.I.F estimates for the problem studied.

For all the tests, one expects to obtain a symmetrical near-tip fringe pattern from the semi-elliptical crack border. That means one should have a pure Mode I field. However, when the surface slices were analyzed, a slightly unsymmetrical fringe pattern appeared. The unsymmetrical fringe pattern is illustrated in Fig.(5.24). The fringe loops are rotated and altered in size. A mixed mode fringe pattern is illustrated in Fig.(5.24) which contains Mode I and Mode II. The main reason for this mixed mode effect lies in the procedure of specimen preparation. When the hole has been drilled through the wall of the star-shaped cutout cylinder, the hole has not been exactly at the center of the finger tip. Therefore, the location of the blade edge has been a little away from the center of the groove. This likely results in the unsymmetrical fringe pattern. This effect may have also resulted from the misalignment of the blade edge with respect to the plane of symmetry of the star finger. However, in all the tests, as the cracks have grown away from the inner surface, the near-tip symmetrical fringe pattern has been restored. This means the pure Mode I fields have been recovered. Furthermore, a

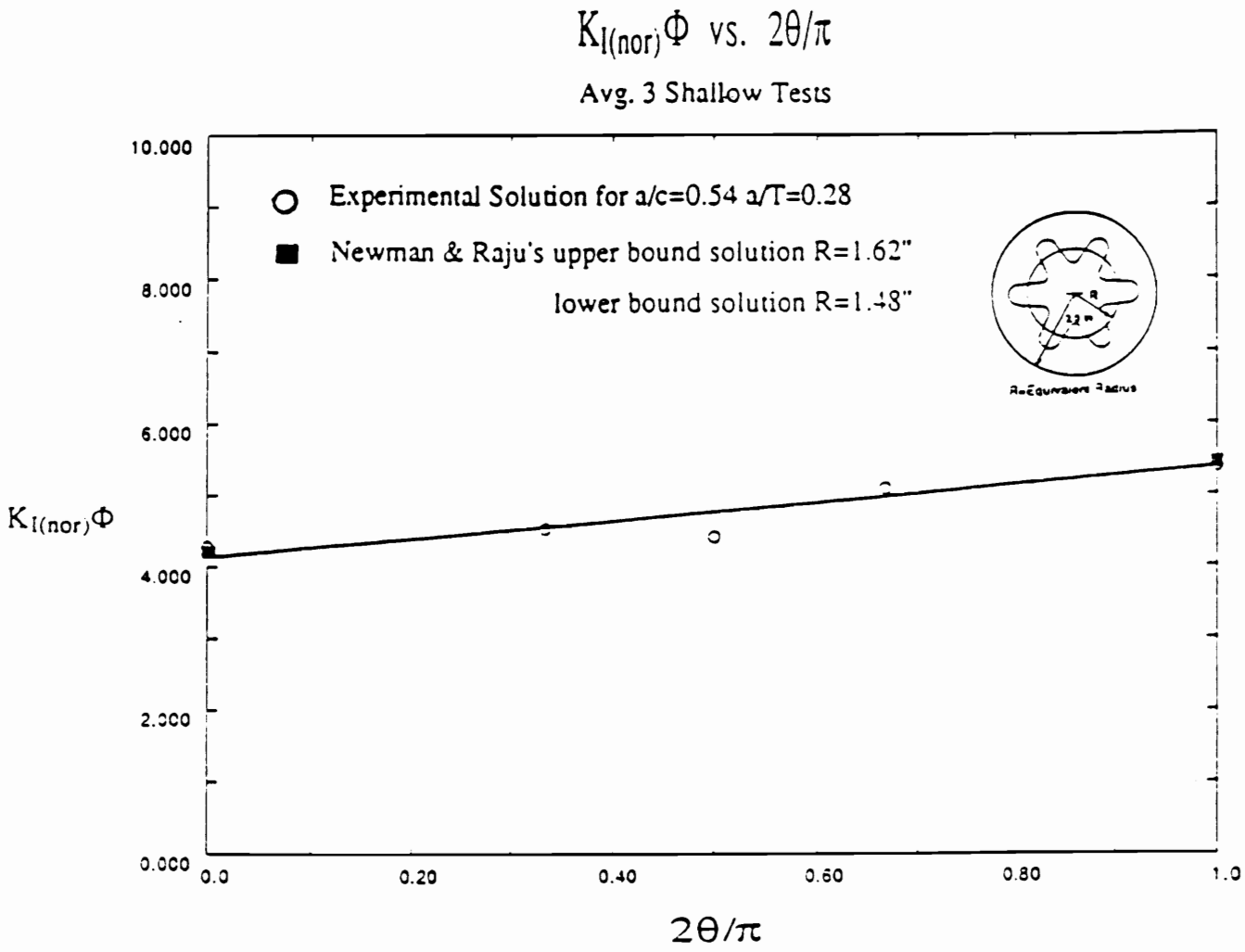

Figure 5.20. Comparison of the distributions of S.I.F for experimental results and Newman & Raju's solutions (shallow crack)

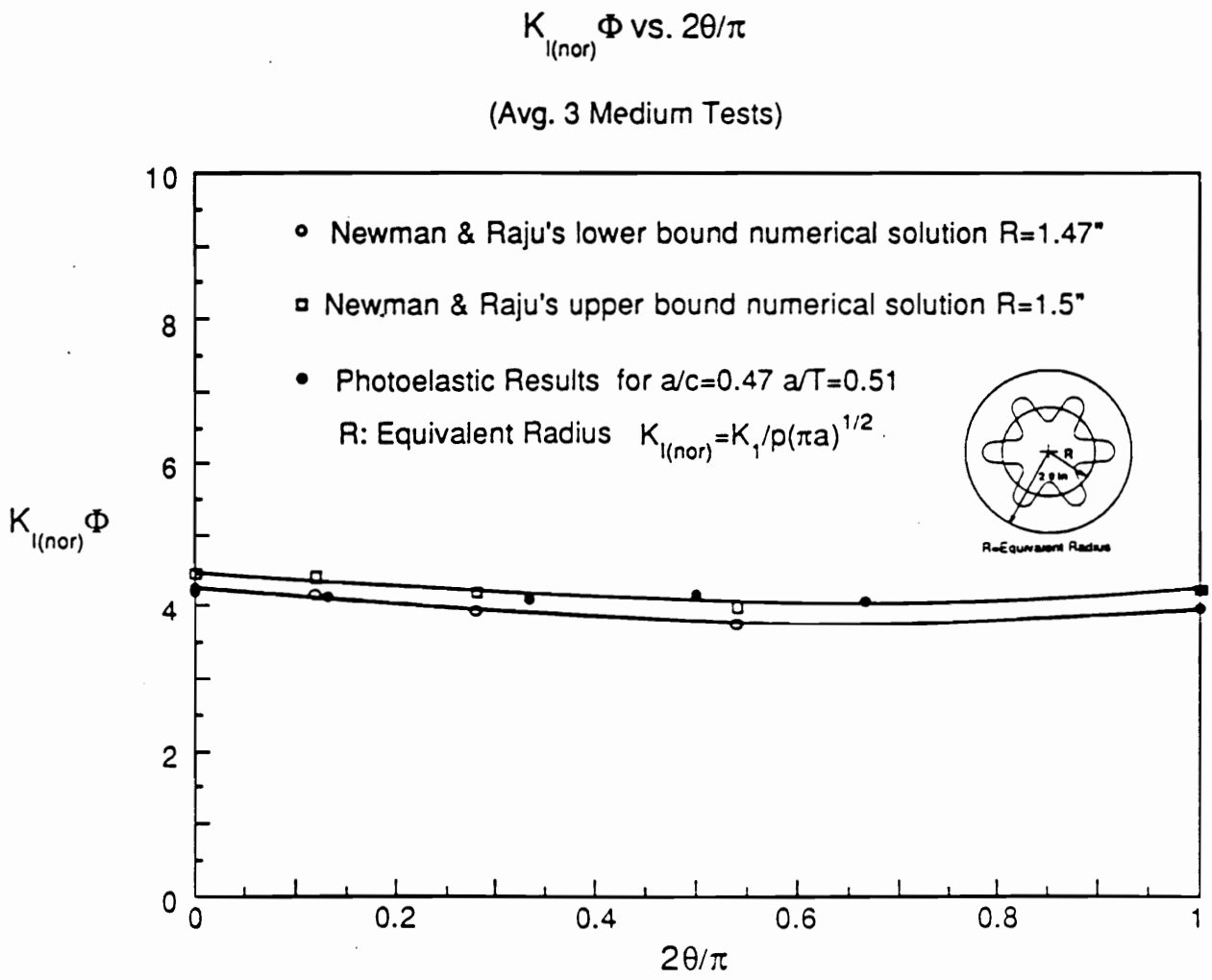

Figure 5.21. Comparison of the distributions of S.I.F for experimental results and Newman & Raju's solutions (medium crack)

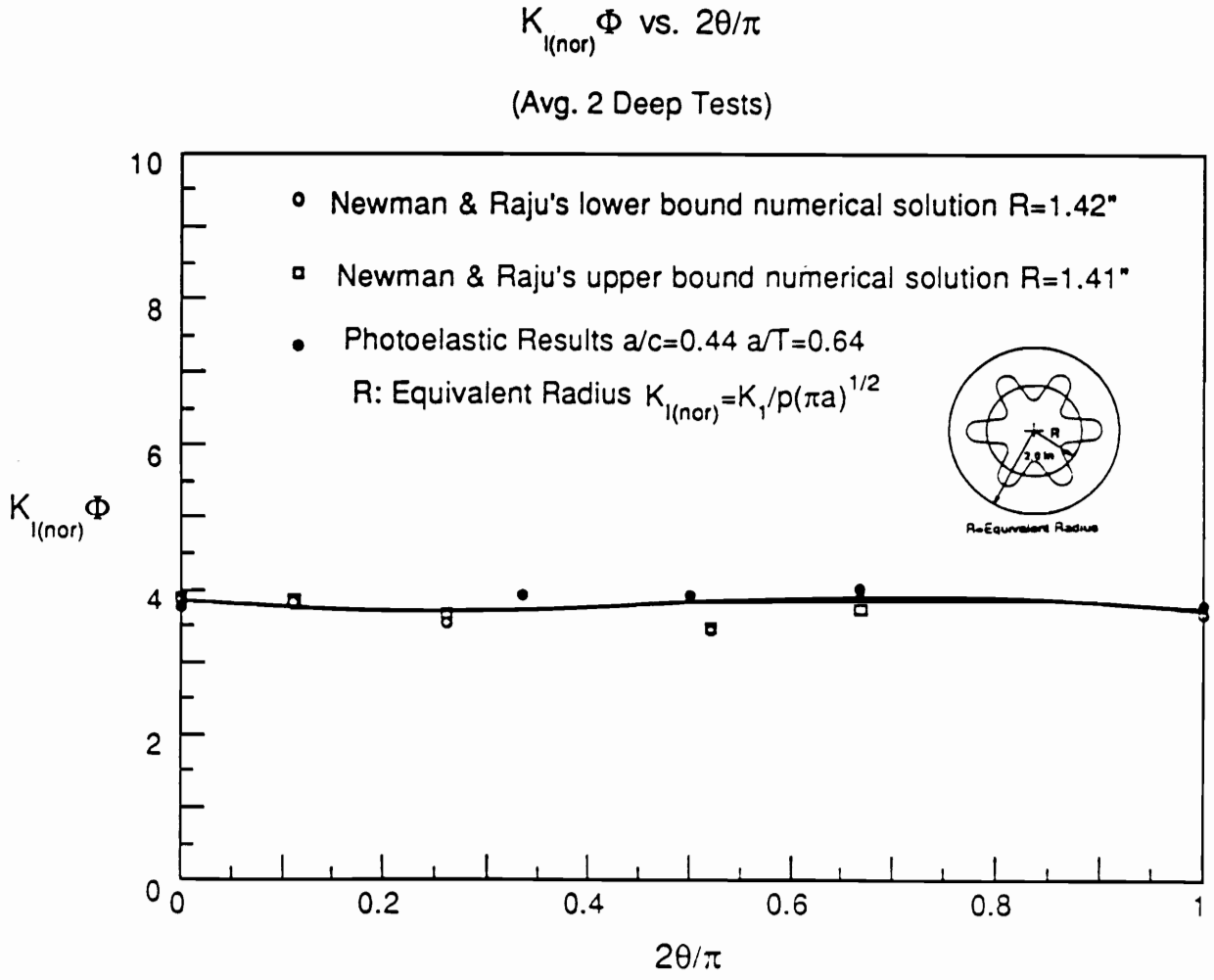

Figure 5.22. Comparison of the distributions of S.I.F for experimental results and Newman & Raju's solution (deep crack)

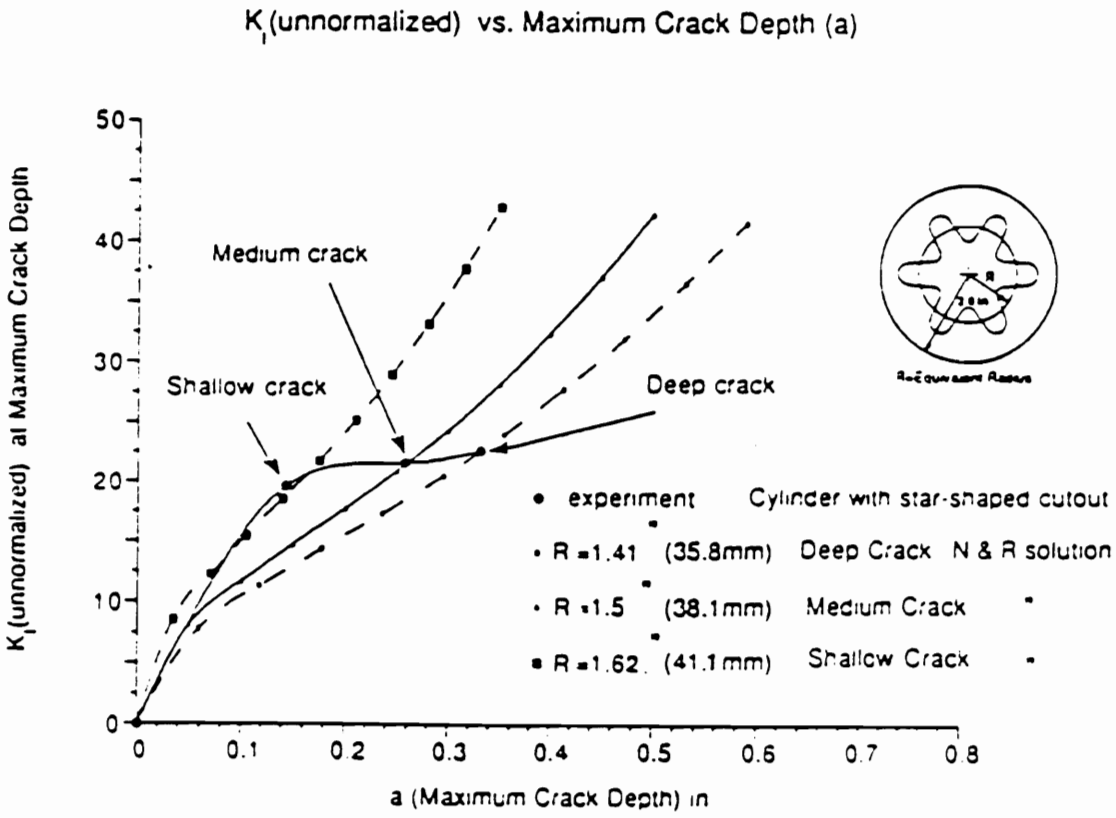

Figure 5.23. A plot of unnormalized S.I.F versus maximum crack depth (a)

mixed mode LEFM algorithm [67]-[68] has been used to extract data from the surface slices which involved the mixed mode effect. After the analysis of these data, the Mode II stress intensity factor has been found to be only 2% of that of Mode I and it can be neglected.

(a) Mixed Mode

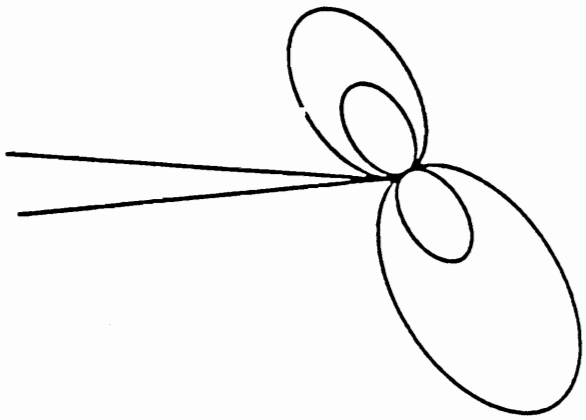

(b) Mode I

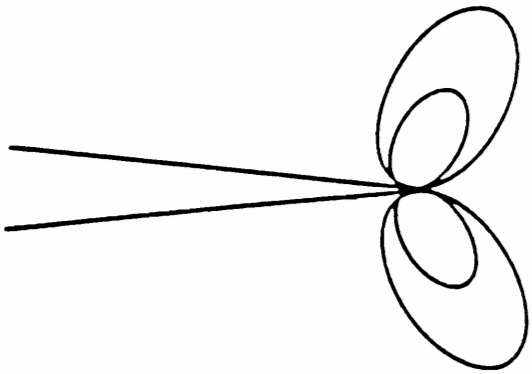

Figure 5.24. Comparison of mixed mode fringe pattern and Mode I fringe pattern

6.0 Summary and Future Work

6.1 Summary

The dissertation describes a refined experimental technique using stress freezing photoelasticity to convert experimental data into fracture parameters. The work also shows the experimental results from experimental studies conducted on the photoelastic model of a solid rocket motor under internal pressure and containing a semi-elliptical surface flaw emanating from the groove of a star finger. The technique is employed to measure the stress singularity order at the right angle intersection of a semi-elliptical crack with an inner star surface under Mode I loading. In addition, the technique provides the distribution of the stress intensity factor (S.I.F) along the border of a surface flaw. The results have been compared with Newman and Raju's three-dimensional finite element analysis for the distribution of the S.I.F in a pressurized circular cylinder and a two-dimensional analysis (a weight function approach) for the radial crack in a circular ring was recommended for predicting maximum S.I.F.'s in rocket motor models. Comparisons were also made with Benthem's numerical solution for measuring the stress singularity at the free surface. The results have also been

experimental results for the distribution of the S.I.F and stress singularity in both four point bending specimens and wide tension plates with surface flaws.

It is concluded that:

(1) The value of stress singularity order when the crack intersects the inner star surface at right angles under pressurized condition agrees with Benthem's result. However, this effect does not appear to influence the S.I.F. computed from a surface slice.

(2) S.I.F. distributions yielded results to within $\pm 6\%$ and showed a uniform S.I.F. distributions around the crack front except for the shallow flaws. By comparing results with the Newman-Raju model for a surface flaw in a cylinder, it appears that, when the surface flaw depth reaches $a/T = 0.5$, the maximum S.I.F. can be predicted accurately with a two dimensional crack in a cylinder using the weight function approach. Reasonable prediction were also obtained for the shallow flaws.

6.2 Future Work

Since fractional fringe order techniques are successfully applicable to frozen stress slices, the frozen stress approach utilizes data very near the crack tip in the measurement zone. It has been shown in chapters 3-5 that the frozen stress method works quite well for Mode I problems. After establishing a rich data base for this complex geometry model, the cracks that make an angle with respect to the plane of symmetry of the star finger could also be a good choice for a better understanding of the behavior of the rocket motor model.

The other recommendation is to develop a finite element program to perform two dimensional analysis for the rocket motor geometry.

References

1. Francis, A.W., "Rocket Propellant," Chap. 7, Chapman Hall, LTD., London, 1960.

2. Swedlow, J.L., Ed. "The Surface Crack: Physical Problems and Computational Solutions," Proc. of ASME Symposium, Nov. 1972.

3. McGowan, J.J., "A Critical Evaluation of Numerical Solutions to the "Benchmark" Surface Flaw Problem," Monograph of Fracture Committee of Society for Experimental Stress Analysis (Society for Experimental Mechanics), 1980.

4. Smith, C.W., "Analytical and Experimental Analysis of the Surface Flaw," Optical Methods in Composites (Proceeding of an SEM Symposium), Keystone, June, 1988, pp. 194-200.

5. Durelli, A.J., "Experimental Means of Analyzing Stresses and Strains in Rocket Propellant Grains," Experimental Mechanics, Apr. 1962, pp.102-109.

6. Francis, E.C., Lindsey, G.H., and Parmerter, R.R., "Pressurized Crack Behavior in Two-Dimensional Rocket Motor Geometries," J. of Spacecraft, Vol. 9, No. 6, June 1972, pp.415-419.

7. Benthem, J.P., "The Quarter Infinite Crack in a Half Space: Alternative and Additional Solutions," International Journal of Solids and Structures, Vol. 16, 1980, pp.119-130.

8. Smith, C.W., Epstein, J.S., and Rezvani, M., "Measurement of Dominant Eigenvalues in Cracked Body Problems," International J. of Fracture, Vol. 39, 1989, pp.15-24.

9. Smith, C.W., "Use of Three Dimensional Photoelasticity and Progress in Related Areas," Experimental Techniques in Fracture Mechanics, Vol. 2, A.S. Kobayashi, Ed., Society for Experimental Stress Analysis Monograph, No. 2, 1975, pp.3-58.

10. Durelli, A.J., "Experimental Strain and Stress Analysis of Solid Propellant Rocket Motors," Mechanics and Chemistry of solid Propellant ; Proceeding of the Fourth

Symposium on Naval and Structural Mechanics, Purdue University, Lafayette, Ind. Pergamon Press, Oxford, 1967, pp.381-442.

11. Becker, E.B. and Brisbane, J.J., "The Effect of Propellant-Case Interaction on Stress/Strain Concentration Factors in Solid Propellant Rocket Grains," Rohm & Mass Company Special Report.

12. Bazant, Z.P., "Three Dimensional Harmonic Function Near Termination or Interaction of Gradient Singularity Lines: A General Numerical Methods," International J. of Engineering Science, Vol. 12, 1974, pp.221-243.

13. Bazant, Z.P. and Estenssoro, L.F., "Surface Singularity and Crack Propagation," International J. of Solids and Structures, Vol. 15, 1979, pp.405-426.

14. Benthem, J.P., "The Quarter Infinite Crack in a Half-Space, Alternative and Additional Solutions," Int. J. of Solids and Structures, vol. 16, 1980, pp.119-130.

15. Benthem, J.P., "Three Dimensional State of Stress at the Vertex of a Quarter Infinite Crack in a Half-Space," Report WTHD No. 74, Delft University of Technology, 1975, pp.405-426.

16. Benthem, J.P., "Graphs of the Three Dimensional State of Stress at the Vertex of a Quarter Infinite Crack in a Half-Space," Delft University, Report 123, 1980.

17. Benthem, J.P., "On an Inversion Theorem for Conical Regions in Elasticity," J. of Elasticity, Vol. 9, No. 2, 1979.

18. Kawai, T. and Fujitani, Y., "Analysis of a Singularity at the Root of the Surface Crack Problems," Proc. of the International Conference on Fracture Mechanics, 1977, pp.1159-1163.

19. Kawai, T. and Fujitani, Y., "Analysis of Three Dimensional Surface Crack Problems by Boundary Integral Methods," Seisan-Kehkyu, Vol. 1, No. 2, 1976, pp.26-29.

20. Folias, E.S., "On the Three Dimensional Theory of Cracked Plate," J. of Applied Mechanics, Trans. of ASME, 1975, pp.663-674.

21. Swedlow, J.L., "Singularity Computations," International J. for Numerical Methods in Engineering, Vol. 12, 1978, pp.1779-1798.

22. Williams, M.L., "Stress Singularities Resulting From Various Boundary Conditions in Angular Corners of Plates Under Bending," Proc. of the U.S. National Congress of Applied Mechanics, 1951.

23. Burton, W.S., Sinclair, G.B., Solecki, J.S., and Swedlow, J.L., "On the Implications for LEFM of Three Dimensional Aspects in some Crack Surface Intersection Problems," International J. of Fracture, Vol. 25, 1984, pp.3-32.

24. Takakuda, K., "Stress Singularities Near Crack Front Edges," Bull. JSME, Vol. 1.28, 1985, pp.225-231.

25. Griffith, A.A., "The Phenomena of Rupture and Flow in Solid," Philosophical Trans. of the Royal Society, London, Series A, Vol. 221, 1921, pp.163-197.

26. Cruse, T.A., "Three-Dimensional Elastic Surface Cracks," Fracture Mechanics: Nineteenth Symposium, ASTM STP 969, 1988, pp.19-42.

27. Cruse, T.A., Meyers, G.J., and Wilson, R.B., "Fatigue Growth of Surface Crack,"Flaw Growth and Fracture: Tenth Conference, ASTM STP 631, American Society for Testing Material, Philadelphia, 1977, pp.174-189.

28. Dally, J.W., Sciammarella, C.A., and Shareef, I., "Extraction of Stress-Intensity Factor from In-Plane Displacements Measured by Holographic Interferometry," Surface Crack Growth: Models, Experiments, and Structures, ASTM STP 1060, 1990, pp.130-141.

29. Westergaard, H.M., "Bearing Pressures and Cracks: Bearing Pressures Through a Slightly a Waved Surface or Through a Nearly Flat Part of a Cylinder, and Related Problems of Cracks," J. of Applied Mechanics, Vol. 6, 1979, pp.289-294.

30. Muskhelishvili, N.I., "Some Basic Problems of the Mathematical Theory of Elasticity," Nordhoff Ltd., Groningen, The Netherlands, 1953, pp.104-161.

31. Raju, I.S., and Newman, J.C., "Stress-Intensity Factors for Internal and External Surface Cracks in Cylindrical Vessels," J. of Pressure Vessel Technology, Vol.104, Nov. 1982, pp.293-298.

32. Atluri, S.N., and Kathiresan, K., "3D Analysis of Surface Flaws in Thick-Walled Reactor Pressure-Vessels using Displacement-Hybrid Finite Element Method," Nuclear Engineering and Design 51, 1979, pp.163-176.

33. Nishioka, T., and Atluri, S.N., "Analysis of Surface Flaw in Pressure Vessels by a New 3-Dimensional Alternating Method," J. of Pressure Vessel Technology, Vol. 104, Nov. 1982, pp.299-307.

34. Tan, C.L., and Fenner, R.T., "Stress Intensity Factors for Semi-Elliptical Surface Cracks in Pressurised Cylinders Using the Boundary Integral Equation Method," International J. of Fracture, Vol. 16, No. 3, June 1980, pp.233-245.

35. Kobayashi, A.S., Polvanich, N., Emery, A.F., and Love, W.J., "Inner and Outer Cracks in Internally Pressurized Cylinders," J. of Pressure Vessel Technology, Feb. 1977, pp.83-89.

36. Epstein, J.S., "On the Variation of the First Classical Eigenvalue of Fracture Mechanics in the Three Dimensional Transitory Stress Field," Ph.D. Dissertation, VPI & SU, 1983.

37. Lloyd, W.R., "Experimental Determination of the Stress Singularity Exponent in Cracked Bodies Using Photoelasticity," Master's Thesis, VPI&SU. 1986.

38. Smith, C.W., and Rezvani, M., "Free Surface Effects on Nonlinear Near Tip Zone for Cracks Intersecting Free Surfaces," The Joint ASME/SES Applied Mechanics and Engineering Sciences Conference, Vol. 91, June 1988, pp.289-297.

39. Smith, C.W., Theiss, T.J., and Rezvani, M., "Intersection of Surface Flaws with Free Surfaces: An Experimental Study," Fracture Mechanics: Perspectives and Directions (Twentieth Symposium), ASTM STP 1020, 1989, pp.317-326.

40. Smith, C.W., Rezvani, M., and Chang, C.W., "Analysis of Optical Measurements of Free-Surface Effects on Natural Surface and Through Cracks," Surface-Crack Growth: Models, Experiments, and Structures, ASTM STP 1060, 1990, pp.99-111.

41. Smith, C.W., Epstein, J.S., and Olaosebikan, O., "Boundary Layer Effects in Cracked Bodies: An Engineering Assessment," Fracture Mechanics: Seventeenth Volume, ASTM STP 905, 1986, pp.775-788.

42. Smith, C.W., "Measurement of Three-Dimensional Effects in Fracture Mechanics," Fracture Mechanics: Nineteenth Symposium, ASTM STP 969, 1988, pp.5-18.

43. Smith, C.W., Lloyd, W.R., and Olaosebikan, O., "An Assessment of the Corresponding Stress-Intensity Factor for Accounting for Boundary Effects in Cracked Bodies," Fracture Mechanics: Eighteenth Symposium, ASTM STP 945, 1988, pp.699-710.

44. Smith, C.W., and Rezvani, M., "Measurement of Boundary Effects in Surface Flaws," Proc. of Joint International Conference of the British Society for Strain Measurement & the Society for Experimental Mechanics, 1987.

45. Smith, C.W., Epstein, J.S., and Olaosebikan, O., "Experimental Boundary Layer Studies in Three Dimensional Fracture Problems," Advances in Aerospace Structures, Materials, and Dynamics, ASME-AO-06, 1983, pp.119-126.

46. Smith, C.W. and Epstein, J.S., "Experimental Boundary Layer Phenomena in High Poisson Ratio Fracture Mechanics," Proc. of U.S. Army Symposium on Solid Mechanics, 1984, pp.51-64.

47. Tardy, M.H.L., "Methode Pratique d'examen de mesure dela birefringence des verres d'optique," Rev. Opt., Vol. 8, 1929, pp.59-69.

48. Post, D., "Fringe Multiplication in Three Dimensional Photoelasticity," J. of Strain Analysis, Vol. 1, No. 5, 1966, pp.380-388.

49. Post, D., "Isochromatic Fringe Sharpening and Fringe Multiplication in Photoelasticity," Proc. Soc. Experimental Stress Analysis, Vol. 12, No. 2, 1955, pp.143-153.

50. Photoelastic Division, "Bulletin S-116-B," Measurement Group Inc., Raleigh, N.C.

51. Dally, J.W. and Riley, W.F., "Experimental Stress Analysis," Ch. 14, McGraw Hill Book Company, Second Edition, 1978.

52. Dally, J.W. and Riley, W.F., "Experimental Stress Analysis," Ch. 13, McGraw Hill Book Company, Second Edition, 1978.

53. Epstein, J.S., Post, D., and Smith, C.W., "Three-Dimensional Photoelastic Measurements with Very Thin Slices," Experimental Techniques, pp. 34-37, Dec. 1984.

54. Irwin, G.R., "Analysis of Stresses and Strain Near the End of a Crack Traversing a Plate," J. of Applied Mechanics, Vol. 79, 1957, pp.34-37.

55. Williams, M.L., "On the Stress Distribution at the Base of a Stationary Crack," J. of Applied Mechanics, March 1957, pp.109-114.

56. Kassir, M.K. and Sih, G.C., "Three Dimensional Stress Distribution Around an Elliptical Crack Under Arbitrary Loadings," J. of applied Mechanics, Sep. 1966, pp.601-610.

57. Smith, C.W., "Determination of Stress Intensity Factors, K_1, K_2, K_3 by the Frozen Stress Method," J. of Optical Engineering, Vol. 27, No. 8, Aug. 1988, pp.619-624.

58. Rezvani, M., "A Study of Near Tip Phenomena for Cracks in a Particulate Composite," Ph.D. Dissertation, VPI & SU, 1989.

59. Nadi, A., "Uber die Spannungsurefeilung in einer durch eine Einzelkraft belasteten rechtekigen platte," Der Bauingenieur, Vol. 2, 1921, pp.11-16.

60. Smith, C.W., Chang, C.W., and Rezvani, M., "Analysis of Optical Measurements of Free Surface Effects on Natural Surface and Through Cracks," Symposium on Surface Crack Growth, Reno, Nevada, April 1988.

61. Bueckner, H.F., "Weight Functions for the Notched Bar," Zeitschrift Fun angewandte Mathematik und Mechanik, Vol. 51, 1971, pp.97-109.

62. Rice, J.R., "Some Remarks on Elastic Crack-Tip Stress Field," International J. of Solids and Structures, Vol. 8, No. 6, June 1972, pp.751-758.

63. Bowie, O.L. and Freese, C.E., "Elastic Analysis for a Radial Crack in a Circular Ring," Engineering Fracture Mechanics, Vol. 4, 1972, pp.315-321.

64. Smith, C.W., "Fracture Mechanics," ESM 6050, ESM Dept., Va. Tech., Blacksburg, 1987.

65. Grandt, Jr., A.F., "Two Dimensional Stress Intensity Solution for Radially Cracked Rings," 11th Annual Meeting of Society for Engineering Science, Nov. 1974, Durham, N.C.

66. Grandt, Jr., A.F., "Stress Intensity Factors for Some Through-Cracked Fastener Holes," International J. of Fracture, Vol. 11, No. 2, Apr. 1975, pp.283-294.

67. Smith, C.W. and Epstein, J.S., "An Assessment of Far Field Effects on the Photoelastic Determination of Mixed Mode Stress Intensity Factors," Engineering Fracture Mechanics, Vol. 16, No. 5, 1982, pp.605- 612.

68. Smith, C.W. and Olaosebikan, O., "Use of Mixed-Mode Stress-Intensity Algorithms for Photoelastic Data," Experimental Mechanics, Vol. 24, No. 4, 1984, pp.300-307.

Appendix A.

In the conducted tests, the Tardy compensation method and the Fringe multiplication methods have been combined to obtain fractional fringes. The Tardy compensation method was introduced by Tardy in 1929 [47]. The dark and light field arrangements of the circular polariscope are shown in Fig.(A.1). The analyzer there is rotated by some arbitrary angle. The purpose of the rotation is to provide a means for determining fractional fringe orders. The details of the Tardy method is given by Dally and Riley [51] and will not be described here.

The photoelastic fringe multiplication technique has been developed by Post [48-49]. The technique increases the fringe order at every point and produces an isochromatic pattern containing several times as many fringes as the regular fringe pattern. The photoelastic fringe multiplication unit Fig.(3.14) has been set up by Epstein [53]. The system includes a photoelastic Model 051 polariscope unit, laser source , fringe multiplication unit, micrometer stage, expanding lens, and view glass.

For fringe multiplication, the partial mirrors are inclined to each other at a small angle. The resulting behavior of the light is shown in Fig.(A.2). When the light arrives at a mirror surface, part of the light is transmitted and part is reflected. The light

passes back and forth through the model. The fringe pattern order is multiplied by the number of times the light observed has passed through the model. The multiplication factor is an odd or an even number depending on whether the beam observed emerges from the forward or backward direction, respectively. When the thin slices was removed from the specimens, the fringe pattern orders would decrease and so the number of data points for the analysis would be reduced. For our case, a third or fifth multiplication factor has been used and the analyzer has been rotated by 18^{0}. These two methods have been combined together to obtain thirty to fifty data points for one slice. Ordinarily, the thickness of the slice is about 0.5mm. In addition, the slice lying on the fringe multiplication unit is shown in Fig.(A.3) An index matching fluid fills the space between the mirrors and the slice. The index matching fluid should match the slices closely.

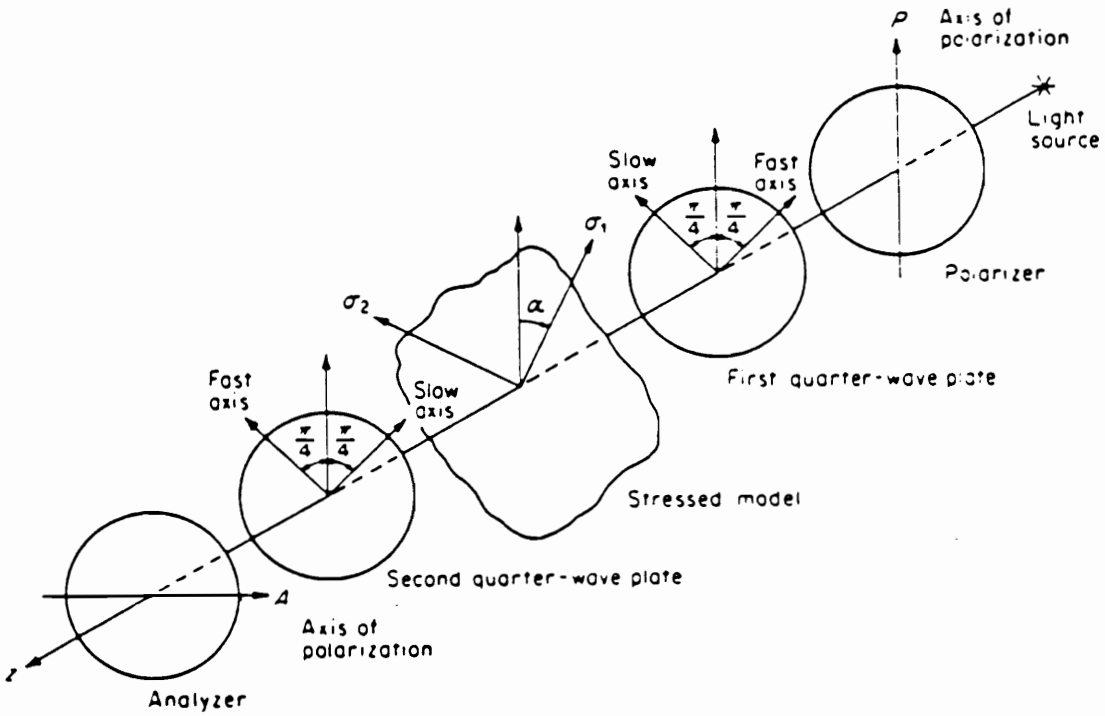

Figure A.1. Arrangement of circular polariscope [52]

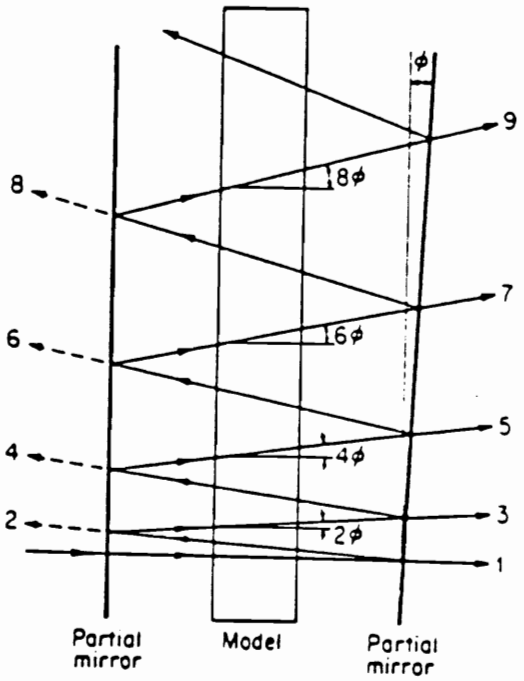

Figure A.2. Light path through model and two inclined mirrors [52]

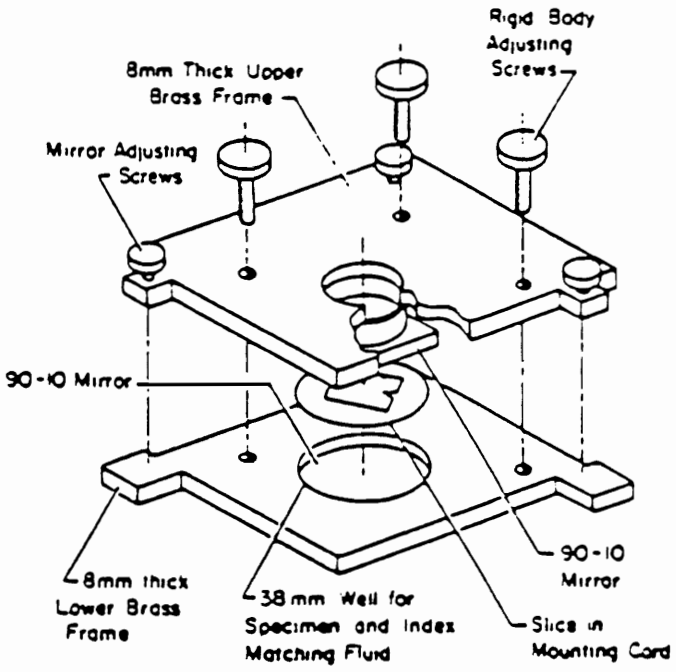

Figure A.3. The fixture used in the fringe multiplier unit [53]

Appendix B.

```
//B120CHA JOB 20CE5,CHANG,TIME=1,REGION=3500K
/*PRIORITY STANDARD
/*ROUTE PRINT VTMVS1.LOCAL
/*JOBPARM LINES=1
//STEP1 EXEC SAS
//SYSIN DD *
GOPTIONS DEVICE=VER80 ;
*   CHANGE THICKNESS (TH) EVERY TIME !!!!   ;
*   CHANGE MULTIPLICATION FACTOR (MULFAC) EVERY TIME!!!   ;
DATA RAW;
INPUT N1 R1 R2;
A=.1420;
P=3.90;
MULFAC=3;
RIN=ABS(R2-R1)/2.0;
RMM=RIN*25.4;
N=N1/MULFAC;
F=2.682;
C=.25**2-RIN**2;
Y1=ABS(SQRT(C));
TH=.25-Y1+.0325;
TAUM=N*F/(2*TH);
SQRT=(RIN/A)**0.5;
SQRT1=(RIN/0.5)**0.5;
SQRT2=RIN**0.5;
K1AP=TAUM*((8*3.141593*RIN)**0.5);
Y=K1AP/(P*((3.141593*A)**0.5));
LN_R=LOG(RIN);
LN_N=LOG(TAUM);
CARDS;
1.0   .5833   .4468
1.1   .5724   .4635
1.2   .5574   .4730
1.3   .5502   .4808
1.4   .5424   .4860
1.5   .5346   .4891
1.6   .5317   .4915
1.9   .5238   .4999
2.0   .5205   .5030
;
```

```
PROC GPLOT DATA=RAW ;
TITLE1 'TAUM VS.R IN. T10-0-2S TH.= VARIABLE ';
PLOT TAUM*RIN;
SYMBOL1 I=NONE V=DIAMOND C=BLUE L=1;
PROC GPLOT DATA=RAW ;
TITLE1 'LN(TAUM) VS. LN(R) IN. T10-0-2S TH.=VARIABLE ';
PLOT LN_N*LN_R;
SYMBOL1 I=NONE V=DIAMOND C=BLUE L=1;
PROC GPLOT DATA=RAW ;
TITLE1 'K1AP(NORM) VS. SQRT(R/A) T10-0-2S TH.=VARIABLE ';
PLOT Y*SQRT;
SYMBOL1 I=NONE V=DIAMOND C=BLUE L=1;
PROC GPLOT DATA=RAW ;
TITLE1 'K1AP VS. SQRT(R) T10-0-2S TH.=VARIABLE ';
PLOT K1AP*SQRT2;

SYMBOL1 I=NONE V=DIAMOND C=BLUE L=1;
DATA;SET RAW;
PROC PRINT;VAR N RIN  RMM LN_R LN_N  SQRT Y SQRT1 SQRT2 K1AP  TAUM TH;
/*
//
```

Vita

The author was born in Taichung on August 5 1956. He completed his elementary education from Tsai-Tun Preliminary school and his high school education from the First Taichung High School in Taichung, Taiwan. In September 1975, he started to study at National Cheng Kung University in Tainan, Taiwan and completed his requirements for a Bachelor of Science degree in Civil Engineering in June, 1979.

Upon graduation he served in the Marine for two years and then worked as a civil engineer for Fu-Chu Construction Co., Taiwan for two years.

In January 1984, the author came to the States and entered the Utah State University, Logan, Utah where he received his Master of Science degree i Civil Engineering.

Since January 1986 he has been enrolled at Virginia Polytechnic Institute and State University pursuing the degree of Doctor of Philosophy in Engineering Science and Mechanics. At the time of this writing the author has accepted a Research Scientist at the Industrial Technology Research Institute, Material Research Laboratories, Hsin Chu, Taiwan beginning in September 1990.